# CONTENTS

## I Code and problem presentation 11

## II SIMULATION RESULTS 37

# NOMENCLATURE

## Flow variables and coefficients

| | |
|---|---|
| $c_p$ | specific heat at constant pressure |
| $c_v$ | specific heat at constant volume |
| $R$ | gas constant |
| $\gamma$ | specific heat ratio |
| $\lambda$ | thermal conductivity |
| $k$ | thermal diffusivity |
| $\rho$ | density |
| $\mu$ | dynamic viscosity |
| $\nu$ | kinematic viscosity |
| $t$ | time |
| $x_i,\ (x, y, z)$ | Cartesian coordinate |
| $u_i,\ (u, v, w)$ | velocity components |
| $p$ | pressure |
| $T$ | temperature |
| $T_i$ | total temperature |
| $T_t$ | total temperature defined using $Pr_m = 1$ |
| $e$ | total energy per unit mass |
| $H$ | stagnation enthalpy |
| $\mathcal{F}_i,\ (E, F, G)$ | fluxes in the $i$-direction |
| $S_{ij}$ | traceless strain rate tensor |

## Reference quantities

| | |
|---|---|
| $T_w$ | wall temperature |
| $T_{wx}$ | wall temperature in the streamwise direction |
| $h$ | channel half-width |
| $\rho_b$ | bulk-averaged density |
| $u_b$ | bulk-averaged velocity |
| $(\rho u)_b$ | bulk-averaged mass flux |
| $u_\tau$ | friction velocity scale |
| $u_p$ | streamwise pressure gradient based velocity scale |
| $u_{\tau p}$ | extended inner velocity scale |
| $T_\tau$ | friction temperature |
| $T_p$ | streamwise pressure gradient based temperature scale |
| $T_{\tau p}$ | extended inner temperature scale |

## Non-dimensional parameters

| | |
|---|---|
| $Re$ | Reynolds number |
| $Re_l$ | local Reynolds number |
| $Re_\tau$ | friction Reynolds number |
| $Re_\tau^c$ | integral friction Reynolds number |
| $Re_\nu$ | Bradshaw's scaling |
| $Re_\nu$ | Huang's *et al.* semi-local scaling |
| $M$ | Mach number |
| $M_l$ | local Mach number |
| $M_b$ | bulk-averaged Mach number |
| $M_t$ | turbulent Mach number |
| $M_\tau$ | friction Mach number |
| $Pr$ | Prandtl number |
| $Pr_t$ | turbulent Prandtl number |
| $Pr_m$ | mixed Prandtl number |
| $Pr_{sgs}$ | subgrid scale Prandtl number |
| $B_q$ | non-dimensional heat flux |

## Large Eddy Simulation

| | |
|---|---|
| $\Phi$ | a general flow parameter |
| $\Delta$ | characteristic scale of the grid mesh |
| $\bar{.}$ | low-pass filter of width $\Delta$ |
| $\tilde{.}$ | density-weighted (Favre) filter |
| $\mu_{sgs}, \nu_{sgs}$ | sgs eddy viscosities |
| $\lambda_{sgs}$ | sgs eddy conductivity |
| $\mathcal{T}_{ij}$ | subgrid-scale stress tensor |
| $\mathcal{Q}_i$ | subgrid-scale heat flux vector |
| $\varpi$ | macropressure |
| $\vartheta$ | macrotemperature |
| $u'_i$ | velocity fluctuation in the $i$-direction |

## Numerical simulation

| | |
|---|---|
| $\delta_{ij}$ | Kronecker delta |
| $(\rho, u, v, w, p, T)$ | primitive variables |
| $(\rho, \rho u, \rho v, \rho w, \rho e)$ | conservative variables |
| $\langle . \rangle$ | ensemble or Reynolds average |
| $\{.\}$ | density-weighted or Favre average |
| $f_i$, $W$ | source terms |
| $f$ | distributed force modelling the streamwise favorable pressure gradient in the channel |
| $g$ | distributed force modelling the streamwise adverse pressure gradient in the channel |
| $c_{norm}$ | normalized speed of sound |
| $p_{norm}$ | normalized pressure |
| $\lambda_i,\ i = 1, 5$ | characteristic velocities, one-dimensional eigenvalues |
| $L_i,\ i = 1, 5$ | amplitudes of characteristic waves |
| $d_i,\ i = 1, 5$ | normal derivatives to the boundary |
| $\alpha_{i,j}$ | turbulence anisotropy tensor |
| $I_2$ | second invariant of the anisotropy tensor |
| $I_3$ | third invariant of the anisotropy tensor |
| $R_{u'_i u'_j}$ | correlation coefficient for the Reynolds stress tensor |
| $R_{u'_i T'}$ | correlation coefficient for the turbulent heat flux |
| $c$ | MSRA coefficient |
| $C^{Ti}$ | temperature derivative coefficient |
| $C_f$ | skin-friction coefficient |
| $C_h$ | heat transfer coefficient |
| $C_p$ | pressure coefficient |
| $s$ | Reynolds Analogy factor |

## Modelling

| | |
|---|---|
| $\delta$ | velocity wall-layer thickness |
| $\delta_T$ | thermal wall-layer thickness |
| $k$ | turbulence kinetic energy per unit mass |
| $\mu_t$ | turbulent dynamic viscosity |
| $\nu_t$ | turbulent kinematic viscosity |
| $\lambda_t$ | turbulent thermal conductivity |
| $\tau_w$ | wall friction |
| $q_w$ | wall heat flux |
| $y^+$ | standard wall unit |
| $y^{c+}$ | proposed integral lengthscale |
| $y^*$ | extended wall unit for distorted/separated wall layers |
| $y^{c*}$ | integral extended lengthscale for distorted/separated wall layers |
| $\alpha, \beta$ | ratios useful for modelling distorted/separated wall layers |

## Subscripts and superscripts

| | |
|---|---|
| 1, 2, 3 | streamwise, wall-normal and spanwise directions |
| $i,\ j,\ k$ | tensor directions which vary from 1 to 3 |
| $.'\ .''$ | fluctuating quantities |
| $w$ | evaluated at wall |
| $e$ | referring to the external flow |
| 0 | referring to the homogeneous contribution |
| $rms$ | root-mean-square fluctuations |
| $+$ | referring to the standard wall unit |
| $c+$ | referring to the extended inner scaling proposed integral scaling |
| $*$ | referring to the extended inner scaling |
| $c*$ | referring to the extended integral inner scaling |
| $VD$ | referring to the van Driest transformation |
| $CDS$ | referring to the Carvin-Debiève-Smits transformation |

## Abbreviaton

| | |
|---|---|
| $LES$ | Large-Eddy Simulation |
| $DNS$ | Direct Numerical Simulation |
| $CFL$ | Courant-Friedrichs-Levy criterion |
| $FSF$ | Filtered Structure-Function model |
| $SGS$ | Sub-Grid Scale model |
| $AIM$ | Anisotropy Invariant Map |
| $SRA$ | Strong Reynolds Analogy |
| $MSRA$ | Modified Strong Reynolds Analogy |
| $CESRA$ | Modified Strong Reynolds Analogy for channel flows |

# CHAPTER 1

# Introduction

Compressible turbulent channel flow has been studied extensively both experimentally and using numerical simulations due to its geometric simplicity. There have been many experimental studies which provided valuable knowledge about the friction coefficient, the mean velocity and temperature profiles and so on ([6, 83, 80, 25, 26]. Direct Numerical Simulations (DNS) and Large Eddy Simulations (LES) exist in the literature for relatively low Reynolds numbers $3000 \leq Re \leq 6000$ and up to a Mach number $M = 3$ [14, 34, 50, 48, 74, 27].

The motivation behind this work is to use large-eddy simulation (LES) to extend the knowledge of complex turbulent wall flows involving or not adverse pressure gradient effects and compressibility effects. The flows investigated are fully developed channel flows, spatially developing channel flow and distorted channel flow, for a compressible fluid. The aim is to analyze the behavior of attached wall layer and distorted/separated wall layer subjected to a local adverse pressure gradient at intermediate Reynolds number and non hypersonic Mach number. [1]

On the basis of the linearized equations of motion in a viscous heat-conducting compressible gas, Kovasznay decomposed compressibility effects into vortical, acoustic and entropic contributions [46], which are related to the vorticity, the pressure and the temperature fields, respectively. The relative growth of each of the three compressibility modes defined above can be used to classify turbulent wall bounded flows. Bradshaw [6] performed such analysis to express the so called 'Morkovin's hypothesis': *'in non hypersonic boundary layers ($M \leq 5$), the acoustic mode is negligible ($p_{rms} \ll \langle P \rangle$) and the entropic mode is small ($T_{t_{rms}} \ll \langle T_t \rangle$).* In such context, the compressibility essentially affects the large scales of the turbulent flow and is driven by a *'coupling between sound and thermal fields'* described by Morkovin [62] in the following way : *'The coupling occurs primarly through spatial and timewise variation of density, viscosity and heat conductivity'*.

The first consequence of this *coupling* is a full analogy between the velocity and the temperature field which can be derived at three different levels:

- Reynolds Analogy between integral wall friction and temperature variations [75, 6];
- Crocco-Busemann relation between mean local temperature and velocity [16, 9] and

---

[1] The present study is part of a French-German DFG-CNRS collaboration entitled 'Large Eddy Simulation of Complex Flows' (UR507). It is related to 'Wall-Layer Models for Large Eddy Simulation of Complex Flows', a subproject coordinated by Michael Manhart from the Technische Universität München, for the German side, and Christophe Brun from the University of Orléans, for the French side.

- Strong Reynolds Analogy (SRA) related to turbulent stresses and turbulent heat fluxes [62].

A second consequence of the *'coupling between sound and thermal fields'* concerns the universality of the structure of the turbulence which is expressed by Morkovin [62] in the following terms :

*'The large scale motion* (mean velocity field) *should be statistically coupled to the thermal field almost exclusively through mean values of $\rho$, $\mu$, $\lambda$, and the generalized law of the wall so that with a variable lateral stretching factor, it may resemble the incompressible motion.'*

This universal logarithmic law for the mean velocity profile is obtained based on an only density-weighted transformation (van Driest transformation, hereafter denoted VD) [88, 6].

An universal logarithmic law for the total temperature has been derived as well thanks to the VD transformation [59, 11, 17], and is of special interest for supersonic boundary layers. The VD transformation performs generally better for adiabatic boundary layers than for isothermal boundary layers such as the ones developed in a turbulent compressible channel flow [14, 34, 50, 48, 74, 27]. The channel flow configuration is a typical case of non-adiabatic wall layer with non negligible entropic modes. It is characterised by strong mean property changes at the wall which were already referred to by Bradshaw [6] :

*'The effect of mean density variations in y on the turbulence structure is not covered by Morkovin's hypothesis, but is negligible if streamwise pressure gradients are small'* (which is presently not the case in a channel).

*'The influence of compressibility that Morkovin's hypothesis does not treat are the effect of viscosity, in regions where mean viscous stresses are important, and the effects of spatial gradients of mean density'*.

Such effects have been accounted for to derive a wall scaling for compressible flows such as the semi-local scaling from Bradshaw [6] or Coleman *et al.* [14], and the composite scaling from Huang *et al.* [34]. They have been applied by some authors [14, 27] to show that VD transformation was not sufficient to rescale the RMS velocity profiles to fit the incompressible one.

Turbulent separation occurs in turbulent flows involving step changes of the wall, surface curvature or strong adverse pressure gradient. Experimental studies exist for flows over a backward-facing step, over a bump [89] and smooth surfaces [4, 5]. Flows with adverse pressure gradient conditions provided by suction over a cylinder [2, 18] or a flate plate [19] also exist. Numerical simulations involve separation behind a backward-facing step or using suction and blowing on the upper boundary condition of the simulation [65, 81]. It was observed that the turbulent boundary layer experiences an adverse pressure gradient. Consequently, the flow is divided into a thickening inner and an outer layers around the separation with the inner region dictating the skin-friction distribution. Over the detachment an intermediate diffusion layer between the outer and the inner layers develops. Thus, the separation process and the outer region behave almost completely independently as an external free turbulent flow. Therefore, the large scale outer structures survive the separation process and interfere with the regeneration of Reynolds stresses in the inner region after reattachment. This continues for several bubble lengths after reattachment [2].

Simpson [77, 78] has carried out extensive reviews of turbulent boundary layer separation and showed that the classical law of the wall breaks down and that new relations must be designed based on the streamwise pressure gradient effects, which is the scope of the present work.

The main *objectives* of this work are (1) to carry out large-eddy simulations of fully developed channel flows, spatially developing channel flow and distorted channel flow, and (2) to derive analytical laws of the wall for velocity and temperature. Thus, the present report is arranged in three main parts.

In the first part, the compressible Navier-Stokes equations presently solved in the context of an LES description of turbulent scales are presented. A description of the source model for the periodic compressible channel flow is provided. Various formulations are proposed, which will be further studied and compared. Inflow and outflow boundary conditions for simulations in which no periodicity is assumed are introduced. Finally, the principle to generate a distorted/separated channel flow is presented.

The second part is dedicated to the description of the results. The first chapter is a description of the parametric study of fully developed channel flows performed based on Mach number, Reynolds number and source terms. Compressibility and low Reynolds number effects are discussed, classical Reynolds and Favre averaging procedures are compared, an anisotropy invariants analysis is performed, Morkovin's hypothesis is assessed. The issue of the strong Reynolds analogy between velocity and temperature fields in a compressible isothermal-wall is addressed. The modified SRA formulation from Huang *et al.* is analysed and assessed.

The second chapter presents simulations of a spatially developing channel flow, with and without streamwise pressure gradient distortion. The boundary conditions are checked for the spatially developing channel flow. Then, the response of the subsonic turbulent flow to the change of sign in pressure gradient is discussed in terms of instantaneous and mean flow features and anisotropy invariants. The modified strong Reynolds analogy is applied to the present results.

The third part, dedicated to the wall modelling, starts with a brief description of the boundary layers, velocity boundary layer and thermal boundary layer, respectively. The next chapter is an analysis of the attached compressible wall layers presently computed with the objective of addressing the issue of whether or not the structure of the turbulence in this wall-bounded flow is universal and depends on Mach number. The last chapter of this part investigates the behavior of an extended scaling for turbulent flows including a streamwise pressure gradient.

# Part I

# Code and problem presentation

# CHAPTER 2

# Compressible Navier-Stokes solver

In this chapter a method for large-eddy simulation for turbulent channel flow is discussed. The analysis starts with the governing equations and a description of the numerical method. Two different source term formulations are presented: first the classical extension of the incompressible configuration by *Coleman et al.* [14], second a formulation presently derived to model both streamwise pressure drop and streamwise internal energy loss in a spatially developing compressible channel flow.

Inflow and outflow boundary conditions are discussed for a subsonic compressible turbulent flow based on the method of characteristics.

A method to get turbulent separation in incompressible flows using an adverse pressure gradient artificially implemented in the Navier-Stokes equations [32] is presently extended to compressible flows.

The non-dimensional compressible Navier-Stokes solver used in this study has been developed first at L.E.G.I. (University of Grenoble) [20] and second at I.M.F.S. (University of Strasbourg) [31].

## 2.1 Governing equations

The equations of motion for a compressible fluid are the Navier-Stokes equations presently written in a conservative form (apart from the source terms),

$$\frac{\partial \rho}{\partial t} + \frac{\partial (\rho u_j)}{\partial x_j} = 0 \tag{2.1}$$

$$\frac{\partial (\rho u_i)}{\partial t} + \frac{\partial}{\partial x_j}(\rho u_i u_j + p\delta_{ij} - \mu S_{ij}) = f_i \tag{2.2}$$

$$\frac{\partial (\rho e)}{\partial t} + \frac{\partial}{\partial x_j}\left[(\rho e + p)u_j - \mu S_{ij} u_i - \lambda \frac{\partial T}{\partial x_j}\right] = \mathcal{W} \tag{2.3}$$

and which assume conservation of mass, momentum and total energy of the flow within the computational domain.

The total energy (for a perfect gas) and the traceless strain rate tensor are defined as, respectively

$$\begin{aligned} \rho e &= \rho c_v T + \frac{1}{2}\rho u_i^2 \qquad (2.4)\\ S_{ij} &= \frac{\partial u_i}{\partial x_j} + \frac{\partial u_j}{\partial x_i} - \frac{2}{3}\frac{\partial u_k}{\partial x_k}\delta_{ij} \qquad (2.5)\end{aligned}$$

The equation of state (ideal gas law)

$$p = \rho R T \qquad (2.6)$$

closes the system of equations describing compressible fluid flow.

$f_i$ and $\mathcal{W}$ are source terms for the momentum and energy equations, respectively (for example: gravity, heat source or sink, etc). For these source terms, we will only consider forces in the streamwise direction, $f_i = f\delta_{i1}$, and they will be further defined in Section 2.3.

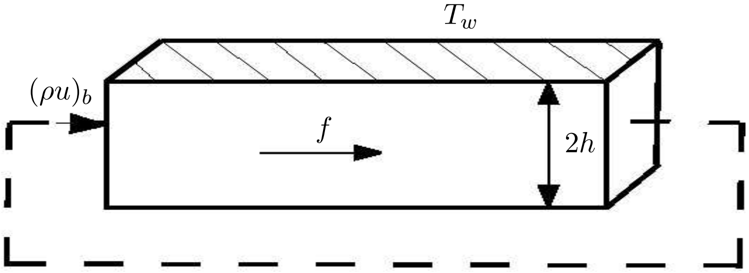

Figure 2.1: **Geometry of the periodical channel flow**

The flow geometry is shown in Figure 2.1. The fluid is assumed to be an ideal gas (air) with constant ratio of specific heats $\gamma = \frac{c_p}{c_v} = 1.4$, $R = c_p - c_v = 287 JKg^{-1}K^{-1}$ and constant Prandtl number $Pr = 0.7$. Isothermal-wall boundary conditions are imposed.

The equations (2.1)-(2.3) are non-dimensionalized by the wall temperature $T_w$, the channel half-width $h$, the bulk-averaged density $\rho_b = \frac{1}{2h}\int_{-h}^{+h} \rho dy$, and the bulk mass flux $(\rho u)_b = \frac{1}{2h}\int_{-h}^{+h} \rho u dy$. The non-dimensional governing equations read then in a flux form

$$\frac{\partial U}{\partial t} + \frac{\partial E}{\partial x} + \frac{\partial F}{\partial y} + \frac{\partial G}{\partial z} = S \qquad (2.7)$$

where $U$ is the vector of conservative variables, $U = (\rho,\ \rho u,\ \rho v,\ \rho w,\ \rho e)^t$,
the total flux vectors $\mathcal{F}_i = (E \equiv \mathcal{F}_{i=1}, F \equiv \mathcal{F}_{i=2}, G \equiv \mathcal{F}_{i=3})^t$ in the $i$-direction, respectively

$$\begin{aligned} (\mathcal{F}_i)_1 &= \rho u_i \\ (\mathcal{F}_i)_2 &= \rho u_i u_1 + \frac{1}{\gamma M^2} P\delta_{i1} - \frac{\mu}{Re} S_{i1} \\ (\mathcal{F}_i)_3 &= \rho u_i u_2 + \frac{1}{\gamma M^2} P\delta_{i2} - \frac{\mu}{Re} S_{i2} \\ (\mathcal{F}_i)_4 &= \rho u_i u_3 + \frac{1}{\gamma M^2} P\delta_{i3} - \frac{\mu}{Re} S_{i3} \\ (\mathcal{F}_i)_5 &= u_i(\rho e + P) - \gamma M^2 \frac{\mu}{Re} u_j S_{ij} - \frac{\gamma}{\gamma - 1}\frac{\mu}{RePr}\frac{\partial T}{\partial x_i} \end{aligned}$$

the non-dimensional pressure and the non-dimensional total energy are defined as, respectively

$$P = \rho T \tag{2.8}$$

$$\rho e = \frac{p}{\gamma - 1} + \frac{\gamma M^2}{2}\rho u_i^2 \tag{2.9}$$

and $\mathcal{S}$ the source terms vector, $\mathcal{S} = (0, f, 0, 0, \gamma M^2 W)^t$.

Non-dimensional parameters are the Mach number, defined in terms of the bulk velocity and speed of sound at the wall $M = \frac{(\rho u)_b/\rho_b}{\sqrt{\gamma R T_w}}$, the Reynolds number, based on the bulk mass flux and channel half-width $Re = \frac{(\rho u)_b h}{\mu(T_w)}$, and the Prandtl number. Thermal conductivity $\lambda(T)$ is related to the molecular Prandtl number by

$$Pr = \frac{\nu}{k} = \frac{c_p \mu(T)}{\lambda(T)}.$$

A power law $\mu = \mu(T) = \mu_w (T/T_w)^{0.7}$ is applied for the molecular dynamic viscosity, as a relatively good approximation of the Sutherland law.

## 2.2 Large-Eddy Simulation

The behavior of large scales in turbulent flows strongly depends on the flow geometry and flow parameters, whereas the smaller scales are relatively universal.

In Direct Numerical Simulations (DNS) all scales are computed, which implies a prohibitively large number of mesh points. Therefore, DNSs are currently limited to low-Reynolds-number flows with simple geometry, such as channel flows [43, 14] and boundary layers [82, 30].

Because of the universal behavior of small scales, in Large-Eddy Simulations (LES), these scales of the flow are modeled, while the remaining scales are computed directly using the three-dimensional, time-dependent Navier-Stokes equations [70].

Let $\Delta$ be a characteristic scale of the grid mesh, larger than the Kolmogorov scale, and $G_\Delta$ a low-pass filter of width $\Delta$. Each variable $f(\overrightarrow{x}, t)$ is split into a resolved part

$$\overline{f}(\overrightarrow{x}, t) = \int f(\overrightarrow{y}, t) G_\Delta(\overrightarrow{x} - \overrightarrow{y}) d\overrightarrow{y} = \int f(\overrightarrow{x} - \overrightarrow{y}, t) G_\Delta(\overrightarrow{y}) d\overrightarrow{y} \tag{2.10}$$

and a Subgrid part $f(\overrightarrow{x}, t) - \overline{f}(\overrightarrow{x}, t)$ to be accounted for with a so called Sub-Grid Scale (sgs) model. The effect of this filter is to remove the high wavenumber (due to scales smaller than $\Delta$) fluctuations.

In the context of compressible flows, the density-weighted Favre filter is considered to account for density changes,

$$\tilde{f} = \frac{\overline{\rho f}}{\overline{\rho}} \tag{2.11}$$

Then, the vector of the filtered conservative variables reads

$$\overline{U} = (\bar{\rho},\ \bar{\rho}\tilde{u},\ \bar{\rho}\tilde{v},\ \bar{\rho}\tilde{w},\ \bar{\rho}\tilde{e})^t. \tag{2.12}$$

The resolved filtered dimensionless fluxes are

$$\overline{(\mathcal{F}_i)}_1 = \bar{\rho}\tilde{u}_i \tag{2.13}$$

$$\overline{(\mathcal{F}_i)}_2 = \bar{\rho}\tilde{u}_i\tilde{u}_1 + \frac{1}{\gamma M^2}\varpi\delta_{i1} - \left(\frac{\tilde{\mu}}{Re} + \bar{\rho}\nu_{sgs}\right)\tilde{S_{i1}} \tag{2.14}$$

$$\overline{(\mathcal{F}_i)}_3 = \bar{\rho}\tilde{u}_i\tilde{u}_2 + \frac{1}{\gamma M^2}\varpi\delta_{i2} - \left(\frac{\tilde{\mu}}{Re} + \bar{\rho}\nu_{sgs}\right)\tilde{S_{i2}} \tag{2.15}$$

$$\overline{(\mathcal{F}_i)}_4 = \bar{\rho}\tilde{u}_i\tilde{u}_3 + \frac{1}{\gamma M^2}\varpi\delta_{i3} - \left(\frac{\tilde{\mu}}{Re} + \bar{\rho}\nu_{sgs}\right)\tilde{S_{i3}} \tag{2.16}$$

$$\overline{(\mathcal{F}_i)}_5 = \tilde{u}_i(\bar{\rho}\tilde{e} + \varpi) - \gamma M^2\frac{\tilde{\mu}}{Re}\tilde{u}_j\tilde{S_{ij}} - \frac{\gamma}{\gamma - 1}\left(\frac{\tilde{\mu}}{RePr} + \frac{\bar{\rho}\nu_{sgs}}{Pr_{sgs}}\right)\frac{\partial\vartheta}{\partial x_i} \tag{2.17}$$

where $\mu_{sgs}$ and $\lambda_{sgs}$ are the sgs eddy viscosity and the sgs eddy diffusivity, respectively. Usually, $\lambda_{sgs}$ is written as $\lambda_{sgs} = \frac{\mu_{sgs}c_p}{Pr_{sgs}}$ where $Pr_{sgs}$ is the sgs Prandtl number. $Pr_{sgs}$ is assumed constant for the simulations, $Pr_{sgs} \approx 0.6$.

The deviatoric part of the subgrid-stress tensor $\mathcal{T}_{ij} = -\overline{\rho u_i u_j} + \bar{\rho}\tilde{u}_i\tilde{u}_j$ and the subgrid heat-flux vector $\mathcal{Q}_i = -\overline{(\rho e + p)u_i} + (\bar{\rho}\tilde{e} + \varpi)\tilde{u}_i$ have been modeled using Boussinesq's assumptions

$$\tau_{ij} = \mathcal{T}_{ij} - \frac{1}{3}\mathcal{T}_{ll}\delta_{ij} \simeq \bar{\rho}\nu_{sgs}\tilde{S}_{ij} \tag{2.18}$$

$$\mathcal{Q}_i \simeq \bar{\rho}c_p\frac{\nu_{sgs}}{Pr_{sgs}}\frac{\partial\tilde{\vartheta}}{\partial x_i} \tag{2.19}$$

The *macropressure* $\varpi$ and the *macrotemperature* $\vartheta$ introduced by Comte & Lesieur [15] are defined, respectively,

$$\varpi = \bar{p} - \frac{1}{3}\mathcal{T}_{ll} \tag{2.20}$$

$$\vartheta = \tilde{T} - \frac{1}{2c_p\bar{\rho}}\mathcal{T}_{ll} \tag{2.21}$$

The filtered equation of state $\bar{p} = \bar{\rho}R\tilde{T}$, with the assumption that $\mathcal{T}_{ll}$ is negligible in front of $\bar{p}$ [24], then reads

$$\varpi = \bar{\rho}R\vartheta + \frac{3\gamma - 5}{6}\mathcal{T}_{ll} =\simeq \bar{\rho}R\vartheta.$$

Large-Eddy Simulations are performed with an eddy-viscosity and an eddy-diffusivity Sub-Grid Scale (SGS) model based on the Filtered Structure Function (FSF) [58, 21, 53, 22, 52, 54]. It consists in submitting the filtered field to a high-pass-filter, a Laplacian operator disctretized by second-order centered finite differences and iterated three times. It finally yields the eddy-viscosity

$$\nu_{sgs}^{FSF} = 0.0014\, C_K^{-3/2}\, \Delta\langle||\nabla^6\tilde{u}(x + r) - \nabla^6\tilde{u}(x)||^2\rangle_{||r||=\Delta}^{1/2} \tag{2.22}$$

where $C_K = 1.4$ is the Kolmogorov constant. This model has shown to be efficient for solving compressible boundary layers without inhibiting transition the turbulence [21].

## 2.3 Streamwise homogeneity for compressible channel flow

[1] [2] For compressible as for incompressible fully developed turbulent channel flow (Fig. 2.1) one seeks a homogeneous unsteady solution of the primitive variables in the streamwise direction [14, 27, 43, 48, 50, 51, 61, 74].

For the incompressible case, the strategy to drive the flow at constant mass flux $(\bar{\rho}\tilde{u})_b$ consists of adding, on the right hand side (*rhs*) of the momentum equation (2.2), a source term $f$ [43] which can be viewed as a mean favourable pressure gradient $-\frac{d\bar{P}_o}{dx} \geq 0$. This model source term is extended for the compressible case in [14] and the analogy to incompressible flow was only considered "in the sense that the total mass flow through the channel remains constant by adjusting the body force $f$". In a companion paper from [34], it was noted that "the flow is driven by an external body force in order to avoid non-zero streamwise gradients of mean density and pressure". In a recent work, Morinishi et al. [61] also comment that "although the driving force $f$ has the same role for compressible turbulent channel flow, it is not interpreted as the mean pressure gradient, since pressure is given by the state equation. Consequently, the rate of work $\mathcal{W} = \tilde{u}f$ arises in the equation of the filtered total energy and obviously "$f$ does not appear in the internal energy equation" [14].

Indeed, by analogy with the procedure described above for the momentum equation, the strategy to transfer energy to the flow at constant total energy $(\bar{\rho}\tilde{e})_b = (\bar{\rho}\tilde{\epsilon})_b + 1/2(\bar{\rho}\tilde{u}^2)_b$ should consist of adding, on the *rhs* of the total energy equation (2.3), a source term $\mathcal{W}$ which can be viewed as the rate of work produced by a mean streamwise enthalpy flux, $\frac{d(\bar{\rho}\tilde{h})_o}{dx} = \frac{d(\bar{\rho}\tilde{\epsilon})_o}{dx} + \frac{d\bar{P}_o}{dx} = \frac{\gamma}{\gamma-1}\frac{d\bar{P}_o}{dx}$. From these considerations which are a part of the coupling referred to by Morkovin [62] between sound ($\frac{d\bar{P}_o}{dx}$) and thermal fields ($\frac{d(\bar{\rho}\tilde{h})_o}{dx}$), we describe in Section 2.3.2 the procedure we chose to model the energy source term in fully developed compressible channel flow. This procedure differs from the classical one and it is better supported by the above arguments in the sense that it constitutes a realistic model for spatially developed compressible channel flow. The flow fields computed with either formulation will be compared in Chapter 4.

### 2.3.1 Momentum source term $f$

Once the flow in a channel has reached a fully developed state, inertial forces in the channel are balanced by the wall friction forces,

$$\frac{d\bar{P}_0}{dx} = -\frac{\tau_w}{h} = -\frac{1}{h}\mu_w\frac{\partial\tilde{u}}{\partial y}|_w \tag{2.23}$$

The pressure is split into non-homogeneous and homogeneous contributions

$$p = \bar{P}_0(x) + \bar{p}(x, y, z, t) \tag{2.24}$$

and introduced in the momentum equation (2.2). When the momentum equations are written in a primitive form [14, 43, 61], which is not the present case, the mean pressure drop contribution

---

[1] N.B. This section is part of the paper [8]:

Brun, C., Petrovan Boiarciuc, M., Haberkorn, M. and Comte, P., *Large eddy simulation of compressible channel flow. Arguments in favour of universality of compressible turbulent wall bounded flows.*, Theor. Comput. Fluid Dyn., 2008

[2] In the present section we consider Navier-Stokes equations with full dimension for clarity purpose with respect to a discussion on source term budgets.

is modeled based on a body force,

$$f_{body} = -\frac{1}{\bar{\rho}}\frac{\partial \bar{P}_0}{\partial x} \tag{2.25}$$

which is used to transform the real spatially evolving problem in which the mean pressure is linearly decreasing into a periodical problem (Fig. 2.1) in which all the variables are homogeneous in the streamwise direction. When the momentum equations are written in conservative form (present case), a mass-weighted force $f$ is applied instead of a body force [48, 51, 74],

$$f = -\frac{\partial \bar{P}_0}{\partial x} \tag{2.26}$$

### 2.3.2 Energy source term $\mathcal{W}$

For compressible channel flow, it is customary to consider the source term $f$ in the momentum equation as an external force to the flow system. When the total energy equation is written in a conservative force, the source term $\mathcal{W}$ is the work of the external force $f$ [51, 74],

$$\mathcal{W}_{ext} = \tilde{u} f = -\tilde{u}\frac{\partial \bar{P}_0}{\partial x} \tag{2.27}$$

For the primitive formulation of the total energy equation [31], the source term reads

$$\mathcal{W}_{body} = \tilde{u} f_{body} = -\frac{\tilde{u}}{\bar{\rho}}\frac{\partial \bar{P}_0}{\partial x} \tag{2.28}$$

and for the temperature equation [14] or for the internal energy equation [61], there is no source term $\mathcal{W} = 0$.

The mean internal energy $(\bar{\rho}\tilde{\epsilon})_o = \frac{1}{\gamma-1}\bar{P}_0$ is not a homogeneous quantity in the streamwise direction for a compressible channel flow. Based on the present analysis, we propose an alternative strategy to the classical one described above which consists of deriving a source term by seeking a homogeneous velocity and density solution for the full compressible Navier-Stokes equations (2.1-2.3), in a similar way as is performed on the momentum equation for incompressible case. In the present case pressure and thus internal energy (which directly affects the temperature) are split into homogeneous and non-homogeneous contributions

$$p = \bar{P}_0(x) + \bar{p}(x,y,z,t) \tag{2.29}$$

$$\rho\epsilon = (\bar{\rho}\tilde{\epsilon})_o + \bar{\rho}\tilde{\epsilon}(x,y,z,t) \tag{2.30}$$

$$\rho T = (\bar{\rho}\tilde{T})_o + \bar{\rho}\tilde{T}(x,y,z,t) \tag{2.31}$$

while density is considered as homogeneous in the streamwise direction, which is consistent with both the continuity equation and the ideal gaz law. Consequently, the corresponding source term

$$W_{int} = \tilde{u} f + \frac{1}{\gamma-1}\tilde{u} f = -\frac{\gamma}{\gamma-1}\tilde{u}\frac{d\bar{P}_0}{dx} = -\tilde{u}\frac{d(\bar{\rho}\tilde{h})_0}{dx} \geq W_{ext} \tag{2.32}$$

is not equivalent to the work of an external force and $\bar{\rho}\tilde{T}$ can be homogeneous. The fully developed state of the flow is then reached when there is a balance between streamwise enthalpy fluxes in the channel (which are related to the mean favourable streamwise pressure gradient), and wall normal heat flux, and reads based on (2.3) and (2.32),

$$-\tilde{u}_b\frac{d(\bar{\rho}\tilde{h})_0}{dx} = -\frac{\gamma}{\gamma-1}\tilde{u}_b\frac{dP_0}{dx} = -\frac{q_w}{h} = \frac{1}{h}\lambda\frac{\partial \tilde{T}}{\partial y}|_w > -\tilde{u}_b\frac{dP_0}{dx} \tag{2.33}$$

This relation differs from the one specific to the classical $\mathcal{W}_{body}$-$\mathcal{W}_{ext}$ case, for which it is assumed that $\frac{d\tilde{T}_0}{dx} = 0$, and thus "an overall energy balance requires that the heat transfer into the walls equals the total pressure work done across the channel" [34].

In the present formulation the pressure drop affects directly the streamwise evolution of the thermodynamic pressure. A significant mean internal energy loss is induced $\frac{d(\bar{\rho}\tilde{e})_o}{dx} = \frac{1}{\gamma-1}\frac{d\bar{P}_0}{dx}$, and thus a negative streamwise temperature gradient appears and is compensated by wall heat flux. Since density is assumed to be homogeneous, the mean temperature gradient can be expressed at the wall by

$$\frac{dT_{wx}}{dx} = \frac{1}{\rho_w}\frac{d\bar{P}_0}{dx} \tag{2.34}$$

and

$$\frac{\tilde{T} - T_{wx}}{T_{wx}} = \frac{\rho_w - \overline{\rho}}{\overline{\rho}} \tag{2.35}$$

is homogeneous.

## 2.4 Computational details

We take advantage of the conservative form of the lhs of the Navier-Stokes equations (2.7), which are further discretised on a cartesian collocated grid at each time step $n$,

$$\frac{U^{n+1}_{i,j,k} - U^{n}_{i,j,k}}{\Delta t} + \frac{E^{n}_{i+\frac{1}{2},j,k} - E^{n}_{i-\frac{1}{2},j,k}}{\Delta x} + \frac{F^{n}_{i,j+\frac{1}{2},k} - F^{n}_{i,j-\frac{1}{2},k}}{\Delta y} + \frac{G^{n}_{i,j,k+\frac{1}{2}} - G^{n}_{i,j,k-\frac{1}{2}}}{\Delta z} = S^n \tag{2.36}$$

where $U$ are the conservative variables and $S$ the source terms. The discretisation of the fluxes ($E \equiv \mathcal{F}_1$, $F \equiv \mathcal{F}_2$, $G \equiv \mathcal{F}_3$) in each direction is performed based on an extension of a fully explicit Mc Cormack scheme, modified by Gottlieb & Turkel [29] to get second order in time and fourth order in space. It is a generalized Lax-Wendroff scheme.

The time advancement is split in two steps, a predictor and a corrector step, respectively,

$$\begin{aligned} U^{n+\frac{1}{2}}_{i,j,k} = U^{n}_{i,j,k} \quad &- \quad \Delta t \left[\frac{-E^{n}_{i+2,j,k} + 8E^{n}_{i+1,j,k} - 7E^{n}_{i,j,k}}{6\Delta x}\right] \\ &- \quad \Delta t \left[\frac{-F^{n}_{i,j+2,k} + 8F^{n}_{i,j+1,k} - 7F^{n}_{i,j,k}}{6\Delta y}\right] \\ &- \quad \Delta t \left[\frac{-G^{n}_{i,j,k+2} + 8G^{n}_{i,j,k+1} - 7G^{n}_{i,j,k}}{6\Delta z}\right] + \Delta t S^n \end{aligned} \tag{2.37}$$

$$\begin{aligned} U^{n+1}_{i,j,k} = \frac{1}{2}\left[U^{n+\frac{1}{2}}_{i,j,k} + U^{n}_{i,j,k}\right] \quad &- \quad \frac{\Delta t}{2}\left[\frac{7E^{n}_{i,j,k} - 8E^{n}_{i-1,j,k} + E^{n}_{i-2,j,k}}{6\Delta x}\right] \\ &- \quad \frac{\Delta t}{2}\left[\frac{7F^{n}_{i,j,k} - 8F^{n}_{i,j-1,k} + F^{n}_{i,j-2,k}}{6\Delta y}\right] \\ &- \quad \frac{\Delta t}{2}\left[\frac{7G^{n}_{i,j,k} - 8G^{n}_{i,j,k-1} + G^{n}_{i,j,k-2}}{6\Delta z}\right] + \frac{\Delta t}{2} S^n \end{aligned} \tag{2.38}$$

which results in a globally centered fourth order scheme.

This predictor-corrector scheme is valid only for the inner points, excepting the two last points in each direction. For these points, the derivatives are defined by Kennedy & Carpenter

[40], respectively

$$\frac{\partial \mathcal{F}_i}{\partial x_i}|_1 = \frac{1}{6\Delta x_i}(-11\mathcal{F}_i|_1 + 18\mathcal{F}_i|_2 - 9\mathcal{F}_i|_3 + 2\mathcal{F}_i|_4) \tag{2.39}$$

$$\frac{\partial \mathcal{F}_i}{\partial x_i}|_2 = \frac{1}{6\Delta x_i}(-2\mathcal{F}_i|_1 - 3\mathcal{F}_i|_2 + 6\mathcal{F}_i|_3 - \mathcal{F}_i|_4) \tag{2.40}$$

$\mathcal{F}_i|_j$ is the flux in $i$-direction at the point $x_j$. The indices 1, 2, 3, 4 correspond to the boundary points and the three next points in the $i$-direction, respectively. This stencil will be applied only for the free boundaries.

The computing time step is determined based on both a CFL (Courant-Friedrichs-Levy) and a viscous stability criterion which must both be considered for the present wall-bounded compressible flow.

Numerical instabilities may occur because the time step is too large to resolve the propagation of internal waves. Therefore, the CFL criterion yields

$$\Delta t = C_{CFL}\, max\left(\frac{\Delta x}{|u|+c}, \frac{\Delta y}{|v|+c}, \frac{\Delta z}{|w|+c}\right) \tag{2.41}$$

where $c$ is the speed of sound, and $C_{CFL}$ is a constant which based on the grid discretization is set to 0.4 in the present case.

Time step limitation due to viscosity and diffusivity (the case of very fine grids, near the wall, for example, of a very low Reynolds number flows) read

$$\Delta t = C_{vis}\, max\left(\frac{\Delta x^2}{\nu}, \frac{\Delta y^2}{\nu}, \frac{\Delta z^2}{\nu}\right) \tag{2.42}$$

where $C_{vis}$ is set to 0.2.

Among the two criterions the minimum is chosen as the computing time step.

## 2.5 Inflow and outflow conditions

Most turbulence simulations are performed by assuming periodic boundary conditions and flow periodicity, implicitly. For simulations in which no periodicity is assumed, conditions at flow inlets and outlets must be prescribed. These simulations are strongly dependent on boundary conditions and on their treatment.

In the present study, two configurations are considered (Figure 2.2):

- the first one, with periodic boundary conditions in the streamwise direction (*T-configuration*);

- for the second one, a fully developed channel flow with streamwise periodic boundary conditions (domain 1) is used in order to ensure realistic inflow conditions for domain 2. This procedure is necessary to develop time dependent realistic turbulent structures which will trigger transition to turbulence in the main domain (if necessary), but it is also very expensive since the preliminary domain must be large enough to get streamwise decorrelation and well resolved to describe small turbulent structures. Non-reflecting outflow conditions based on wave decomposition [46],[68] are applied at the outlet of domain 4 (*S-configuration*).

For specifying boundary conditions we use the characteristic analysis described by Thompson in [86], [87] for Euler equations, and generalized to the viscous-diffusive Navier-Stokes equations by Poinsot & Lele [68]. It consists in decomposing hyperbolic equations into wave modes of

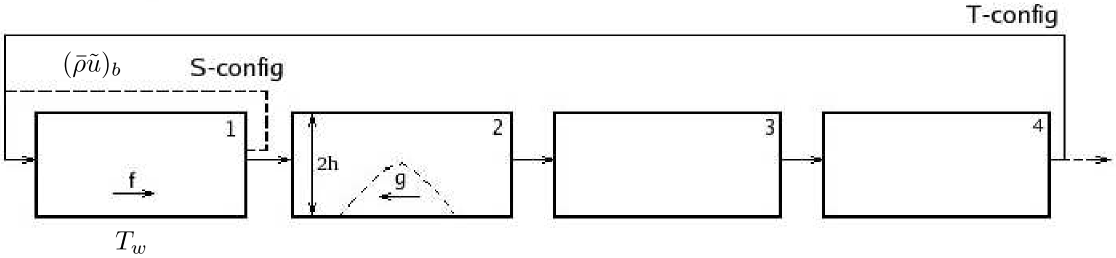

Figure 2.2: **Geometry of the separating channel flow**

velocity. This characteristic analysis makes clear which waves are propagating into and out of the computational domain. The behavior of the outward propagating waves is defined entirely by the solution at and within the boundary, whereas the inward propagating waves are specified as boundary conditions.

The Navier-Stokes equations (2.7) are converted to an equivalent set of wave equations, which represent nonlinear waves propagating at characteristic velocities in the $x$-direction only, as

$$\begin{aligned}
\frac{\partial \rho}{\partial t} &+ d_1 + \frac{\partial}{\partial y}(\rho v) + \frac{\partial}{\partial z}(\rho w) = 0 && (2.43)\\
\frac{\partial(\rho u)}{\partial t} &+ u d_1 + \rho d_3 + \frac{\partial}{\partial y}(\rho u v) + \frac{\partial}{\partial z}(\rho u w) = \frac{1}{Re}\frac{\partial(\mu S_{1j})}{\partial x_j} && (2.44)\\
\frac{\partial(\rho v)}{\partial t} &+ v d_1 + \rho d_4 + \frac{\partial}{\partial y}(\rho v v + \frac{1}{\gamma M^2} p) + \frac{\partial}{\partial z}(\rho v w) = \frac{1}{Re}\frac{\partial(\mu S_{2j})}{\partial x_j} && (2.45)\\
\frac{\partial(\rho w)}{\partial t} &+ w d_1 + \rho d_5 + \frac{\partial}{\partial y}(\rho w v) + \frac{\partial}{\partial z}(\rho w w + \frac{1}{\gamma M^2} p) = \frac{1}{Re}\frac{\partial(\mu S_{3j})}{\partial x_j} && (2.46)\\
\frac{\partial(\rho e)}{\partial t} &+ \gamma M^2\left[\frac{1}{2}(u_k u_k) d_1 + \rho u d_3 + \rho v d_4 + \rho w d_5\right] && (2.47)\\
&+ \frac{\partial}{\partial y}\left[(\rho e + p) v\right] + \frac{\partial}{\partial z}\left[(\rho e + p) w\right]\\
&= \frac{\partial}{\partial x_j}\left(\gamma M^2 \frac{\mu}{Re} u_i S_{ij} + \frac{\gamma}{\gamma - 1}\frac{\mu}{RePr}\frac{\partial T}{\partial x_j}\right)
\end{aligned}$$

The characteristic velocities are given as the solution of the eigenvalue problem and are

$$\begin{aligned}
\lambda_1 &= u - c_{norm}\\
\lambda_2 &= \lambda_3 = \lambda_4 = u && (2.48)\\
\lambda_5 &= u + c_{norm}
\end{aligned}$$

where $c_{norm}$ is the normalized speed of sound, $c_{norm}^2 = \frac{1}{\gamma M^2}\frac{\gamma p}{\rho} = \frac{\gamma p_{norm}}{\rho}$. The normalized pressure $p_{norm}$ is defined alike. $\lambda_1$ and $\lambda_5$ are the velocities of sound waves moving in the negative and positive $x$-directions, $\lambda_2$ is the convection velocity (the speed of entropy waves) while $\lambda_3$ and $\lambda_4$ are the velocities at which $v$ and $w$ are advected in the $x$-direction.

The system of Eqs. (2.43)-(2.47) includes derivatives normal to the $x = 0$ or $L_x$-boundary ($d_1$ to $d_5$), derivatives parallel to the $x = 0$ or $L_x$-boundary like $(\frac{\partial}{\partial y})(\rho v v)$ and local viscous terms. The vector **d** is given by characteristic analysis and is expressed as

$$d = \left( \begin{array}{c} \frac{1}{c_{norm}^2}\left[L_2 + \frac{1}{2}(L_5 + L_1)\right] \\ \frac{1}{2}(L_5 + L_1) \\ \frac{1}{2\rho c_{norm}}(L_5 - L_1) \\ L_3 \\ L_4 \end{array} \right) = \left( \begin{array}{c} \frac{\partial(\rho u)}{\partial x} \\ \frac{\partial}{\partial x}(c_{norm}^2 \rho u) + (1-\gamma) u \frac{\partial p_{norm}}{\partial x} \\ u\frac{\partial u}{\partial x} + \frac{1}{\rho}\frac{\partial p_{norm}}{\partial x} \\ u\frac{\partial v}{\partial x} \\ u\frac{\partial w}{\partial x} \end{array} \right) \tag{2.49}$$

where the $L_i$'s are the amplitudes of characteristic waves associated with each characteristic velocity $\lambda_i$. The $L_i$'s are given by:

$$L_1 = \lambda_1 \left( \frac{\partial p}{\partial x} - \rho c_{norm} \frac{\partial u}{\partial x} \right) \tag{2.50}$$

$$L_2 = \lambda_2 \left( c_{norm}^2 \frac{\partial \rho}{\partial x} - \frac{\partial p}{\partial x} \right) \tag{2.51}$$

$$L_3 = \lambda_3 \frac{\partial v}{\partial x} \tag{2.52}$$

$$L_4 = \lambda_4 \frac{\partial w}{\partial x} \tag{2.53}$$

$$L_5 = \lambda_5 \left( \frac{\partial p}{\partial x} + \rho c_{norm} \frac{\partial u}{\partial x} \right) \tag{2.54}$$

The time variation of the primitive flow variables can be expressed based on the $L_i$'s as

$$\frac{\partial \rho}{\partial t} + \frac{1}{c_{norm}^2}\left[L_2 + \frac{1}{2}(L_5 + L_1)\right] = 0 \tag{2.55}$$

$$\frac{\partial u}{\partial t} + \frac{1}{2\rho c_{norm}}(L_5 - L_1) = 0 \tag{2.56}$$

$$\frac{\partial v}{\partial t} + L_3 = 0 \tag{2.57}$$

$$\frac{\partial w}{\partial t} + L_4 = 0 \tag{2.58}$$

$$\frac{\partial p}{\partial t} + \frac{1}{2}(L_5 + L_1) = 0 \tag{2.59}$$

$$\frac{\partial T}{\partial t} + \frac{T}{\rho c_{norm}^2}\left[-L_2 + \frac{1}{2}(\gamma - 1)(L_5 + L_1)\right] = 0 \tag{2.60}$$

All gradients normal to the boundary may also be expressed in terms of the $L_i$'s

$$\frac{\partial \rho}{\partial x} = \frac{1}{c_{norm}^2}\left[\frac{L_2}{u} + \frac{1}{2}\left(\frac{L_5}{u + c_{norm}} + \frac{L_1}{u - c_{norm}}\right)\right] \tag{2.61}$$

$$\frac{\partial p}{\partial x} = \frac{1}{2}\left(\frac{L_5}{u + c_{norm}} + \frac{L_1}{u - c_{norm}}\right) \tag{2.62}$$

$$\frac{\partial u}{\partial x} = \frac{1}{2\rho c_{norm}}\left(\frac{L_5}{u + c_{norm}} - \frac{L_1}{u - c_{norm}}\right) \tag{2.63}$$

$$\frac{\partial T}{\partial x} = \frac{T}{\rho c_{norm}^2}\left[-\frac{L_2}{u} + \frac{1}{2}(\gamma - 1)\left(\frac{L_5}{u + c_{norm}} + \frac{L_1}{u - c_{norm}}\right)\right] \tag{2.64}$$

We use the system of Eqs. (2.43)-(2.47) to obtain the values of variables at the boundary for the immediately following time step by estimating the amplitude variation $L_i$'s of waves propagating into the domain.

The knowledge of the conditions ensuring well-posedness of the Navier-Stokes equations is not sufficient for the discretization and implementation of boundary conditions. Poinsot & Lele distinguished two types of conditions [68]:

- "physical", inviscid or/and viscous, boundary conditions, which specify the known physical behavior of one or more of the dependent variables. These conditions are independent of the numerical method used to solve the governing equations.
- "soft" or "numerical" boundary conditions are needed when the number of physical boundary conditions is less than the number of primitives variables (this is always the case at an outflow). These additional conditions should be viewed as compatibility relations required by the numerical method and not as boundary conditions.

### 2.5.1 A subsonic inflow

At the inlet, it was chosen to impose the velocities, $u$, $v$ and $w$, as well as the temperature, $T$, using the solution of the fully-developed channel flow, domain 1. The only remaining unknown is the density $\rho$ which can be obtained through the continuity equation. This case of inflow does not require any viscous condition, the total number of boundary conditions being four. From a numerical point of view, we have four physical conditions (for $u$, $v$, $w$ and $T$) and one soft condition (for $\rho$).

For a subsonic three-dimensional flow, the only characteristic variable $L_1$ propagates against the flow direction, while the other four, $L_2$, $L_3$, $L_4$ and $L_5$, are entering the domain. Therefore, $L_1$ needs to be computed from the interior of the spatially developing channel using Eq. (2.50). The entering characteristic variables $L_5$ and $L_2$ are estimated using Eqs. (2.56) and (2.60), respectively

$$L_5 = L_1 - 2\rho c_{norm}\frac{\partial u}{\partial t} \tag{2.65}$$

$$L_2 = \frac{1}{2}(\gamma - 1)(L_5 + L_1) + \frac{\rho c_{norm}^2}{T}\frac{\partial T}{\partial t} \tag{2.66}$$

The density is avanced in time using Eq. (2.43) and thus, it is strongly coupled to both velocity and temperature fluctuations in the periodical channel. Consequently, it is very important to use an accurate model for the inflow channel, source terms implicitly (Section 2.3).

The entering characteristic variables $L_3$ and $L_4$ are not needed in this case of inflow.

### 2.5.2 A subsonic outflow

For non-reflecting subsonic outflow, one physical condition is needed for the Euler equations. This condition states that the pressure has to be imposed at infinity so that waves reflected from infinity towards the computational domain should have a zero amplitude. For the Navier-Stokes equations, three viscous conditions have to be added [10, 68]

$$\frac{\partial(\mu S_{12})}{\partial x} = 0 \tag{2.67}$$

$$\frac{\partial(\mu S_{13})}{\partial x} = 0 \tag{2.68}$$

$$\frac{\partial}{\partial x}\left(\mu\frac{\partial T}{\partial x}\right) = 0 \tag{2.69}$$

They are implemented numerically by simply setting them to zero in the system of Eqs. (2.43)-(2.47).

Considering a three-dimensional subsonic outlet, characteristic waves leaving the domain, $L_2$ to $L_5$, are computed using Eqs. (2.51) to (2.54), respectively. The incoming wave $L_1$ is modeled. When it is possible to determine an exact value $L_1^{exact}$ of $L_1$, Poinsot & Lele suggested to set

$$L_1 = K(p - p_\infty) + L_1^{exact} \tag{2.70}$$

The expression of the constant, $K = \sigma(1 - M^2)c/L$, with $M$ the maximum Mach number in the flow, $L$ a characteristic size of the domain and $\sigma$ a constant, is the one proposed by Rudy & Strikwerda [72], [73]. When $\sigma = 0$, the amplitude of reflected waves is set to 0. This is the so called 'perfectly non-reflecting' method.

In the present work, based on the pressure drop modelled in the periodic inflow channel as a constant force $f = -\frac{\partial p_{norm}}{\partial x}$, we propose the following expression as an exact value $L_1^{exact}$ of $L_1$

$$L_1^{exact} = -\sigma(1 - M_l^2)c_{norm}f \tag{2.71}$$

where $M_l$ is the local Mach number. The constant $\sigma$ is set to $\sigma = \frac{1}{1+M_l}$.

Finally, the characteristic variable $L_1$ is modelled as

$$L_1 = (1 - M_l)c_{norm}\left[\frac{p - p_\infty}{L} - f\right] \tag{2.72}$$

Thus, the second term ensures an accurate matching of derivatives between both sides of the boundary (pressure drop), while the first term keeps the mean values of the pressure around $p_\infty$.

## 2.6 Artificial distortion of the wall layer

The distortion of the flow in the channel is generated by applying a distributed force $g$ against the streamwise direction within the domain of an equilibrium channel flow (domain 2, Fig. 2.2) and the outgoing flow readjusts to the new conditions. This distributed force per unit area is equivalent to a local adverse pressure gradient.

In order to get an incompressible separated turbulent flow, R. Howard [32] [3] used a distributed force of the following expression

$$F(x,y) = C\,sin\left(2\pi\frac{x}{h}\right)tanh\left(5\frac{y}{h}\right) \tag{2.73}$$

for $0 < x < \frac{L_x}{3}$ and $F(x,y) = 0$ for $\frac{L_x}{3} < x < L_x$. The constant was set to $C = 40$. Thus, the distributed force varies sinusoidally in the streamwise direction between $0 < x < \frac{L_x}{3}$. The *tanh* function in the wall normal direction is used to reverse the sign of the forcing in order to satisfy continuity, Fig. 2.3(a).

---

[3] The Howard's test case was simulated with a friction Reynolds number of $Re_\tau = 130$ and using periodical boundary conditions in the streamwise direction. *'The simulation was shown to generate a mild separation region of the upper surface of the channel and a small but strong separation bubble on the lower surface. Upstream of the separation, the flow underwent a strong acceleration which caused laminarescent flow and streak elongation. Just downstream of the mean separation point the streak structures were completely destroyed and the anisotropy map showed the turbulence to be close to the axisymmetric contraction limit near the wall.This persisted far downstream beyond the mean reatachment point. Turbulence budgets showed that the flow in the vicinity of the separation bubble was very energetic with maximum turbulence production more than ten times the plane channel flow value. Budgets and anisotropy profiles in the recovery region showed the turbulence to be at similar levels to steady channel flow. Instantaneous visualization also showed the regeneration of streaks in this region.'*

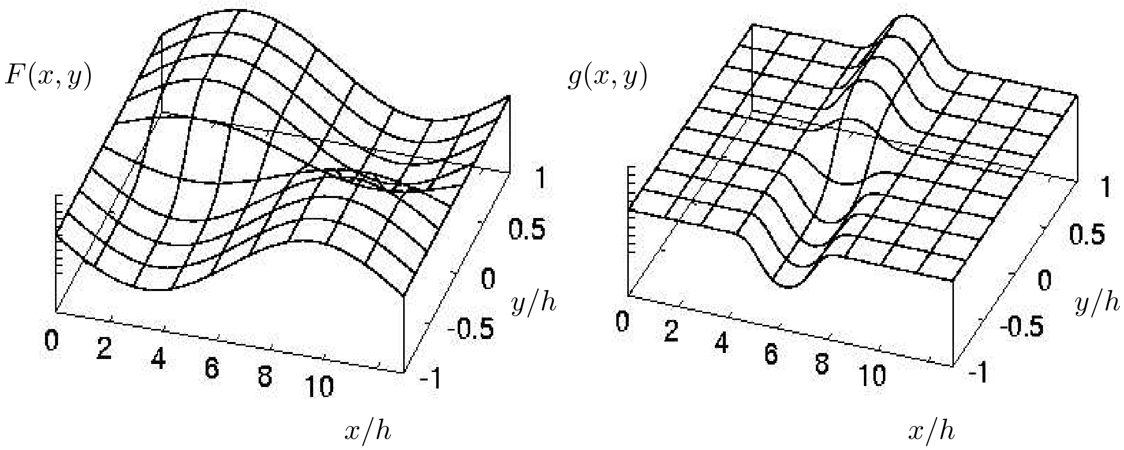

(a) Howard's distributed force $F$ (b) distributed force $g$

Figure 2.3: **Distribution of the streamwise adverse pressure gradient.**

In the present work, we have chosen a distributed force of the following expression,

$$g(x,y) = C\,exp\left[-0.4\left(\frac{x}{h}-2\pi\right)^2 - 0.2\left(\frac{x}{h}-2\pi\right)^4\right] tanh\left(5\frac{y}{h}\right) \tag{2.74}$$

for $\frac{L_x}{6} < x < \frac{L_x}{3}$ and $g(x,y) = 0$ for $0 < x < \frac{L_x}{6}$ and $\frac{L_x}{3} < x < L_x$, 2.3(b). The *tanh* function in the wall normal direction was kept and the *sin* function in the streamwise direction was replaced by an *exp* function. Computations were carried out with the constant set to $C = 10$.

This force $g$ replace the force $f$ in the source terms in the Navier-Stokes equations (2.1 to 2.3).

## 2.7 Parallelization and optimization of the code

Within the present study, it was planned to investigate the near wall behavior for turbulent compressible wall layers involving separation. The ultimate goal of the study is to develop wall models for complex flow situations including separation, compressibility, and turbulence. This goal can only be successfully achieved if simulations are done on a sufficiently large domain and an adequate resolution to allow for basic and reliable studies of the near wall physics of such flows. Therefore the parallelization and the optimization of the code were essential. [4]

A typical run of a non-separating flow takes about 200 hours of CPU-time on the IDRIS's NEC SX-5 or SX-8 platforms. The separating flow requires a computational domain which is at least four times larger. In addition, a slightly higher grid resolution is necessary in the region around the distortion.

Consequently, the parallelization was done based on the exisiting multiblock structure of the code. The platform for parallelization was the NEC SX-8 at the HLRS in Stuttgart because only minor modifications were necessary for porting the code from NEC SX-5 to NEC SX-8.

---

[4] The code used was parallelized by the Message Passing Interface (MPI) implementation during a first HPC-Europa stay at the Fachgebiet Hydromechanik of Technische Universität München and optimized during a second HPC-Europa visite at the HLR Stuttgart. The main computing resources were assured by the HLR Stuttgart.

Nevertheless, a serial optimization was performed for making efficient use of the hardware.

The parallelization of the code was made using the Message Passing Interface (MPI) implementation [1]. Due to the multiblock structure of the code, it was chosen to compute one block per processor. Point-to-point communication subroutines (as MPI_SENDRECV, MPI_SEND, MPI_RECV) were used to exchange information from a processor (block) to its neighbours. To compute the minimum time step of all processors, MPI_REDUCE collective comunication subroutine was used. Another collective comunication subroutine, MPI_BCAST was used to share some information with the first processor, e.g. the $f$ force.

Computations for both T- and S-configurations have been performed on the HLRS's NEC SX-8. In Table 2.1, the number of grid points and the one processor (serial) time per time steps for each of these tests are presented. The speed-up achieved by parallelisation on 2, 4 and 8 processors is reported in Figure 2.4. The result is satisfactory and further optimization was done.

| | | 1 | 2 | 4 | 8 |
|---|---|---|---|---|---|
| grid points | | 673920 | 1347840 | 2695680 | 5391360 |
| serial time/time steps (sec) | T-conf | 0.09 | 0.2 | 0.4 | 0.8 |
| | S-conf | – | 0.22 | 0.42 | 0.82 |

Table 2.1: **Grid points number and serial time per time steps of the tests done**

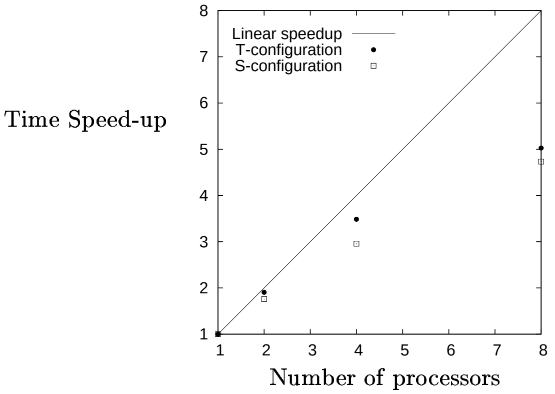

Figure 2.4: **Speed-up relative to CPU time on 1 processor**

An important issue in optimization was to minimize the time spent for communication. Processors communication visualization was possible using the PARAVER software. One time step parallel run on four processors is represented in Figures 2.5a (T-configuration) and 2.5b (S-configuration). The color's signification is: blue - running time outside the MPI subroutines, orange - collective communication subroutines (MPI_REDUCE or MPI_BCAST), grey - MPI_SENDRECV point-to-point communication, green - blocking send duration and red - waiting for a message duration. In Table 2.2 are reported the corresponding times in percentage. The global communication time is greater for the S-configuration (80.31% vs 12.63% for T-configuration), so the main optimization effort has been focussed on this configuration.

The most time expensive communication subroutines are MPI_SEND, MPI_RECV and MPI_SENDRECV, therefore it was decided to replace them by

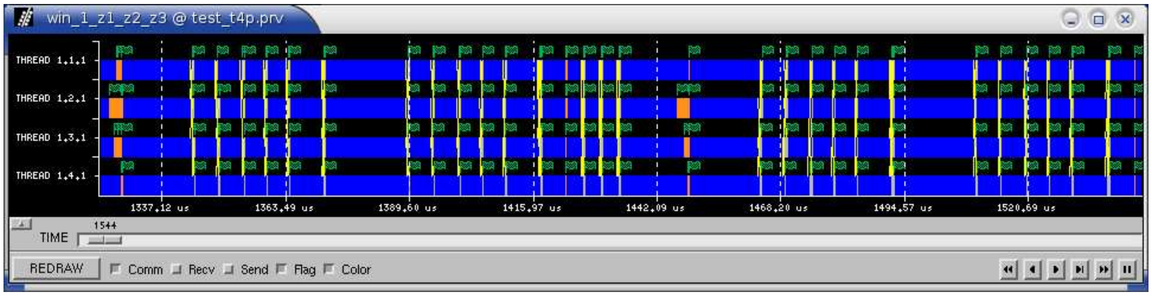

(a) T-configuration

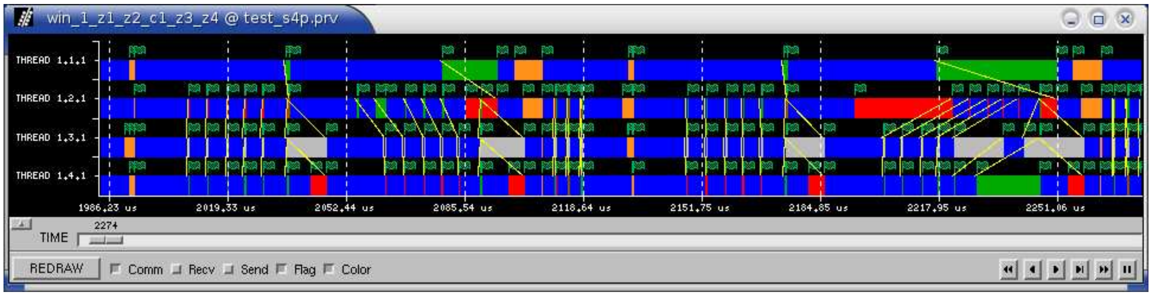

(b) S-configuration

Figure 2.5: **Zoom of the parallel run on 4 processors: T-configuration (a); S-configuration (b).**

| Config. | Thread | Running | Waiting a Message | Blocking Send | Group Communication | Send Receive |
|---|---|---|---|---|---|---|
| T-config. | 1.1.1 | 97.21% | — | — | 0.99% | 1.76% |
| | 1.2.1 | 96.59% | — | — | 1.71% | 1.67% |
| | 1.3.1 | 96.79% | — | — | 1.41% | 1.72% |
| | 1.4.1 | 96.78% | — | — | 1.44% | 1.78% |
| S-config. | 1.1.1 | 75.73% | — | 15.84% | 8.40% | 0.00% |
| | 1.2.1 | 80.78% | 13.21% | 1.46% | 4.54% | 0.00% |
| | 1.3.1 | 75.43% | — | — | 1.33% | 23.24% |
| | 1.4.1 | 87.75% | 5.94% | 4.80% | 1.44% | 0.01% |

Table 2.2: **Time spent for processors comunication**

| S-config. | # processors | 1 | 2 | 4 | 8 |
|---|---|---|---|---|---|
| before optimization | time(secs) | 181.4 | 504.4 | 1144.2 | 2795.8 |
| | speed-up | 1 | 1.76 | 2.96 | 4.72 |
| | rel. speed-up | 1 | 0.88 | 0.74 | 0.59 |
| after optimization | time(secs) | 181.4 | 503.0 | 1052.4 | 2718.6 |
| | speed-up | 1 | 1.76 | 3.21 | 4.86 |
| | rel. speed-up | 1 | 0.88 | 0.8 | 0.61 |

Table 2.3: **Computing times and speed-up of parallel program running on 1 to 8 processors, S-configuration**

MPI_ISEND+MPI_WAIT, MPI_IRECV+MPI_WAIT and MPI_IRECV + MPI_ISEND+MPI_WAIT sequences, respectively. The MPI_WAIT subroutine controls that the desired data is completely transfered from one processor to the other. The impact of these replacements on the speed-up is reported in Table 2.3. Computing times are expressed in seconds for 1771 iterations. We note no significant improvements perhaps due to the vectorial computation.

## 2.8 Statistical analysis

Turbulent flows are complex due to their properties of irregularity or randomness. Analysis revealed that although the instantaneous behavior of such a flow is irregular, there is a general statistical behavior of turbulence that is repeatable. This has led to a statistical description of turbulence. Different types of averaging can be carried out depending on the type of flow field being examined.

The ensemble average $\langle f(x_i,t)\rangle$ is defined as

$$\langle f(x_i,t)\rangle \equiv \lim_{N\to+\infty}\frac{1}{N}\sum_{n=1}^{N} f_n(x_i,t) \tag{2.75}$$

where $f(x_i,t)$ is taken at a given position and time, and $N$ is the number of data points taken.

In flows that are statistically steady, it is possible to use the *ergodic hypothesis* to replace the ensemble averages by time averages. The time average is given by

$$\langle f\rangle_t(x_i) = \lim_{T\to+\infty}\frac{1}{T}\int_t^{t+T} f(x_i,t)dt \tag{2.76}$$

where $T$ is the mean integration time and it must be sufficiently long for the mean to be stationary.

Fully developed channel flows are homogeneous in the streamwise and spanwise directions, thus a spatial average might be defined

$$\langle f\rangle_{x,z}(y,t) = \lim_{L_x,L_z\to+\infty}\frac{1}{L_xL_z}\int_0^{L_x}\int_0^{L_z} f(x,y,z,t)dx\ dz \tag{2.77}$$

In the case of spatially developing flows which are homogeneous only in the spanwise direction, this spatial average is defined

$$\langle f\rangle_z(x,y,t) = \lim_{L_z\to+\infty}\frac{1}{L_z}\int_0^{L_z} f(x,y,z,t)dz \tag{2.78}$$

For compressible flows, both Reynolds averaging and Favre averaging can be used. The Reynolds averaging is a standard (classical) averaging of a quantity f over homogeneous directions, and is used to define a fluctuating part,

$$f' = f - \langle f \rangle \tag{2.79}$$

Consequently, in an LES the dependent variables are decomposed according to: [5]

$$\begin{aligned}
\bar{\rho}' &= \bar{\rho} - \langle \bar{\rho} \rangle && (2.80)\\
\tilde{u}_i' &= \tilde{u}_i - \langle \tilde{u}_i \rangle && (2.81)\\
\tilde{T}' &= \tilde{T} - \langle \tilde{T} \rangle && (2.82)\\
\langle \bar{p} \rangle &= \langle \bar{\rho} R \tilde{T} \rangle && (2.83)
\end{aligned}$$

Favre averaging is a density weighted averaging,

$$\{f\} = \frac{\langle \bar{\rho} f \rangle}{\langle \bar{\rho} \rangle} \tag{2.84}$$

and is used to define a fluctuating part,

$$f'' = f - \{f\} \tag{2.85}$$

Note that $\langle f' \rangle = 0$, and $\langle \bar{\rho} f'' \rangle = 0$ but $\langle \bar{\rho} \rangle \langle f'' \rangle = \langle \rho' f' \rangle = \langle \bar{\rho} \rangle \left( \langle f \rangle - \{f\} \right) \neq 0$. Consequently, the dependent variables are decomposed according to: [6]

$$\begin{aligned}
\tilde{u}_i'' &= \tilde{u}_i - \{\tilde{u}_i\} && (2.86)\\
\tilde{T}'' &= \tilde{T} - \{\tilde{T}\} && (2.87)
\end{aligned}$$

In the Section 4.4 these two averaging procedures will be further compared.

In what follows, all the statistical variables needed for post-processing are listed. These variables are written using the Reynolds averaging and they are similar for the mass-weighted (Favre) averaging.

$$\begin{aligned}
\langle u_i'^2 \rangle &= \langle \tilde{u}_i{}^2 \rangle - \langle \tilde{u}_i \rangle^2 && (2.88)\\
\langle u_i' T' \rangle &= \langle \tilde{u}_i \tilde{T} \rangle - \langle \tilde{u}_i \rangle \langle \tilde{T} \rangle && (2.89)\\
\langle u_i'^3 \rangle &= \langle \tilde{u}_i{}^3 \rangle - 3 \langle \tilde{u}_i \rangle \langle \tilde{u}_i{}^2 \rangle + 2 \langle \tilde{u}_i \rangle^3 && (2.90)\\
\langle u_i'^2 v' \rangle &= \langle \tilde{u}_i^2 \tilde{v} \rangle - 2 \langle \tilde{u}_i \rangle \langle \tilde{u}_i \tilde{v} \rangle - \langle \tilde{u}_i{}^2 \rangle \langle \tilde{v} \rangle + 2 \langle \tilde{u}_i \rangle^2 \langle \tilde{v} \rangle && (2.91)\\
\langle u_i'^4 \rangle &= \langle \tilde{u}_i{}^4 \rangle - 4 \langle \tilde{u}_i \rangle \langle \tilde{u}_i{}^3 \rangle + 6 \langle \tilde{u}_i \rangle^2 \langle \tilde{u}_i{}^2 \rangle - 3 \langle \tilde{u}_i \rangle^4 && (2.92)\\
\langle v' T_i' \rangle &= \langle v' T' \rangle + \frac{Pr_m}{2} (\gamma - 1) M^2 \left( \langle \tilde{u}_i^2 \tilde{v} \rangle - \langle \tilde{u}_i^2 \rangle \langle \tilde{v} \rangle \right) && (2.93)\\
\langle T_i' T_i' \rangle &= \langle T' T' \rangle + Pr_m (\gamma - 1) M^2 \left( \langle \tilde{u}_i^2 \tilde{T} \rangle - \langle \tilde{u}_i^2 \rangle \langle \tilde{T} \rangle \right) && (2.94)\\
&+ \frac{Pr_m^2}{4} (\gamma - 1)^2 M^4 \left( \langle \tilde{u}_i^4 \rangle - \langle \tilde{u}_i^2 \rangle^2 \right) && (2.95)
\end{aligned}$$

where $T_i$ is the total temperature which will be defined in Section 4, Eq. (4.18).

---

[5] For the simplicity of the notation, it will be considered hereafter that: $\bar{\rho}' \approx \rho'$, $\tilde{u}_i' \approx u_i'$, $\tilde{T} \approx T'$. These approximations are valid in the present case because a very high resolved LES is considered.

[6] For the simplicity of the notation, it will be considered hereafter that: $\tilde{u}_i'' \approx u_i'$, $\tilde{T} \approx T''$.

# CHAPTER 3

# Problem description

## 3.1 Flow case description

Because of its geometric simplicity, turbulent channel flow has been studied extensively both experimentally and using direct numerical or large eddy simulations. The aim of this section is to compare the channel flow simulations carried out in this work to previous studies, as shown on Table 3.1.

LES of fully developed compressible channel flow were performed for both source terms $\mathcal{W}_{body}$ (2.28) and $\mathcal{W}_{int}$ (2.32), for Reynolds numbers $Re = \frac{(\bar{\rho}\tilde{u})_b h}{\mu_w} = 3,000$ and $Re = 4,880$ based on bulk mass flux, channel half width and wall temperature. Mach number $M = \frac{(\bar{\rho}\tilde{u})_b/\bar{\rho}_b}{\sqrt{\gamma R T_w}}$ based on bulk velocity and wall temperature is varied in the range $0.3 \leq M \leq 5$ to study compressibility effects as well.

Fully developed turbulent channel flow is homogeneous in the streamwise and spanwise directions, and periodic boundary conditions are used in these directions (Fig. 2.2, $T$-configuration). Therefore, in the homogeneous directions, the computational box has to include the largest eddies in the flow. Jimenez & Moin [38] found the minimum size of the computational box of about $250-350$ wall units in the streamwise direction and about 100 wall units in the spanwise direction.

The size of the computational domain is $L_x$ x $L_y$ x $L_z = 4\pi h$ x $2h$ x $\frac{4}{3}\pi h$ in the streamwise $x$, wall-normal $y$ and spanwise $z$ directions, respectively. The number of grid points is $N_x$ x $N_y$ x $N_z$ = 128 x 65 x 81. Grid spacing in the periodic directions is uniform. An assessment of the grid resolution can be obtained by comparing the non-dimensional grid spacing with other turbulent flows (Table 3.1). The non-dimensional grid spacing is defined as

$$\Delta x_i^+ = \frac{\Delta x_i u_\tau}{\nu_w}$$

the grid spacing is $\Delta x_i = L_i/N_i$, $L_i$ being the box length and $N_i$ the number of grid points in the $i$-direction. The wall-normal collocation points are distributed by using a hyperbolic-tangent type stretching [31]

$$Y_j = A\left(1 - \frac{tanh(g_y * (A - dy * (j-1)))}{tanh(g_y * A)}\right),\ j = 1, Ny + 1$$

where $h$ is the channel half-width, $dy = 2h/Ny$, and $g_y$ a stretching factor. $A$ is fixed to 1 in order to get a symmetrical grid in $y$-direction. There are $N_y + 1$ grid points $Y_j$ and all variables are calculated on $N_y$ grid points

$$y_j = \frac{Y_{j+1} + Y_j}{2}.$$

This special mesh refinement is used to capture the main physical aspects in the near wall region down to $y_w^+ = 0.2$. In this context, the SGS model acts mainly in the core region of the channel where the turbulent flow is fully developed, while at the wall and in the wall normal direction only, the flow is nearly resolved in a DNS sense. Statistics were computed over four to ten channel advection times $L_x/u_b$, using both Reynolds averaging procedures and Favre averaging procedures.

In order to study flow distortion in the turbulent compressible channel, the second configuration is considered (see Section 2.5, Fig. 2.2, $S$-configuration). Simulation with 4 (not shown here) and 7 blocks were performed for a Reynolds number of $Re = 4,880$ and a Mach number of $M = 0.7$. Each block has the same size and the same resolution as the computational domain used for the simulation of fully developed channel flow. The internal forcing presented in Section 2.3 is used.

Since the size of the computational domain is important (around $88h$ in the streamwise direction and the total number of grid points being of $4,717,440$), an important CPU time is needed for each of simulation. Thus, statistics were computed over one to two channel advection times $L_x/u_b$, using Reynolds averaging procedures.

For isothermal-wall channel flow with constant temperature $T_w$, the present case, both a friction velocity based on wall friction and a friction temperature based on wall heat flux [6] are defined, respectively

$$u_\tau = \sqrt{\frac{\tau_w}{\rho_w}} \tag{3.1}$$

$$T_\tau = \frac{-q_w}{\rho_w c_p u_\tau} \tag{3.2}$$

with $\tau_w = \mu_w \frac{\partial \langle \tilde{u} \rangle}{\partial y}|_w$ and $q_w = -\lambda \frac{\partial \langle \tilde{T} \rangle}{\partial y}|_w$. These quantities are used to define non-dimensional parameters (Table 3.2),

$$Re_\tau = \frac{\rho_w u_\tau h}{\mu_w} \tag{3.3}$$

$$M_\tau = \frac{u_\tau}{\sqrt{\gamma R T_w}} \tag{3.4}$$

$$B_q = -\frac{T_\tau}{T_w} = \frac{-1}{PrRe} \frac{1}{\rho_w u_\tau} \frac{\partial \langle \tilde{T} \rangle}{\partial y}|_w \tag{3.5}$$

$$M_\tau^c = \frac{M_\tau}{\sqrt{-B_q}} = \frac{u_\tau}{\sqrt{\gamma R T_\tau}} \tag{3.6}$$

where $Re_\tau$, $M_\tau$ and $B_q$ are the friction Reynolds number, the friction Mach number and the non-dimensional heat flux, respectively. The $B_q$ and $M_\tau$ parameters allow to account for the Mach number influence in the expression of velocity law of the wall. The last coefficient represents the ratio between work done by wall friction and wall heat flux. It is weakly dependent on Mach and Reynolds numbers, about $M_\tau^c = 0.3 - 0.4$ for the classical external or body source term $\mathcal{W}_{body}$

| Case | M | Re | Flow state | $L_x$x$L_y$x$L_z$ | $N_x$x$N_y$x$N_z$ | $\Delta x^+$ | $\Delta y_w^+$ | $\Delta z^+$ |
|---|---|---|---|---|---|---|---|---|
| Kim et al. (1987) [43] | 0 | 3000 | Turbulent | $4\pi h$x$2h$x$2\pi h$ | 192x160x129 | 12 | 0.05 | 7 |
| Moser et al. (1999) [64] | 0 | 3000 | Turbulent | $4\pi h$x$2h$x$\frac{4}{3}\pi h$ | 128x128x129 | 17.7 | | 5.9 |
| Coleman et al. (1995) [14] | | | | $4\pi h$x$2h$x$\frac{4}{3}\pi h$ | 144x119x80 | | | |
| | 1.5 | 3000 | Turbulent | | | 19 | 0.2 | 12 |
| | 3 | 4880 | Turbulent | | | 24 | 0.4 | 24 |
| Lechner et al. (2001) [48] | 1.5 | 3000 | Turbulent | | | 19 | 0.99 | 12 |
| Morinishi et al. (2004) [61] | 1.5 | 3000 | Turbulent | $4\pi h$x$2h$x$\frac{4}{3}\pi h$ | 120x180x120 | 23 | 0.36 | 7.6 |
| Foysi et al. (2004) [61] | 0.3 | 2820 | Turbulent | $9.6h$x$2h$x$6h$ | 192x129x160 | 9.12 | 1.02 | 6.84 |
| | 1.5 | 3000 | Turbulent | $4\pi h$x$2h$x$\frac{4}{3}\pi h$ | 192x151x128 | 14.46 | 0.84 | 7.23 |
| | 2.5 | 5000 | Turbulent | $2\pi h$x$2h$x$\frac{2}{3}\pi h$ | 256x201x128 | 11.16 | 1.17 | 7.44 |
| | 3.0 | 6000 | Turbulent | $2\pi h$x$2h$x$\frac{2}{3}\pi h$ | 256x221x128 | 13.37 | 0.89 | 8.91 |
| 2D DNS [8] (T-configuration) | | | | $2\pi h$x$2h$x$\frac{4}{3}\pi h$ | 64x65x81 | | | |
| $(\mathcal{W}_{body})$ | 0.5-5.0 | 1200 | Laminar | | | - | - | - |
| $(\mathcal{W}_{body})$ | 0.5-5.0 | 1200 | Laminar | | | - | - | - |
| $(\mathcal{W}_{ext})$ | 0.5-5.0 | 1200 | Laminar | | | - | - | - |
| 3D LES [8] (T-configuration) | | | | $4\pi h$x$2h$x$\frac{4}{3}\pi h$ | 128x65x81 | | | |
| $(\mathcal{W}_{body})$ | 0.3 | 3000 | Turbulent | | | 20.1 | 0.10 | 10.7 |
| | 1.0 | 3000 | Turbulent | | | 19.8 | 0.10 | 10.5 |
| | 1.5 | 3000 | Turbulent | | | 21.5 | 0.11 | 11.3 |
| | 2.0 | 3000 | Turbulent | | | 23.7 | 0.12 | 12.4 |
| | 3.0 | 3000 | Transition | | | - | - | - |
| | 4.0 | 3000 | Transition | | | - | - | - |
| | 5.0 | 3000 | Laminar | | | - | - | - |
| | 1.0 | 4880 | Turbulent | | | 30.4 | 0.16 | 16.0 |
| | 3.0 | 4880 | Turbulent | | | 45.0 | 0.23 | 23.7 |
| | 5.0 | 4880 | Transition | | | - | - | - |
| $(\mathcal{W}_{ext})$ | 3.0 | 4880 | Turbulent | | | 45.3 | 0.23 | 23.8 |
| $(\mathcal{W}_{int})$ | 0.3 | 3000 | Turbulent | | | 17.7 | 0.10 | 9.4 |
| | 1.0 | 3000 | Transition | | | 25.5 | 0.14 | 13.6 |
| | 1.5 | 3000 | Transition | | | 35.0 | 0.20 | 18.7 |
| | 0.3 | 4880 | Turbulent | | | 29.2 | 0.15 | 15.3 |
| | 0.7 | 4880 | Turbulent | | | 36.2 | 0.19 | 19.0 |
| | 1.0 | 4880 | Turbulent | | | 43.2 | 0.22 | 22.7 |
| | 1.5 | 4880 | Turbulent | | | 56.7 | 0.29 | 29.8 |
| | 3.0 | 4880 | Laminar | | | 99.1 | 0.51 | 52.6 |
| Spatial/Distorted (S-configuration) | | | | | | | | |
| $(\mathcal{W}_{int})$ | | | | | | | | |
| 4 blocks | 0.7 | 4880 | Turbulent | 4x$4\pi h$x$2h$x$\frac{4}{3}\pi h$ | 4x128x65x81 | 36.2 | 0.19 | 19.0 |
| 7 blocks | 0.7 | 4880 | Turbulent | 7x$4\pi h$x$2h$x$\frac{4}{3}\pi h$ | 7x128x65x81 | 36.2 | 0.19 | 19.0 |

Table 3.1: **Mach and Reynolds numbers of the computed cases**

| Case | $M$ | $Re$ | $Re_\tau$ | $M_\tau$ | $-B_q$ | $M_\tau^c$ | $\langle\tilde{T}_c\rangle/T_w$ | Crocco-Busemann |
|---|---|---|---|---|---|---|---|---|
| LES ($\mathcal{W}_{body}$) | 0.3 | 3000 | 188 | 0.018 | 0.0022 | 0.39 | 1.016 | 1.018 |
| | 1.0 | 3000 | 203 | 0.058 | 0.023 | 0.38 | 1.18 | 1.20 |
| | 1.5 | 3000 | 219 | 0.079 | 0.05 | 0.36 | 1.40 | 1.45 |
| | 2.0 | 3000 | 241 | 0.097 | 0.08 | 0.35 | 1.72 | 1.80 |
| Coleman et al. (1995) [14] | 1.5 | 3000 | 222 | 0.082 | 0.049 | 0.37 | 1.38 | 1.45 |
| LES ($\mathcal{W}_{int}$) | 0.3 | 3000 | 193 | 0.018 | 0.0075 | 0.21 | 1.105 | 1.106 |
| | 1.0 | 3000 | 280 | 0.046 | 0.067 | 0.18 | 2.27 | 2.17 |
| | 1.5 | 3000 | 385 | 0.056 | 0.129 | 0.16 | 4.1 | 3.6 |
| LES ($\mathcal{W}_{body}$) | 1.0 | 4880 | 310 | 0.054 | 0.022 | 0.37 | 1.19 | 1.20 |
| | 3.0 | 4880 | 459 | 0.112 | 0.14 | 0.30 | 2.67 | 2.79 |
| Coleman et al. (1995) [14] | 3.0 | 4880 | 451 | 0.116 | 0.137 | 0.313 | 2.5 | 2.7 |
| LES ($\mathcal{W}_{ext}$) | 3.0 | 4880 | 462 | 0.110 | 0.138 | 0.29 | 2.73 | 2.79 |
| LES ($\mathcal{W}_{int}$) | 0.3 | 4880 | 297 | 0.017 | 0.0071 | 0.20 | 1.103 | 1.104 |
| | 0.7 | 4880 | 368 | 0.035 | 0.035 | 0.19 | 1.58 | 1.57 |
| | 1.0 | 4880 | 440 | 0.044 | 0.065 | 0.17 | 2.24 | 2.17 |
| | 1.5 | 4880 | 578 | 0.052 | 0.118 | 0.15 | 4.01 | 3.60 |

Table 3.2: **Wall parameters for the turbulent channel flow cases**

and about $M_\tau^c = 0.1 - 0.2$ for the internal source term $\mathcal{W}_{int}$, thus characteristic of which source term is applied.

## 3.2 Analytical solution for laminar compressible channel flow with constant transport coefficients and specific heats

The momentum equation (2.2) and the energy equation (2.3) written for a laminar compressible fully developed flow in the streamwise direction $x$ of a channel,

$$\begin{aligned} -\mu\frac{\partial^2 u}{\partial y^2} &= f &\quad (3.7)\\ -\lambda\frac{\partial^2 T}{\partial y^2} - -\mu\left(\frac{\partial u}{\partial y}\right)^2 - \mu u\frac{\partial^2 u}{\partial y^2} &= \gamma M^2 \mathcal{W} &\quad (3.8)\end{aligned}$$

are integrated twice from the wall. Constant molecular viscosity is assumed. Thus, analytical velocity and temperature profiles are obtained,

$$\begin{aligned} \frac{u(y)}{u_b} &= -\frac{3}{2}\,\frac{y^2-h^2}{h^2} &\quad (3.9)\\ \left.\frac{c_p\left(T(y)-T_w\right)}{u_b^2}\right|_{ext/body} &= -\frac{3}{4}\,Pr\,\frac{y^2-h^2}{h^2}\,\frac{y^2+h^2}{h^2} &\quad (3.10)\\ \left.\frac{c_p\left(T(y)-T_w\right)}{u_b^2}\right|_{int} &= \frac{3}{8}\,Pr\,\frac{y^2-h^2}{h^2}\,\frac{(3-2\gamma)y^2-(3+2\gamma)h^2}{(\gamma-1)h^2} &\quad (3.11)\end{aligned}$$

The three source terms result in a qualitatively similar behavior of the flow, although $\mathcal{W}_{int}$ yields a stronger heating effect on the channel centerline (Figures 3.1 and 3.2). For an increasing

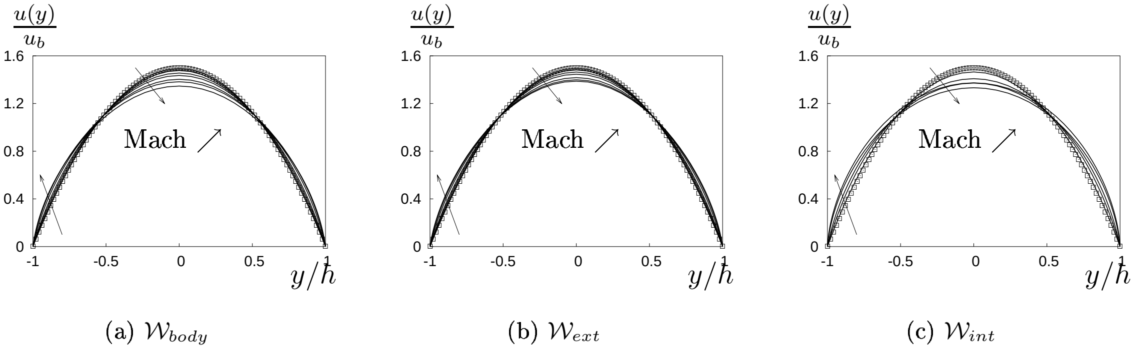

(a) $\mathcal{W}_{body}$ (b) $\mathcal{W}_{ext}$ (c) $\mathcal{W}_{int}$

Figure 3.1: **Laminar compressible channel flow at** $Re = 1200$ **for** $0.5 \leq M \leq 5$. **Velocity profile with** $\mathcal{W}_{body}$ **(a),** $\mathcal{W}_{ext}$**(b),** $\mathcal{W}_{int}$**(c). ——, simulation and □, analytical solution.**

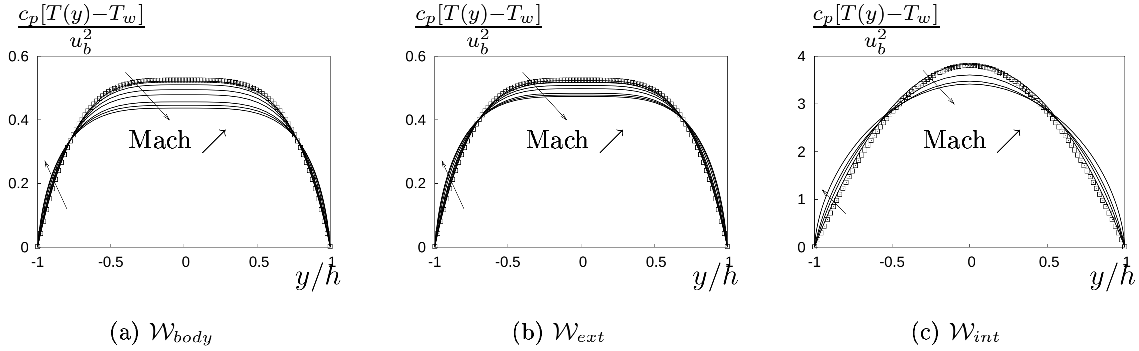

(a) $\mathcal{W}_{body}$ (b) $\mathcal{W}_{ext}$ (c) $\mathcal{W}_{int}$

Figure 3.2: **Laminar compressible channel flow at** $Re = 1200$ **for** $0.5 \leq M \leq 5$. **Temperature profile with** $\mathcal{W}_{body}$ **(a),** $\mathcal{W}_{ext}$ **(b),** $\mathcal{W}_{int}$ **(c). ——, simulation and □, analytical solution.**

Mach number, the computed profiles deviate more and more from the analytical solution, due to viscosity effects through temperatures changes.

Relations 3.9, 3.10 and 3.11 are used in the Section 4.1 to develop Crocco-Busemann type relations between velocity and temperature for turbulent isothermal-wall channel flows, for both body/external and internal forcing.

## 3.3 Validation of the LES method

In this section the $\mathcal{W}_{body}$ source term channel results are compared with those of Kim *et al.* [43] and of Coleman *et al.* [14]. The reference test cases are isothermal-wall direct numerical incompressible ($Re = 3000$ and $M = 0$) and compressible ($Re = 3000$ and $M = 1.5$) simulations, respectively (see also Tables 3.1 and 3.2). The LES test cases are those with a Reynolds number of $Re = 3000$ and Mach numbers of $M = 0.3$ (the closest case to incompressible flow) and of $M = 1.5$ (compressible case). The computational domains are identical for both DNS and LES compressible simulations.

Firstly, profiles of mean streamwise velocity and density are plotted in Figure 3.3 for the compressible simulations. The reference DNS results are plotted in open squares. It is noticed a good agreement between both LES and DNS simulations. The maximum mean velocity and minimum mean density occur at the centerline.

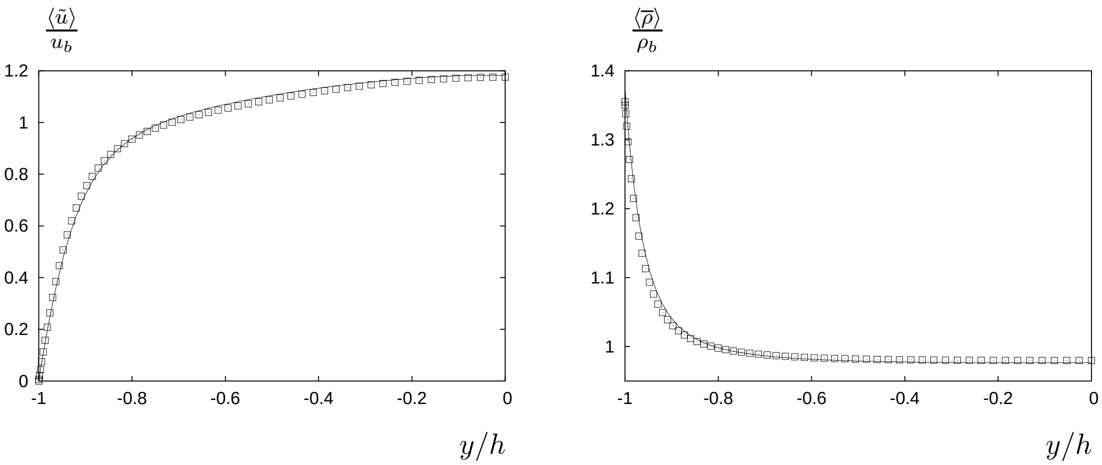

(a) Mean streamwise velocity

(b) Mean density

Figure 3.3: **Mean streamwise velocity (a) and mean density (b) profiles for** $Re = 3000$ **and** $M = 1.5$**: Coleman *et al.*** (1995) **( □ ) and** $\mathcal{W}_{body}$ **( —— ).**

Next, in Figures 3.4 and 3.5 are plotted the mean streamwise velocity profile and the rms velocity fluctuations normalized by the friction velocity for both incompressible and compressible cases, respectively. The reference DNS results are plotted in open squares.

The LES mean streamwise velocity is in a good agreement with the DNS incompressible reference. The logarithmic law constant is found slightly greater than the reference value of 5.5.

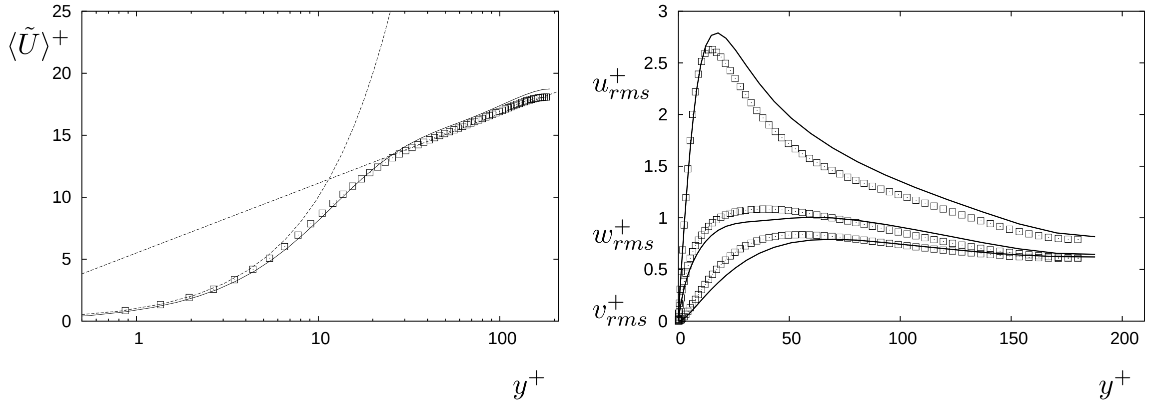

(a) Mean streamwise velocity (b) rms velocity fluctuations

Figure 3.4: **Mean streamwise velocity in wall units (a) and rms velocity fluctuations (b): Kim *et al.*** (1987) ( □ ) **and** $\mathcal{W}_{body}$ **simulation with** $Re = 3000$ **and** $M = 0.3$ ( —— ).

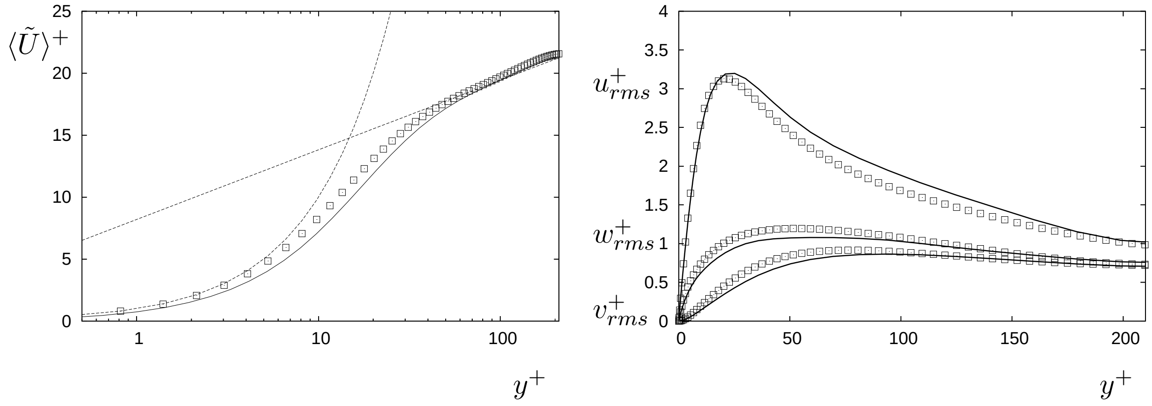

(a) Mean streamwise velocity (b) rms velocity fluctuations

Figure 3.5: **Mean streamwise velocity in wall units (a) and rms velocity fluctuations (b) for** $Re = 3000$ **and** $M = 1.5$**: Coleman *et al.*** (1995) ( □ ) **and** $\mathcal{W}_{body}$ ( —— ).

In the compressible case, there is also a good agreement between LES and DNS mean streamwise velocities apart from the buffer region.

RMS velocity fluctuations profiles are correct for both cases. The peak of $u^+_{rms}$ is well reproduced in amplitude, but it is slightly moved towards the center of the channel. The wall-normal and spanwise velocity fluctuations are underestimated in the near-wall region. In the core of the channel, these fluctuations are overestimated for the incompressible case, while they are correctly estimated for the compressible simulation. This might be due to the use of a sub-grid scale model in the case of the present simulation.

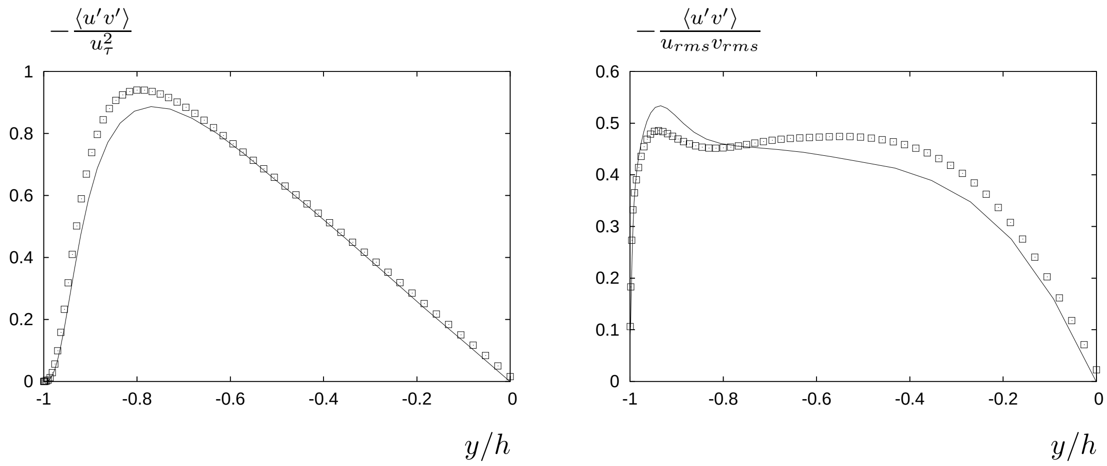

(a) Reynolds shear stress

(b) Reynolds stress correlation

Figure 3.6: **Profiles of (a) Reynolds shear stress and (b) Reynolds stress correlation for** $Re = 3000$ **and** $M = 1.5$**: Coleman *et al.*** (1995) **( □ ) and** $\mathcal{W}_{body}$ **( —— ).**

Profiles of the Reynolds shear stress normalized by the square of the friction velocity and of the Reynolds stress correlation are plotted in Figure 3.6 for the compressible case. The Reynolds shear stress has a lower maximum than the DNS result. Regarding the Reynolds-shear-stress correlation coefficient, there is a slight increase of the near-wall maximum and a slight decrease in the remaining part of the channel.

# Part II

# SIMULATION RESULTS

# CHAPTER 4

# Fully developed compressible channel flow

In this chapter data produced by LES simulations of fully developed turbulent compressible flow are examined. This data will then be used as a reference for the flows discussed in subsequent chapters.

A parametric study performed based on Mach number, Reynolds number and the two source terms described in Section 2.3 is presented here. Compressibility and low Reynolds number effects are discussed, classical Reynolds and Favre averaging procedures are compared, and the turbulence structure of the flow is discussed in terms of anisotropy invariants and instantaneous visualization. Morkovin's hypothesis is assessed and the modified Strong Reynolds Analogy formulation of *Huang et al.* [34] is analysed and assessed.

The chapter ends with a brief summary.

## 4.1 Mean properties

The isothermal walls allow the heat generated by dissipation to be transferred out of the channel. Thus, the walls are colder than the bulk of the flow and the maximum mean temperature and minimum mean density - and therefore the maximum mean kinematic viscosity- occur at the centerline. Furthermore, the maximum gradients of mean density and temperature are located at $y = \pm h$, which is a very important attribute of the isothermal-wall flow. This is illustrated in Figures 4.1 and 4.2 for both source terms, $\mathcal{W}_{ext}$ / $\mathcal{W}_{body}$ on the left hand side and $\mathcal{W}_{int}$ on the right hand side. The arrows show the quantities variation when the Mach number increases. It is noticed that the temperature at the centreline is up to 3-times larger for simulations with the $\mathcal{W}_{int}$ source term than for simulations with classical source terms (see also Table 3.2). For example, a simulation at $Re = 3,000$ and $M = 1.5$ has the temperature at the centreline of 1.4 when using the $\mathcal{W}_{body}$ souce term, while when using the $\mathcal{W}_{int}$ source term the temperature reaches 4.1.

Consequently, the global Reynolds number $Re$ and the global Mach number $M$ are not the best quantities to represent the flow property and parameters including local viscous effects

(Figure 4.2) and local speed of sound effects may be considered, respectively

$$Re_l(y) = \frac{\langle \bar{\rho}(\tilde{T}) \rangle \, \langle \tilde{u} \rangle \, h}{\langle \tilde{\mu}(\tilde{T}) \rangle} \tag{4.1}$$

$$M_l(y) = \frac{\langle \tilde{u} \rangle}{\sqrt{\gamma R \langle \tilde{T} \rangle}} \tag{4.2}$$

The local Mach number gives us an indication on sub- and supersonic regions in the channel flow. As shown in Figure 4.3, the near-wall regions in the flow are always subsonic. For simulations with external or body source terms, starting with $M = 1$, the local Mach number $M_l$ is lower than the Mach number of the simulation. This trend is even enhanced for simulations with internal source term. It can be explained based on differences in temperature for simulations at the same Mach and Reynolds numbers, but using a different forcing.

A Crocco-Busemann type relation between velocity and temperature exists for a turbulent adiabatic boundary layer [75, 16, 9] or for a turbulent isothermal-wall boundary layer [12], respectively

$$\frac{\langle \tilde{T} \rangle - T_w}{T_w} = -M_e^2 \, (\gamma - 1) \frac{1}{2} \, \frac{\langle \tilde{u} \rangle^2}{u_e^2} \tag{4.3}$$

$$\frac{\langle \tilde{T} \rangle - T_w}{T_w} = \frac{T_e - T_w}{T_w} \, \frac{\langle \tilde{u} \rangle}{u_e} + M_e^2 \, \frac{\gamma - 1}{2} \left( \frac{\langle \tilde{u} \rangle}{u_e} - \frac{\langle \tilde{u} \rangle^2}{u_e^2} \right) \tag{4.4}$$

with $M_e = u_e / \sqrt{\gamma R T_w}$ the Mach number based on the external flow velocity (subscript $e$ referring to the external flow). These Crocco-Busemann relations differ in the case of a turbulent isothermal-wall channel flow because of symmetry conditions. They may be derived from equations (3.9), (3.10) and (3.11), written in terms of statistics for a turbulent flow, [1]

$$\frac{\langle \tilde{u} \rangle (y)}{u_b} = -\frac{3}{2} \frac{y^2 - h^2}{h^2} \tag{4.5}$$

$$\left. \frac{\langle \tilde{T} \rangle - T_w}{T_w} \right|_{ext/body} = (\gamma - 1) \; Pr \; M_b^2 \; \left( \frac{\langle \tilde{u} \rangle}{u_b} - \frac{1}{3} \frac{\langle \tilde{u} \rangle^2}{u_b^2} \right) \tag{4.6}$$

$$\left. \frac{\langle \tilde{T} \rangle - T_w}{T_w} \right|_{int} = Pr \; M_b^2 \; \left( \gamma \, \frac{\langle \tilde{u} \rangle}{u_b} + \frac{(3 - 2\gamma)}{6} \frac{\langle \tilde{u} \rangle^2}{u_b^2} \right) \tag{4.7}$$

with $M_b = u_b / \sqrt{\gamma R T_w}$ the Mach number based on the bulk velocity in the channel.

A good agreement between computed temperature values and estimated temperature values (Eqs. 4.6 and 4.7) is found, especially for the $\mathcal{W}_{int}$ source term (see Table 3.2 and Fig. 4.1). Therefore, although these relations have been derived for laminar flows and assuming constant viscosity, they will be used to develop a Reynolds analogy for the turbulent compressible channel flow (see Section 4.7.2).

---

[1] A useful result to derive these relations is:

$$\frac{y^4 - h^4}{h^4} = \left( \frac{y^2 - h^2}{h^2} \right)^2 + 2 \, \frac{y^2 - h^2}{h^2} = -\frac{4}{3} \frac{\langle \tilde{u} \rangle (y)}{u_b} \left( 1 - \frac{1}{3} \frac{\langle \tilde{u} \rangle (y)}{u_b} \right)$$

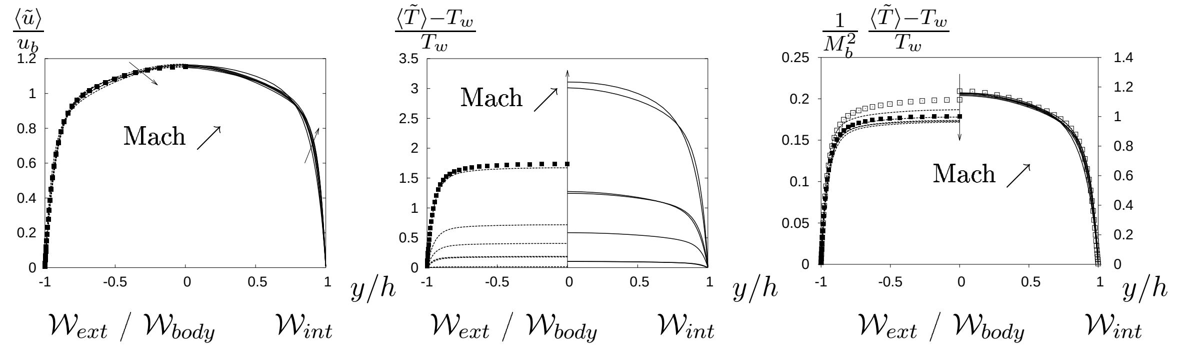

(a) Velocity

(b) Temperature

(c) Temperature

Figure 4.1: **Mean velocity (a) and temperature (b,c) profiles for both source terms $\mathcal{W}_{body}$ ( - - - ), $\mathcal{W}_{ext}$ ( ■ ) and $\mathcal{W}_{int}$ ( —— ). Crocco-Busemann type relations (equations 4.6 & 4.7) are also plotted ( □ ). Mach number effect $0.3 \leq M \leq 3$. The arrows show quantities variation when Mach number increases.**

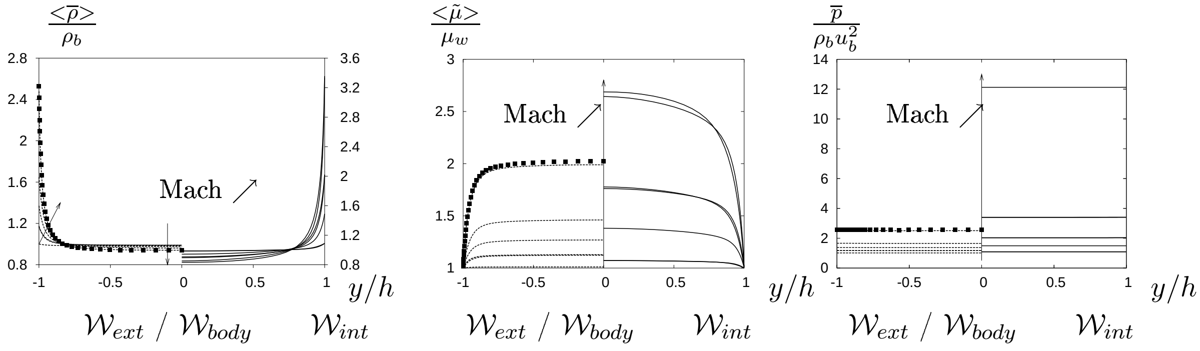

(a) Density

(b) Dynamic viscosity

(c) Mean pressure

Figure 4.2: **Mean density (a), mean dynamic viscosity (b) and mean pressure (c) profiles, for $\mathcal{W}_{body}$ ( - - - ), $\mathcal{W}_{ext}$ ( ■ ) and $\mathcal{W}_{int}$ ( —— ). Mach number effect $0.3 \leq M \leq 5$. The arrows show quantities variation when Mach number increases.**

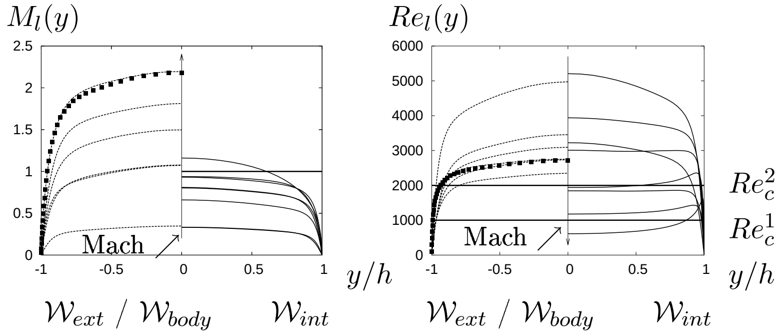

(a) $M_l(y) = \frac{\langle\tilde{u}\rangle}{\sqrt{\gamma R \langle\tilde{T}\rangle}}$ (b) $Re_l(y) = \frac{\langle\overline{\rho}(\tilde{T})\rangle \; \langle\tilde{u}\rangle \; h}{\langle\overline{\mu}(\tilde{T})\rangle}$

Figure 4.3: **Local Mach number (a) and local Reynolds number (b) profiles, for** $\mathcal{W}_{body}$ **( - - - ),** $\mathcal{W}_{ext}$ **( ■ ) and** $\mathcal{W}_{int}$ **( —— ). Mach number effect** $0.3 \leq M \leq 5$**. The arrows show quantities variation when Mach number increases.**

## 4.2 Compressibility and low Reynolds number effects

In general, the effects of compressibility on wall-bounded turbulence can be classified as one of two types: those associated with variations of the mean properties (such as density and viscosity), and those due to fluctuations of thermodynamic quantities. It is often assumed that only the mean effects are significant for non-hypersonic wall-bounded flows (i.e., free-stream Mach number less than about 5) [6, 83].

The first direct effect of compressibility is a heating effect which yields an increase of the temperature and thus of the viscosity in the center of the channel (Figure 4.2). As for incompressible channel flow, pressure is uniform in the wall normal direction, which yields, because of the perfect gas law, a mean density decrease in the center of the channel, and a strong wall density increase with Mach number.

A strong relaminarisation effect is obtained for increasing Mach number at constant wall temperature $T_w$ and constant bulk mass flux $(\rho u)_b$ whichever source term is considered (Figure 4.3). The critical Reynolds numbers $Re_c^1 = 1000$ and $Re_c^2 = 2000$ refer to the lower and the upper limit of the transition regime from laminar to fully turbulent in an incompressible pipe flow (Reynolds experiments). For the flow case ($\mathcal{W}_{ext}$: $M = 5$, $Re = 3000$) the local Reynolds number is always below this limit $Re_l \leq Re_c^1$ and the flow might fully relaminarize. For the flow case ($\mathcal{W}_{int}$: $M = 3$, $Re = 4880$) the local Reynolds number is nearly below this limit, but for a tiny zone close to the wall. The cases ($\mathcal{W}_{ext}$: $M = 3$, $Re = 3000$), ($\mathcal{W}_{ext}$: $M = 4$, $Re = 3000$), ($\mathcal{W}_{ext}$: $M = 5$, $Re = 4880$), ($\mathcal{W}_{int}$: $M = 1$, $Re = 3000$) and ($\mathcal{W}_{int}$: $M = 1.5$, $Re = 3000$) are transitional cases characterized by a large zone in the channel where $Re_c^1 \leq Re_l(y) \leq Re_c^2$.

The friction Reynolds number $Re_\tau$ referred to on Table 3.2 increases while the flow gets laminar. The reason is that $Re_\tau$ is built of quantities determined at the cold wall only ($T_w$, $u_\tau$) while there exist strong temperature gradients from the wall to the center of the channel which yield viscous effects in the boundary layer. The commonly used incompressible definition of the friction Reynolds number is obsolescent for compressible channel flow and more generally non-adiabatic boundary layers [6, 14, 34].

## 4.3 Anisotropy invariant map (AIM)

The anisotropy invariant map is the invariant representation of Reynolds stresses [56, 55, 69]. This is a useful postprocessing tool which gives an indication of the state of the turbulence in different regions within a flow. Also, AIM allows to verify whether a simulated or modelled flow contains unphysical regions.

The analysis of Lumley [55] gives information about anisotropy of the large-scales of the motion since it depends on the Reynolds stress tensor. Classical theories of turbulence assume the isotropy of the smallest scales. DNSs of Yeung and Brasseur [92] have shown that high levels of anisotropy are induced at the small-scales of motion when anisotropic forcing of the largest scales is applied. Hence, in order to provide information about the anisotropy of small-scale motion, Lumley's invariant analysis has been applied to the tensors for the vorticity and dissipation rate of kinetic energy [3].

The non-dimensional Reynolds stress anisotropy tensor is defined based on the Reynolds averaged quantities as

$$\alpha_{ij} = \frac{\langle \tilde{u}_i \tilde{u}_j \rangle - \langle \tilde{u}_i \rangle \langle \tilde{u}_j \rangle}{2k} - \frac{1}{3}\delta_{ij} = \frac{\langle u'_i u'_j \rangle}{2k} - \frac{1}{3}\delta_{ij} \tag{4.8}$$

and the second and the third invariants of the anisotropy tensor can be defined as, respectively

$$I_2 = -\frac{\alpha_{ij}\alpha_{ji}}{2} \tag{4.9}$$

$$I_3 = \frac{\alpha_{ij}\alpha_{jk}\alpha_{ki}}{3} \tag{4.10}$$

where $k$ is the turbulence kinetic energy $k = \frac{\langle \tilde{u}_k \tilde{u}_k \rangle - \langle \tilde{u}_k \rangle \langle \tilde{u}_k \rangle}{2}$. A similar anisotropy tensor can be defined based on the density-weighted quantities and it will be discussed in Section 4.4, Figures 4.11.

In the case of isotropic turbulence, the only non-zero stresses are $\langle u'_1 u'_1 \rangle = \langle u'_2 u'_2 \rangle = \langle u'_3 u'_3 \rangle = \frac{2}{3}k$ and $I_2 = I_3 = 0$.

In the case of axisymmetric turbulence, the invariants reduce to the following axisymmetric relation

$$I_3 = +2\left(\frac{-I_2}{3}\right)^{3/2} \quad (axisymmetric\ \ expansion) \tag{4.11}$$

$$I_3 = -2\left(\frac{-I_2}{3}\right)^{3/2} \quad (axisymmetric\ \ contraction) \tag{4.12}$$

The two different modes of axisymmetry [49] are: *axisymmetric contraction*, caused by straining in one direction and contracting in the other two, and *axisymmetric expansion*, caused by straining the flow equally in two orthogonal directions and contracting it in the third. Lee and Reynolds [49] suggested that the parameter $A$, defined as

$$A = \frac{I_3}{2(-I_2/3)^{3/2}} \tag{4.13}$$

might be used as a measure of axisymmetry: values $A = -1$ and $A = 1$ correspond to 'rod-like' and 'disk-like' turbulence, respectively.

| Case | $M$ | $Re$ | $-I_2$ | $I_3$ | $A$ |
|---|---|---|---|---|---|
| LES ($\mathcal{W}_{body}$) | 0.3 | 3000 | 0.208 | 0.032 | 0.876 |
| | 1.0 | 3000 | 0.216 | 0.035 | 0.906 |
| | 1.5 | 3000 | 0.239 | 0.043 | 0.956 |
| | 2.0 | 3000 | 0.252 | 0.047 | 0.965 |
| LES ($\mathcal{W}_{body}$) | 1.0 | 4880 | 0.234 | 0.041 | 0.941 |
| | 3.0 | 4880 | 0.276 | 0.055 | 0.985 |
| LES ($\mathcal{W}_{ext}$) | 3.0 | 4880 | 0.273 | 0.054 | 0.984 |
| LES ($\mathcal{W}_{int}$) | 0.3 | 3000 | 0.203 | 0.031 | 0.881 |
| | 1.0 | 3000 | 0.257 | 0.049 | 0.977 |
| | 1.5 | 3000 | 0.281 | 0.057 | 0.994 |
| LES ($\mathcal{W}_{int}$) | 0.3 | 4880 | 0.229 | 0.039 | 0.925 |
| | 0.7 | 4880 | 0.242 | 0.044 | 0.960 |
| | 1.0 | 4880 | 0.259 | 0.049 | 0.966 |
| | 1.5 | 4880 | 0.273 | 0.054 | 0.984 |

Table 4.1: **Invariants at the first-grid point**

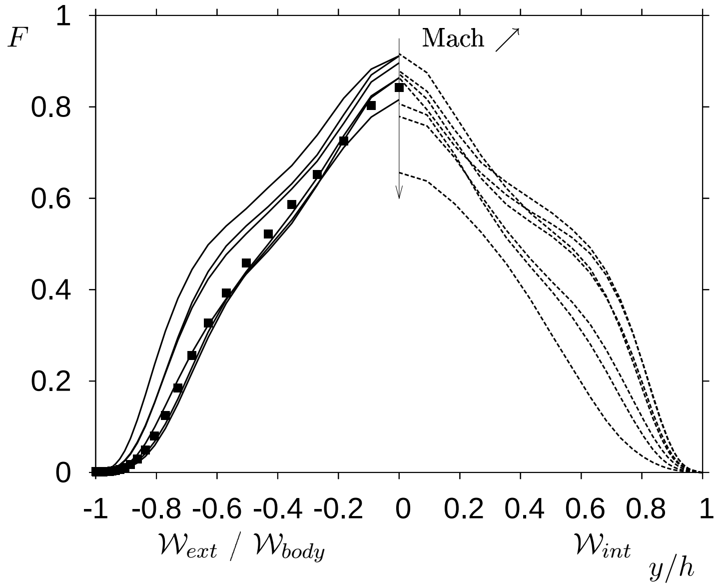

Figure 4.4: **Anisotropy function in fully developed channel flow:** $\mathcal{W}_{body}$ **( —— ),** $\mathcal{W}_{ext}$ **( ■ ) and** $\mathcal{W}_{int}$ **( - - - ). Mach number effect** $0.3 \leq M \leq 3$**. The arrows show quantities variation when Mach number increases.**

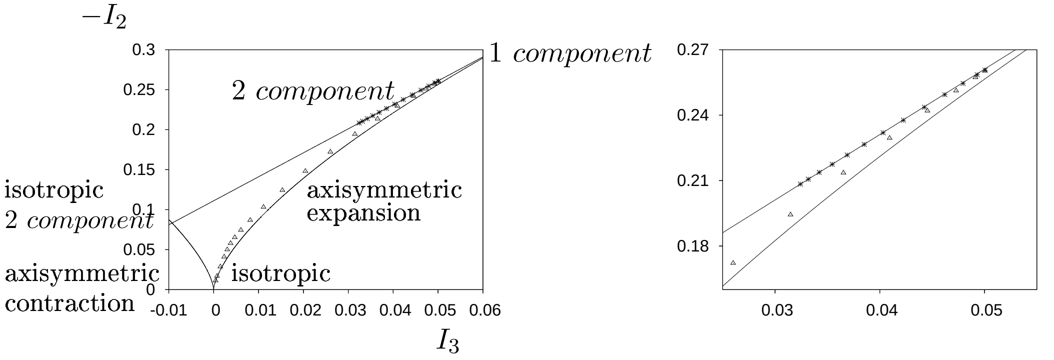

(a) $M = 0.3$

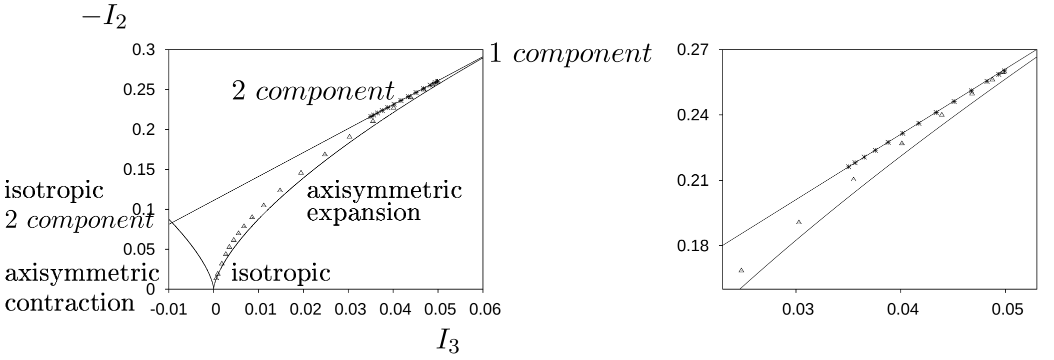

(b) $M = 1.0$

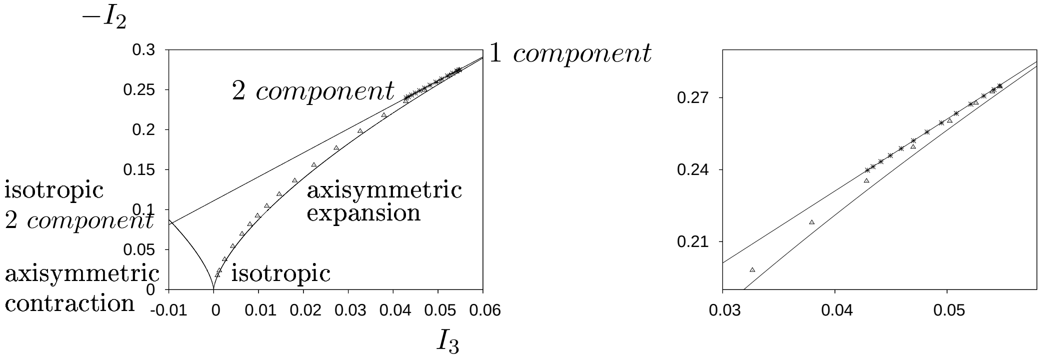

(c) $M = 1.5$

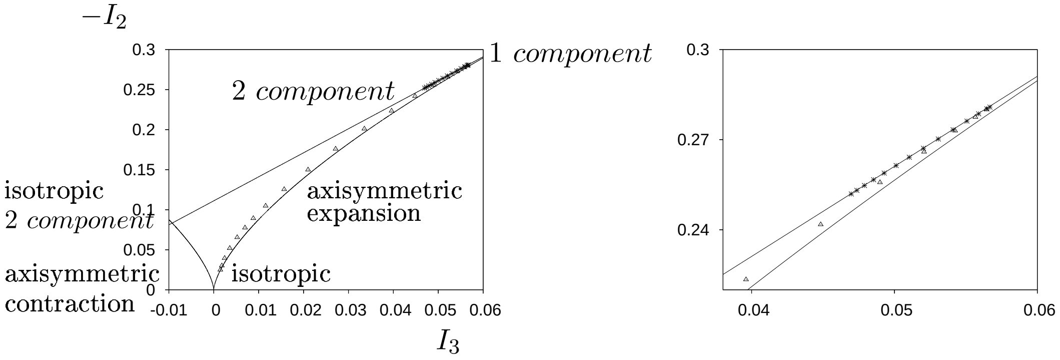

(d) $M = 2.0$

Figure 4.5: **Anisotropy invariant map for channel flows with $\mathcal{W}_{body}$, $Re = 3000$.**

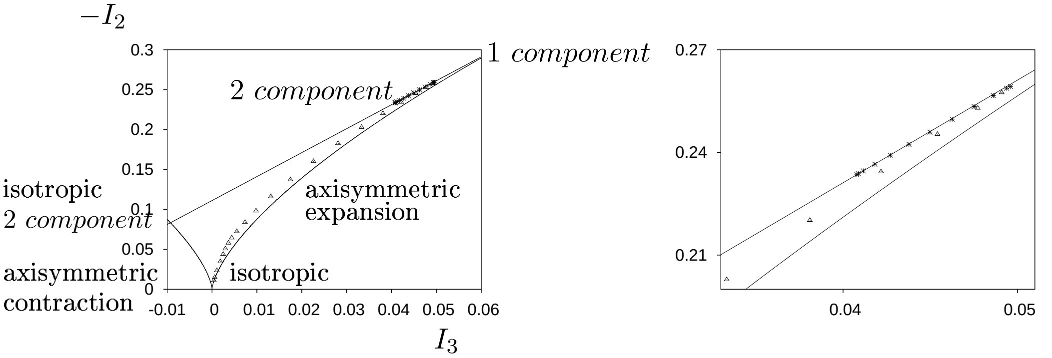

(a) $M = 1.0$

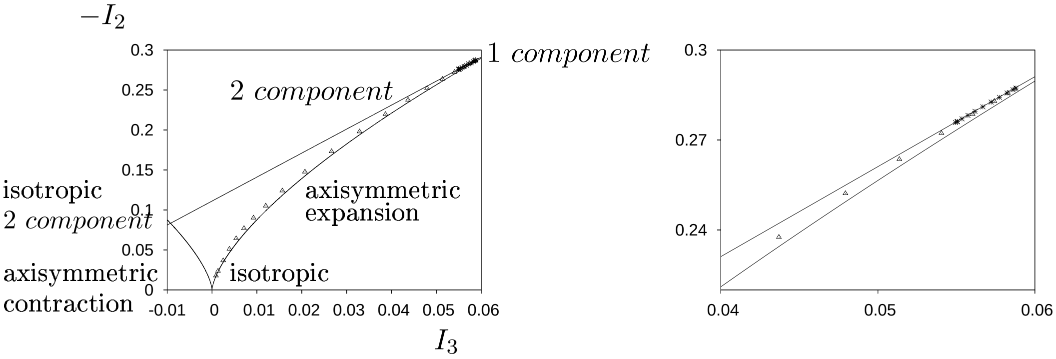

(b) $M = 3.0$

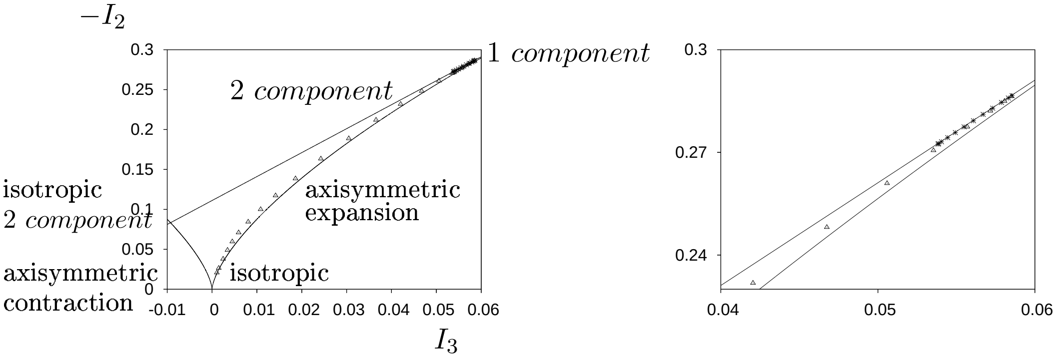

(c) $\mathcal{W}_{ext}$ $M = 3.0$

Figure 4.6: **Anisotropy invariant map for channel flows with $\mathcal{W}_{body}$, $Re = 4880$.**

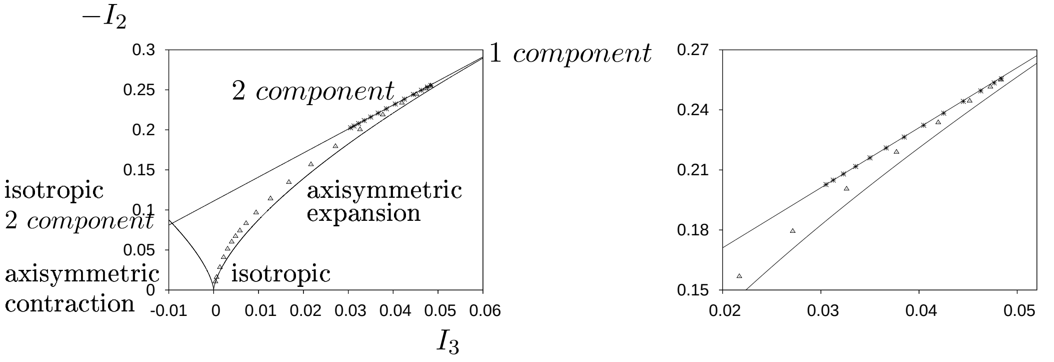

(a) $M = 0.3$

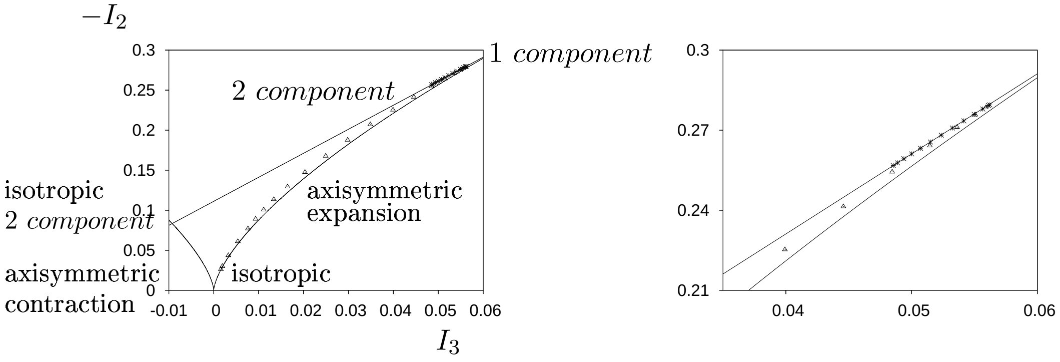

(b) $M = 1.0$

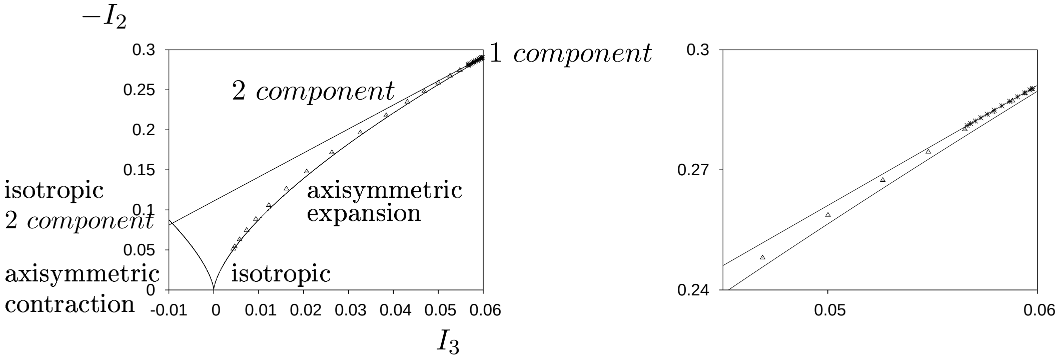

(c) $M = 1.5$

Figure 4.7: **Anisotropy invariant map for channel flows with $\mathcal{W}_{int}$, $Re = 3000$.**

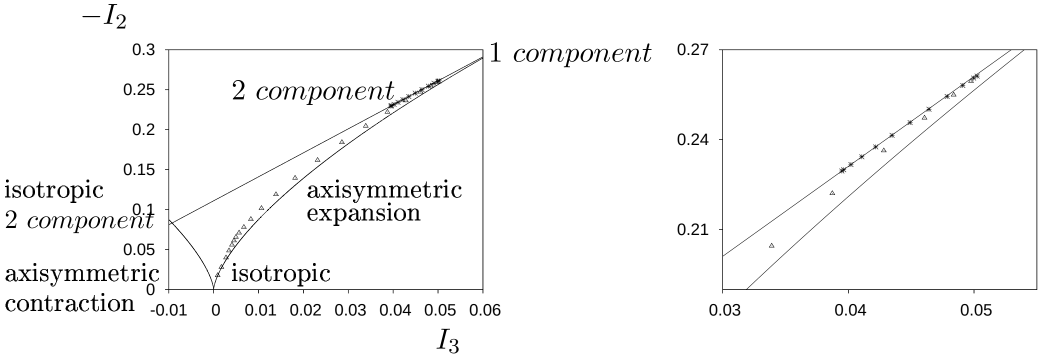

(a) $M = 0.3$

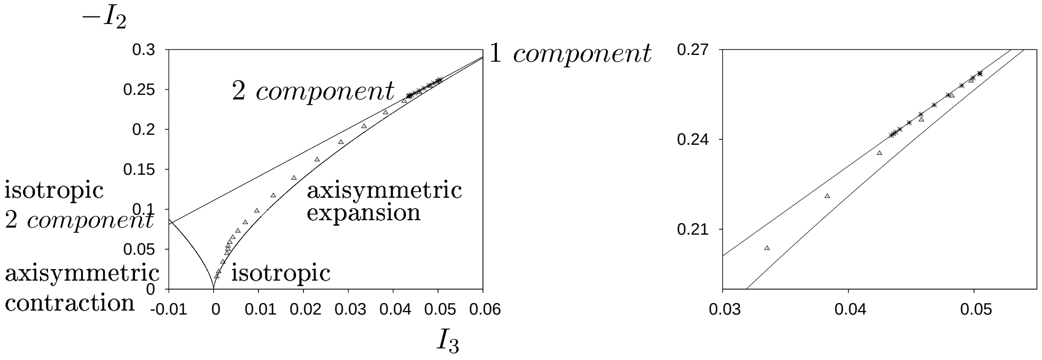

(b) $M = 0.7$

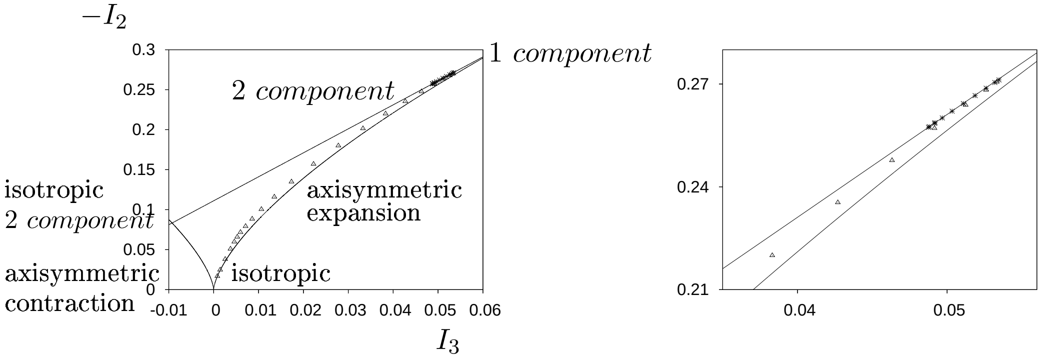

(c) $M = 1.0$

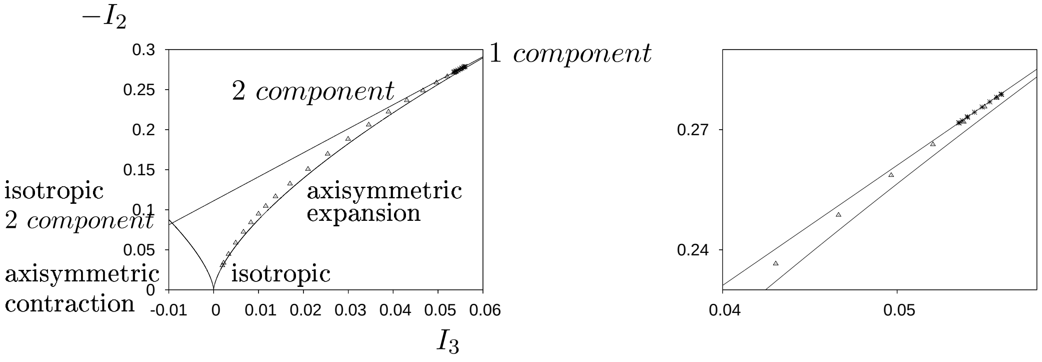

(d) $M = 1.5$

Figure 4.8: **Anisotropy invariant map for channel flows with $\mathcal{W}_{int}$, $Re = 4880$.**

Identically two-component turbulence can be defined in terms of the invariants by

$$1/9 + I_2 + 3I_3 = 0 \tag{4.14}$$

Lumley suggested that the parameter $F = 1 + 9I_2 + 27I_3$ might be used as a measure of the departure from isotropic ($F \equiv 1$) and two-component turbulence ($F \equiv 0$). This parameter is plotted in Figure 4.4 for all the fully developed channel simulations considered in the present study.

Values of the $A$-parameter at the first-grid point for the turbulent channel simulations are reported in Table 4.1. Turbulent motion close to a wall is more axisymmetric for simulations with the $\mathcal{W}_{int}$ source term than those with the $\mathcal{W}_{ext}$ or $\mathcal{W}_{body}$ source term. The same trend is obtained while the Mach number increases.

Plotted together the invariants form the anisotropy invariant map (AIM) which encloses all the possible physical solutions for turbulence. This is shown in Figs. (4.5, 4.6, 4.7 and 4.8). In the near-wall region the flow is two dimensionnal ($F \equiv 0$ as shown in Figure 4.4) as the wall supresses the wall normal velocity. The streamwise Reynolds stress grows much faster than the other stresses and, at about $y/h \approx \pm 0.96$ for all the simulations, independent of the source term type or the Mach number or the Reynolds number, the flow tends towards the one-component turbulence point. It should be noted that this region, from the wall to $y/h \approx \pm 0.96$, is less extended while the Mach number is increased.

Further away from the wall the turbulence stays close to the axisymmetric expansion limit. In the centre of the channel, the turbulence gets closer to the isotropic limit, but is still axisymmetric [91]. The anisotropy function values decrease with Mach number increasing, Figure 4.4.

The sudden deflection found for the simulation ($\mathcal{W}_{int}$, $Re = 4880$, $M = 0.7$) is explained by Krogstad & Torbergsen [47] as related to the separation of the central core region from the near-wall region.

## 4.4 Reynolds vs Favre averaging

In this section conventional Reynolds or ensemble averaging (Equation 2.79) and mass-weighted averaging (Equation 2.84) (commonly referred to as "Favre" averaging, although Reynolds (1895) was the first to propose it) are compared. They were performed on time samples extracted from the following simulations: ($\mathcal{W}_{ext} : M = 3, Re = 4,880$), ($\mathcal{W}_{body} : M = 3, Re = 4,880$) and ($\mathcal{W}_{int} : M = 1, Re = 4,880$).

An evaluation of the scatter between these two statistical procedures may be obtained from the quantity $\langle f \rangle - \{f\}$ (Section 2.8). It is reported to be about 1.5% for the velocity field, for an adiabatic boundary layer at Mach 3 [80]. Huang *et al.* evaluated this quantity to be 3% for the velocity field, too, but for a channel flow at Mach 3 [34].

As can be seen from the Fig. 4.9, the difference between Reynolds- and Favre-averaged quantities is mainly observed in the near-wall region ($y/h < 0.3$). It reaches up to about 3% of the velocity field and 1.5% of the temperature field for the present isothermal-wall channel flow with both source terms up to Mach 3.

The contribution of the Reynolds stress and the turbulent heat flux are plotted on Figures (4.10a), (4.10b) and (4.10c). Favre averaging fits the classical averaging with a maximum of 5% scatter and this is confined to the sublayer region ($y/h < 0.1$).

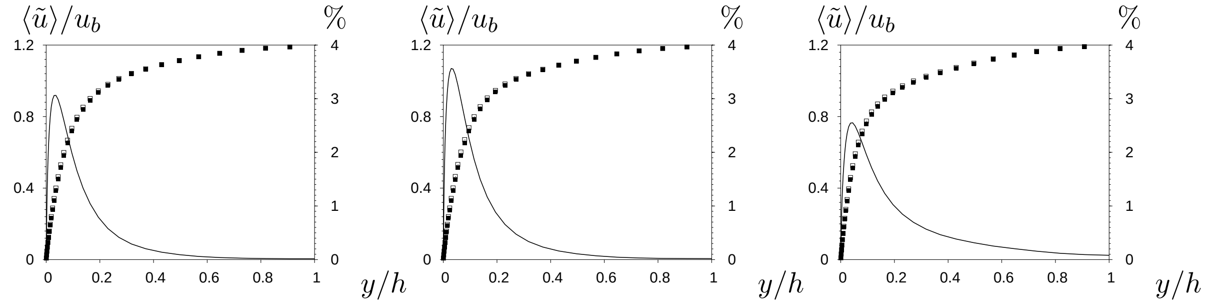

(a) $\mathcal{W}_{body}$ at $Re = 4880$, $M = 3$ (b) $\mathcal{W}_{ext}$ at $Re = 4880$, $M = 3$ (c) $\mathcal{W}_{int}$ at $Re = 4880$, $M = 1$

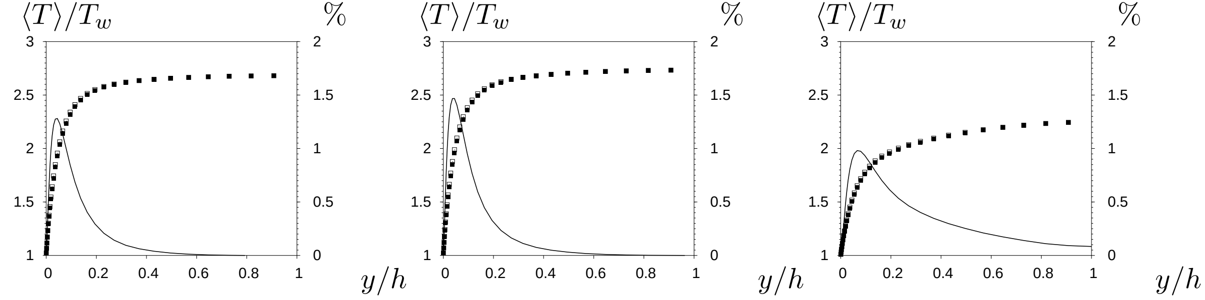

(d) $\mathcal{W}_{body}$ at $Re = 4880$, $M = 3$ (e) $\mathcal{W}_{ext}$ at $Re = 4880$, $M = 3$ (f) $\mathcal{W}_{int}$ at $Re = 4880$, $M = 1$

Figure 4.9: **Mean streamwise velocity (a,b,c) and mean temperature (d,e,f) for each source term, using classical statistics procedure ( □ ) and Favre statistics procedure ( ■ ). The scatter between the two statistical values $\frac{\langle f\rangle - \{f\}}{\langle f\rangle}$ is expressed in % on the rhs ( —— ).**

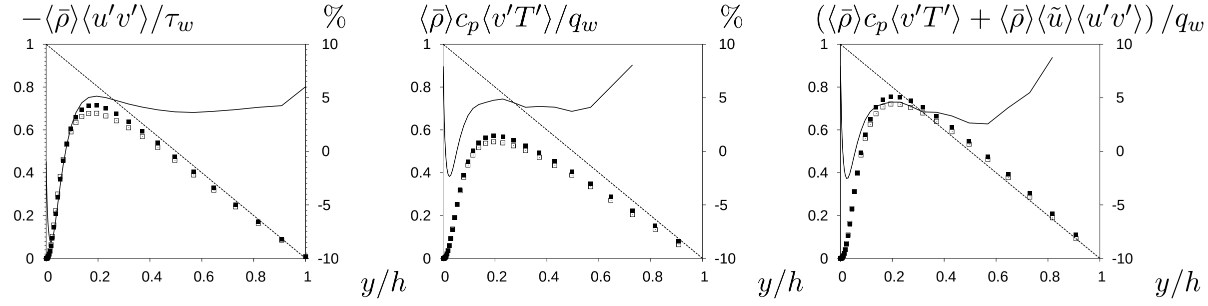

(a) velocity cross correlation (b) temperature-velocity correlation (c) total temperature-velocity correlation

Figure 4.10: **Reynolds stress (a), Turbulent heat fluxes (b,c), using standard and Favre averaging for $\mathcal{W}_{int}$ at $Re = 4880$, $M = 1$, using classical statistics procedure ( □ ) and Favre statistics procedure ( ■ ). The scatter between the two statistical values is expressed in % on the rhs ( —— ).**

The anisotropy invariant map computed with the two averaging procedures are similar, as shown in Figure 4.11.

In conclusion, differences between Reynolds and Favre averaging are small and are mainly observed in the near-wall region.

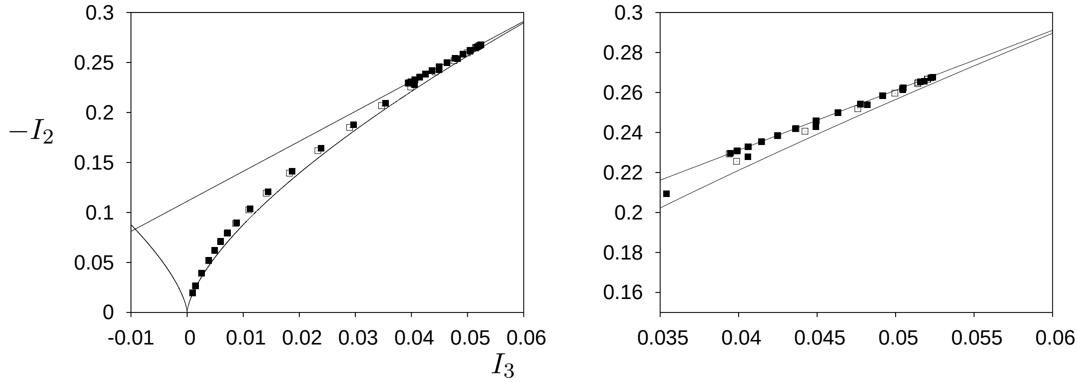

Figure 4.11: **Anisotropy invariant map for $\mathcal{W}_{int}$ at $Re = 4,880$ & $M = 1$, using classical statistics procedure ( □ ) and Favre ( ■ ) statistics procedure.**

## 4.5 Coherent structures

The term 'structure' is used to describe coherent organized motions occuring in the flow.

Robinson [39] defined a coherent motion, or structure, as

*a three-dimensional region of the flow over which at least one fundamental variable (velocity component, density, temperature, etc.) exhibits significant correlation with itself or with another flow variable over a range of space and/or time that is significantly larger than the smallest local scales of the flow.*

Lesieur [52] summarized the properties of a coherent structure, as following

- a high enough vorticity to make a local rollup of the surrounding fluid possible,
- the preservation of its shape approximately during a time long enough in front of the local turnover time, and
- unpredictability.

Several vortex-identification methods exist, among them,

- the low-pressure criterion: the cores of the coherent structures should be low dynamic pressure regions,
- the positive Q-criterion proposed by Hunt & al. [35]

$$Q = \frac{1}{2}(\overline{\Omega}_{ij}\overline{\Omega}_{ij} - \overline{S}_{ij}\overline{S}_{ij}) \tag{4.15}$$

with $S_{ij}$ and $\Omega_{ij}$ the symmetric and antisymmetric parts of the velocity gradient tensor, respectively

$$\overline{S}_{ij} = \frac{1}{2}\left(\frac{\partial \overline{u}_i}{\partial x_j} + \frac{\partial \overline{u}_j}{\partial x_i}\right) \tag{4.16}$$

$$\overline{\Omega}_{ij} = \frac{1}{2}\left(\frac{\partial \overline{u}_i}{\partial x_j} - \frac{\partial \overline{u}_j}{\partial x_i}\right) \tag{4.17}$$

- the negative $\lambda_2$-criterion introduced by Jeong & Hussain [36, 37]. A coherent vortex is associated to a local minimum of pressure which corresponds to two negative eigenvalues of $\overline{S}^2 + \overline{\Omega}^2 = -\frac{1}{\bar{\rho}}\frac{\partial^2}{\partial x_i \partial x_j}\bar{p}$. Since there are three real eigenvalues classified as $\lambda_1 \geq \lambda_2 \geq \lambda_3$, its second eigenvalue $\lambda_2$ is negative.

Flow visualizations based on positive isovalues of the Q-criterion (Figures 4.12 to 4.15, right) show less and less small-scale turbulent structures for inceasing Mach number and confirm the relaminarisation observation (section 4.2). For the same Reynolds number, simulations with $\mathcal{W}_{int}$ seem to get relaminarisation faster with increasing Mach number.

The wall-normal gradients of mean density and temperature cause an enhanced streamwise coherence of the near-wall streaks for an increasing Mach number [14]. The width and shape of the streaks close to the wall are also modified (Figures 4.12 to 4.15, left). This is not a compressibility effect but a viscous effect since the dynamic viscosity $\tilde{\mu}(\tilde{T}) \propto \tilde{T}^{0.7}$ increases with Mach number [14].

## 4.6 The Morkovin's hypothesis

The compressible channel flow is a special wall-bounded flow with strong mean temperature and density gradients at the wall, which is thus not covered by the Morkovin's hypothesis [6] and has to be discussed.

Kovasznay [46] has shown that the vorticity, acoustic and entropy modes are the solutions for the perturbation fields superimposed on a uniform steady flow of a compressible, viscous and heat-conductive gas. When the fields are weak, these modes obey separate linear differential equations, while, when the fields are stronger, they have moderate interactions.

The velocity, pressure and temperature fields can be easily split into the three modes if the spatial scale of the disturbances is not too small. Thus, the solenoidal part of the velocity field constitutes the vorticity mode, while the irrotational field belongs to the acoustic mode. The pressure fluctuations contribute to the sound waves. Isentropic fluctuations of the density and temperature fields belong to the acoustic mode, too, while the nonisentropic part constitutes the entropy mode.

Compressible fluctuations may be equivalently categorized into acoustic, total temperature and vorticity disturbances. The total temperature [17, 60] is defined as

$$\langle\tilde{T}_i\rangle = \langle\tilde{T}\rangle + \frac{Pr_m}{2c_p}\langle\tilde{u}_k\rangle\langle\tilde{u}_k\rangle \tag{4.18}$$

The mixed Prandtl number $Pr_m$ is defined as [59, 60]

$$Pr_m = \frac{(\mu + \mu_t)c_p}{\lambda + \lambda_t} \tag{4.19}$$

where $\mu_t$ and $\lambda_t$ are the turbulent viscosity (Eq. 6.3) and turbulent conductivity (Eq. 6.4), respectively.

Morkovin's hypothesis [62] refers to the structure of the turbulence in compressible boundary layers. It postulates that the essential dynamics of compressible boundary layers closely follow the incompressible pattern, as long as the entropy and acoustic modes are negligible or small [46,

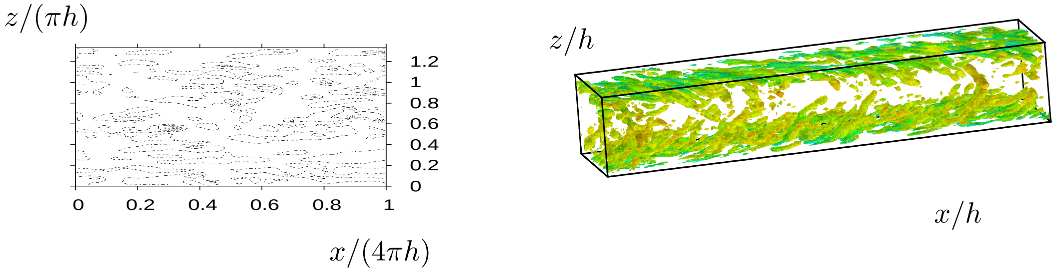

(a) $\mathcal{W}_{body}$, $M = 0.3$, $Re = 3000$

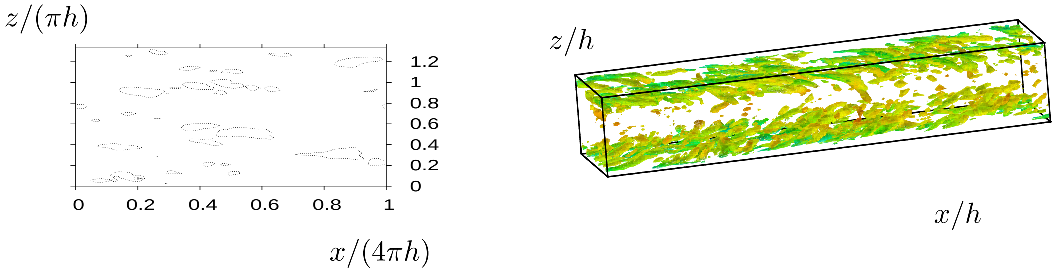

(b) $\mathcal{W}_{body}$, $M = 1.0$, $Re = 3000$

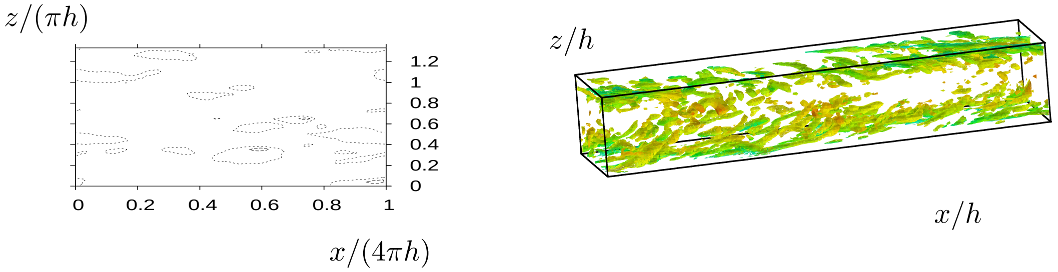

(c) $\mathcal{W}_{body}$, $M = 1.5$, $Re = 3000$

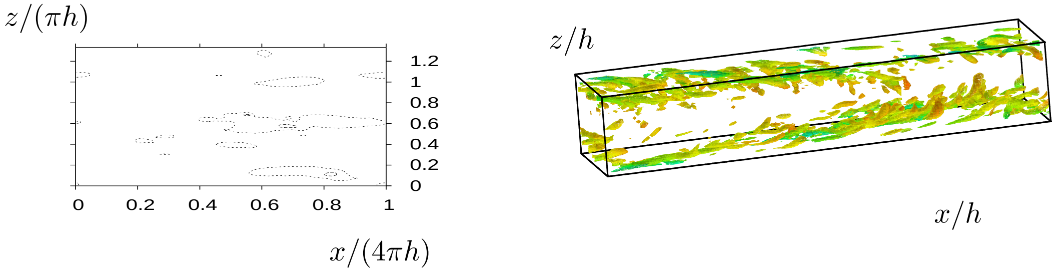

(d) $\mathcal{W}_{body}$, $M = 2.0$, $Re = 3000$

Figure 4.12: **Contour plot of instantaneous wall streamwise velocity in the** $xz$ **plane,** $y/h \sim -0.99$ **(left) and positive Q-criterion isovalues:** $Q = 0.6\frac{u_b^2}{h^2}$ **in the channel flow (right):** $\mathcal{W}_{body}$, $Re = 3000$

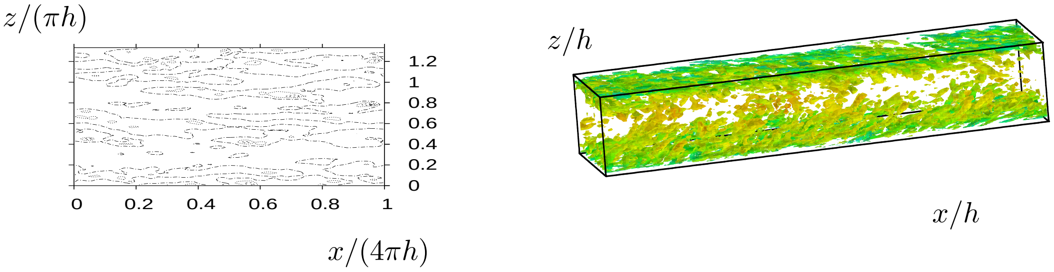

(a) $\mathcal{W}_{body}$, $M = 1.0$, $Re = 4880$

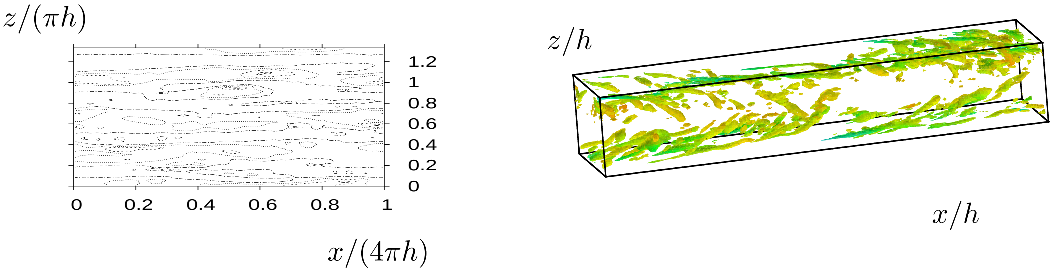

(b) $\mathcal{W}_{body}$, $M = 3.0$, $Re = 4880$

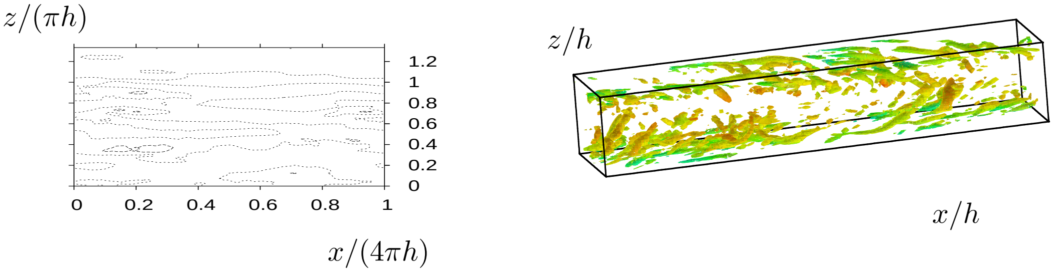

(c) $\mathcal{W}_{ext}$, $M = 3.0$, $Re = 4880$

Figure 4.13: **Contour plot of instantaneous wall streamwise velocity in the** $xz$ **plane,** $y/h \sim -0.99$ **(left) and positive Q-criterion isovalues:** $Q = 0.6\frac{u_b^2}{h^2}$ **in the channel flow (right):** $\mathcal{W}_{body}$ **and** $\mathcal{W}_{ext}$**,** $Re = 4880$

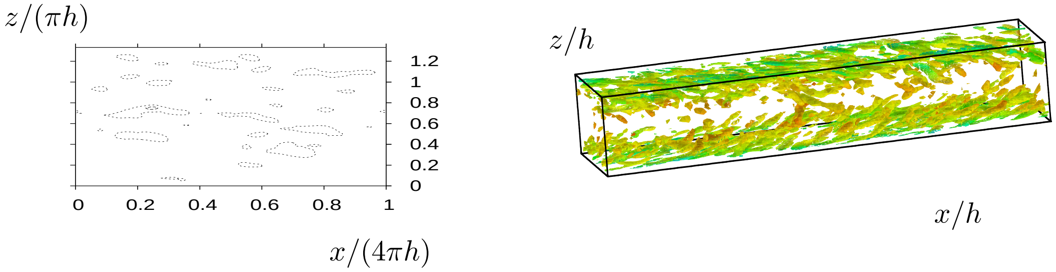

(a) $\mathcal{W}_{int}$, $M = 0.3$, $Re = 3000$

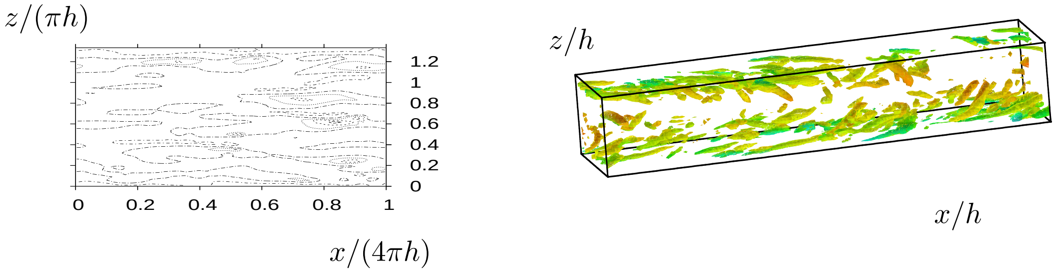

(b) $\mathcal{W}_{int}$, $M = 1.0$, $Re = 3000$

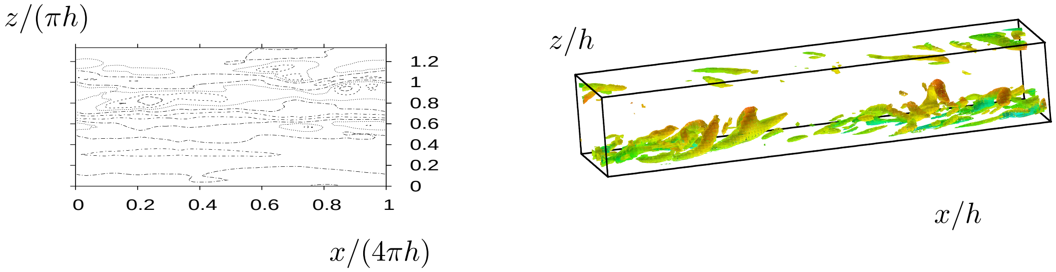

(c) $\mathcal{W}_{int}$, $M = 1.5$, $Re = 3000$

Figure 4.14: **Contour plot of instantaneous wall streamwise velocity in the** $xz$ **plane,** $y/h \sim -0.99$ **(left) and positive Q-criterion isovalues:** $Q = 0.6\frac{u_b^2}{h^2}$ **in the channel flow (right):** $\mathcal{W}_{int}$**,** $Re = 3000$

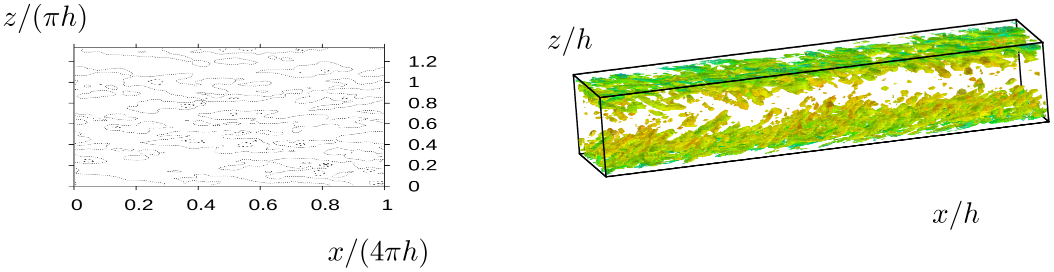

(a) $\mathcal{W}_{int}$, $M = 0.3$, $Re = 4880$

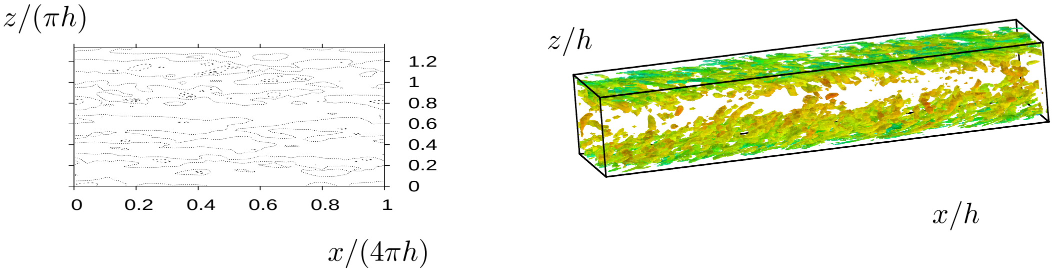

(b) $\mathcal{W}_{int}$, $M = 0.7$, $Re = 4880$

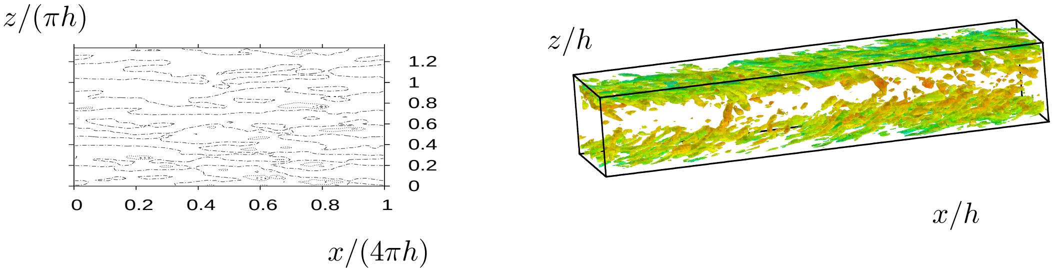

(c) $\mathcal{W}_{int}$, $M = 1.0$, $Re = 4880$

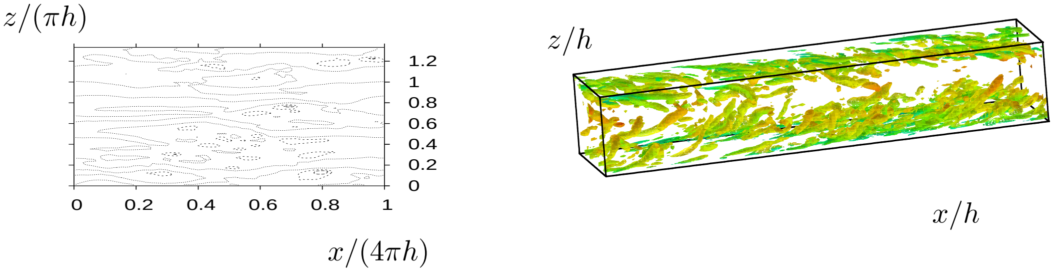

(d) $\mathcal{W}_{int}$, $M = 1.5$, $Re = 4880$

Figure 4.15: **Contour plot of instantaneous wall streamwise velocity in the** $xz$ **plane,** $y/h \sim -0.99$ **(left) and positive Q-criterion isovalues:** $Q = 0.6\frac{u_b^2}{h^2}$ **in the channel flow (right):** $\mathcal{W}_{int}$**,** $Re = 4880$

6, 34]. This assumption which is relatively well satisfied for non-hypersonic adiabatic boundary layers ($M \leq 5$) reads in this context :

$$p_{rms} \ll \langle p \rangle \tag{4.20}$$

$$T_{T_{rms}} \ll \langle T_T \rangle \tag{4.21}$$

The r.m.s. fluctuations of pressure and total temperature $T_T$ ($= T + \frac{1}{2c_p} u_k^2$, definition equivalent to $T_i$ with $Pr_m = 1$, Equation 4.18) are plotted in Figure 4.16. It is noted that, for the present case, the first acoustic condition is much better verified than the second entropic condition. This tendency is even better for the $\mathcal{W}_{int}$ case with less than 1% relative turbulence level (Figure 4.6). The turbulent Mach number

$$M_t = \frac{\sqrt{u_{rms}^2 + v_{rms}^2 + w_{rms}^2}}{\sqrt{\gamma R \langle \tilde{T} \rangle}}$$

is also much lower for the $\mathcal{W}_{int}$ case, which means that the hypersonic limit defined by Bradshaw might be reached at larger Mach number $M$ than expected.

In contrast, the RMS temperature, RMS density and RMS viscosity increase for the $\mathcal{W}_{int}$ case, but are still small (figure 4.17). *Coleman et al.* [14] found that 'these disturbances are mostly of a non-acoustic nature, primarily the result of solenoidal 'passive mixing' across a mean gradient'.

These results confirm that in any case the entropic mode is not negligible for isothermal-wall boundary layer and channel flow [34]. As a direct consequence, the classical SRA set of relations derived from equation (4.21) is not valid for non-adiabatic wall-bounded flows and a new set of relations must be considered.

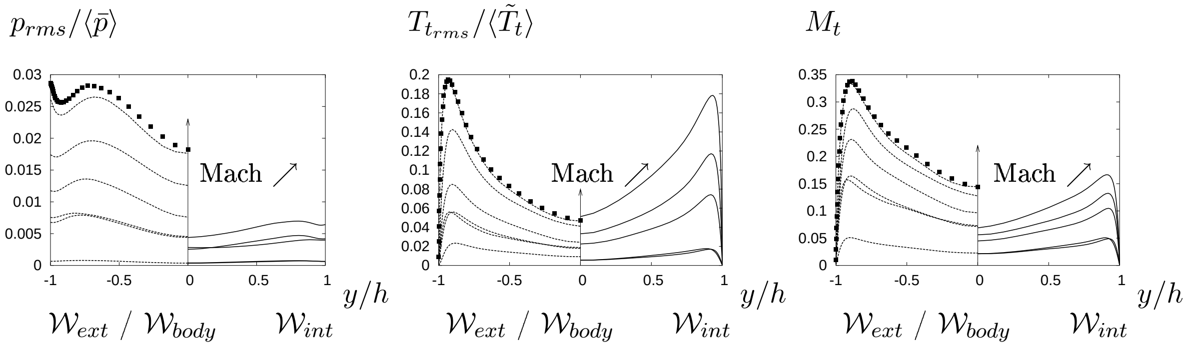

(a) Pressure (b) Total temperature (c) Turbulent Mach number

Figure 4.16: **Pressure fluctuations (a), total temperature fluctuations (b), turbulent Mach number (c), for $\mathcal{W}_{body}$ ( - - - ), $\mathcal{W}_{ext}$ ( ■ ) and $\mathcal{W}_{int}$ ( —— ).**

## 4.7 Reynolds Analogies

O. Reynolds discovered that quantities pertaining to heat transfer may be related with quantities pertaining to momentum transfer based on the similarity of the momentum and energy equations, for incompressible laminar boundary layers. With additional assumptions, the 'Reynolds analogy' has been extended to the compressible and turbulent flows. The concept of 'Strong Reynolds Analogy' (SRA) has been suggested by Morkovin [62] for compressible turbulence. 'Modified Reynolds Analogies' have been developed by several authors, [34, 27, 48].

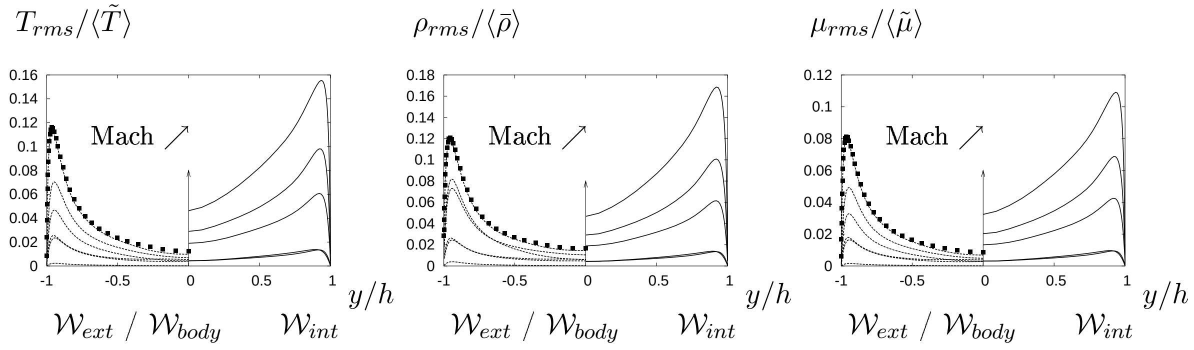

(a) Temperature (b) Density (c) Dynamic Viscosity

Figure 4.17: **Temperature fluctuations, (a) density fluctuations (b), viscosity fluctuations (c), for $\mathcal{W}_{body}$ ( - - - ), $\mathcal{W}_{ext}$ ( ■ ) and $\mathcal{W}_{int}$ ( —— ).**

### 4.7.1 The Strong Reynolds Analogy

The Strong Reynolds Analogy is a useful relation for the reduction of experimental data and the comparison of compressible to incompressible results. It was first identified as such by Morkovin [62], but primarily it was due to Young [93].

In Favre-averaged variables, the boundary-layer form of the compressible $x$-momentum equation and the mean energy equation (developed in terms of the stagnation enthalpy [93]) can be written, respectively [83]

$$\langle\bar{\rho}\rangle\langle\tilde{u}\rangle\frac{\partial\langle\tilde{u}\rangle}{\partial x}+\langle\bar{\rho}\rangle\langle\tilde{v}\rangle\frac{\partial\langle\tilde{u}\rangle}{\partial y} = -\frac{d\langle\bar{p}\rangle}{dx}+\frac{\partial}{\partial y}\left(\langle\tilde{\mu}\rangle\frac{\partial\langle\tilde{u}\rangle}{\partial y}-\langle\bar{\rho}\rangle\langle u'v'\rangle\right) \tag{4.22}$$

$$\langle\bar{\rho}\rangle\langle\tilde{u}\rangle\frac{\partial\langle\tilde{H}\rangle}{\partial x}+\langle\bar{\rho}\rangle\langle\tilde{v}\rangle\frac{\partial\langle\tilde{H}\rangle}{\partial y} = \frac{\partial}{\partial y}\left[\frac{\langle\tilde{\lambda}\rangle}{c_p}\frac{\partial\langle\tilde{H}\rangle}{\partial y}+\langle\tilde{\mu}\rangle(1-\frac{1}{Pr})\frac{\partial}{\partial y}\left(\frac{\langle\tilde{u}\rangle^2}{2}\right)-\langle\bar{\rho}\rangle\langle v'H'\rangle\right] \tag{4.23}$$

where, neglecting higher-order terms, $\langle\tilde{H}\rangle=\langle\tilde{h}\rangle+\frac{1}{2}\langle\tilde{u}\rangle^2$, and $H'=h'+\langle\tilde{u}\rangle u'$.

The Strong Reynolds Analogy is based upon the similarity between Eqs. (4.22) and (4.23) for a stationary, zero-pressure-gradient boundary layer [75, 90]. Consequently, when $Pr=1$ we get an analogy between Reynolds stresses and turbulent heat fluxes. For adiabatic compressible boundary layers, the total enthalpy fluctuations are zero, which yields an anti-correlation between streamwise velocity and temperature,

$$T_i' = 0 \tag{4.24}$$

$$\frac{T'(t)}{\langle\tilde{T}\rangle} = -(\gamma-1)M_l^2\frac{u'(t)}{\langle\tilde{u}\rangle} \tag{4.25}$$

Gaviglio [28] notes that these relations apply in an instantaneous sense, but they cannot be expected to hold exactly. Morkovin [62] has developed a set of statistical relations referred to as 'Strong Reynolds Analogy' (SRA), that relates the r.m.s. of the static temperature fluctuations to that of the velocity fluctuations. These relations are

$$\frac{T_{rms}}{\langle \tilde{T} \rangle} = (\gamma - 1) M_l^2 \frac{u_{rms}}{\langle \tilde{u} \rangle} \tag{4.26}$$

$$R_{u'T'} = \frac{< u'T' >}{u_{rms} T_{rms}} = -1 \tag{4.27}$$

$$< v'T' > = -\frac{\langle \tilde{u} \rangle}{C_p} < u'v' > \tag{4.28}$$

$$\frac{< v'T' >}{\langle \tilde{T} \rangle} = -(\gamma - 1) M_l^2 \frac{< u'v' >}{\langle \tilde{u} \rangle} \tag{4.29}$$

$$< v'T_i' > = < v'T' > + \frac{\langle \tilde{u} \rangle}{C_p} < u'v' > = 0 \tag{4.30}$$

Morkovin [62] and Gaviglio [28] have found that $R_{u'T'}$ is close to $-0.8$ or $-0.9$. It should be noted that $T_i'$ is not negligible , but that relations derived based on this assumption represent good approximations [63, 44, 23, 79].

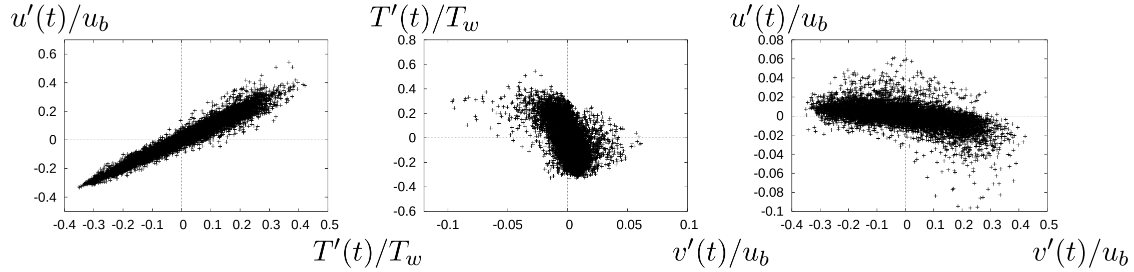

(a) $\mathcal{W}_{int}$ : $\tilde{u}\tilde{T}$ correlation (b) $\mathcal{W}_{int}$ : $\tilde{T}\tilde{v}$ correlation (c) $\mathcal{W}_{int}$ : $\tilde{u}\tilde{v}$ correlation

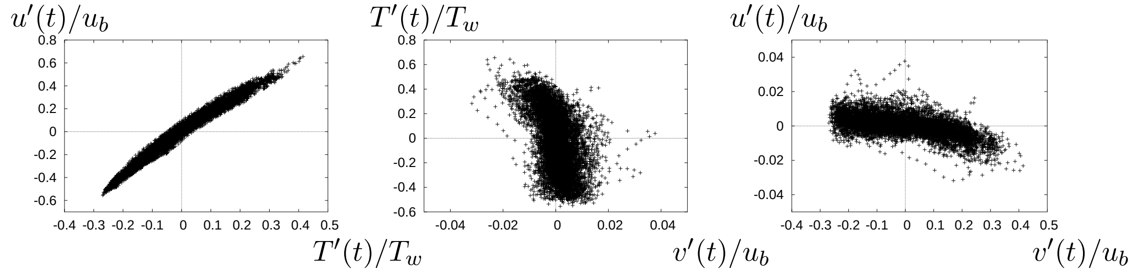

(d) $\mathcal{W}_{body}$ : $\tilde{u}\tilde{T}$ correlation (e) $\mathcal{W}_{body}$ : $\tilde{T}\tilde{v}$ correlation (f) $\mathcal{W}_{body}$ : $\tilde{u}\tilde{v}$ correlation

Figure 4.18: **Channel flow: crosspdf for** $Re = 4880$**,** $M = 1$ **and** $\mathcal{W}_{int}$ **at** $y^+ = 19.6$ **(a,b,c) and crosspdf for** $Re = 4880$**,** $M = 3$ **and** $\mathcal{W}_{body}$ **at** $y^+ = 20.4$ **(d,e,f).**

### 4.7.2 Modified Strong Reynolds Analogies

The classical SRA relations developed in the framework of adiabatic compressible boundary layers do not hold for isothermal boundary layers including compressible channel flow [34, 27, 48]. For example, figures (4.18) and (4.19) show a positive correlation between $\tilde{T}$ and $\tilde{u}$ in the buffer

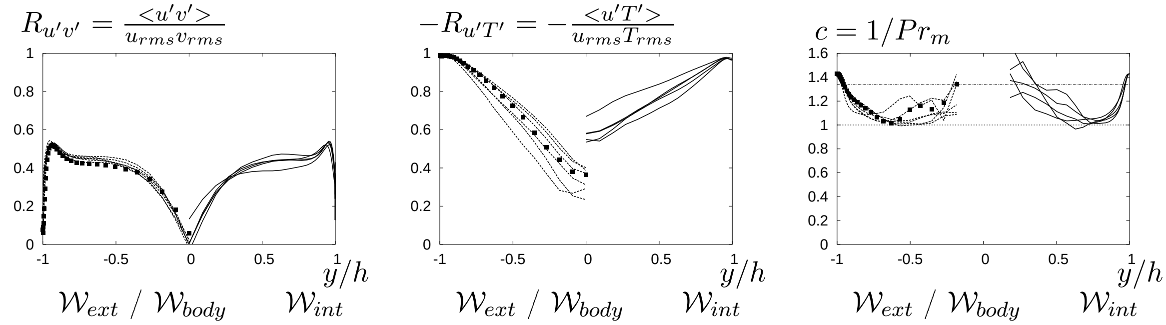

(a) uv correlation (b) ut correlation (c) MSRA $c$ coefficient

Figure 4.19: **Channel flow: correlation coefficient for the Reynolds stress tensor (a), correlation coefficient for the turbulent heat flux (b), MSRA $c$ coefficient (c): $\mathcal{W}_{body}$ ( - - - ), $\mathcal{W}_{ext}$ ( ■ ) and $\mathcal{W}_{int}$ ( —— ).** $Re = 3000$ **and** $Re = 4880$, $0.3 \leq M \leq 2$.

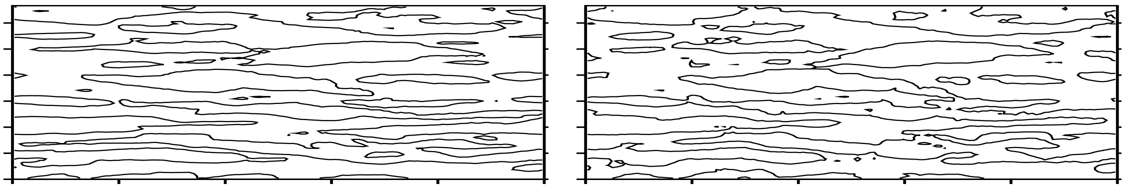

(a) isovalues of $u_\tau = \langle u_\tau \rangle$ (b) isovalues of $T_\tau = \langle T_\tau \rangle$

Figure 4.20: **Isovalues of instantaneous friction velocity (a) and instantaneous friction temperature (b) for $\mathcal{W}_{int}$,** $M = 1.5$, $Re = 4880$.

layer region for the channel flow while a negative correlation is expected for adiabatic boundary layer (equation 4.27). This strong correlation is also very clear on instantaneous visualizations of the two main quantities $u_\tau$ and $T_\tau$ for the fully developed channel flow which represent the trace of the streaks at the wall (figure 4.20).

Thus, for non-adiabatic boundary layers, other assumptions than Morkovin's hypothesis must be considered. For isothermal boundary layers, Cebecci & Smith [12] demonstrated rigorously a so called 'Extended Strong Reynolds Analogy' (ESRA), based on the Crocco-Busemann relations (Equation 4.4),

$$\frac{T'(t)}{\langle\tilde{T}\rangle} = \left[1 + Cp\frac{T_w - T_{te}}{\langle\tilde{T}\rangle}\frac{\langle\tilde{u}\rangle}{u_e}\right](\gamma - 1)M_l^2\frac{u'(t)}{\langle\tilde{u}\rangle} \tag{4.31}$$

Gaviglio [28], Rubesin [71] and Huang *et al.* [34] proposed new general relations based on the total temperature variation $\partial\langle\tilde{T}_i\rangle/\partial\langle\tilde{T}\rangle$ which will be called 'Modified Strong Reynolds Analogies' (MSRA) [30],

$$\frac{T'(t)}{\langle\tilde{T}\rangle} = \frac{1}{c\left(a\partial\langle\tilde{T}_i\rangle/\partial\langle\tilde{T}\rangle - 1\right)}(\gamma - 1)M_l^2\frac{u'(t)}{\langle\tilde{u}\rangle} \tag{4.32}$$

If $a = 0$ and $c = 1$ then the standard SRA is obtained. For the modified expressions $a = 1$.

In a similar way as in [12], from relations (4.6) and (4.7) which are only valid in channel flow (with either source term), it is derived an analogy between temperature fluctuations and velocity fluctuations which yields a strong positive correlation (Figure 4.18) :

- $\mathcal{W}_{ext}$ model [31]:

$$\frac{T'(t)}{\langle\tilde{T}\rangle} \quad = \quad (\gamma - 1)\ Pr\ M_l^2\left(\frac{u_b}{\langle\tilde{u}\rangle} - \frac{2}{3}\right)\frac{u'(t)}{\langle\tilde{u}\rangle} \tag{4.33}$$

- $\mathcal{W}_{int}$ model :

$$\frac{T'(t)}{\langle\tilde{T}\rangle} \quad = \quad Pr\ M_l^2\left(\gamma\frac{u_b}{\langle\tilde{u}\rangle} + \frac{3 - 2\gamma}{3}\right)\frac{u'(t)}{\langle\tilde{u}\rangle} \tag{4.34}$$

It is interesting to note that the two relations above could be derived as well using the MSRA relation (4.32) and accounting for the present definition of the total temperature $T_i$ (Equation 4.18) and the specific Crocco-Busemann relation for the channel flow (Equation 4.6 or 4.7),

$$C_{ext}^{Ti} = \frac{1}{\partial\langle\tilde{T}_i\rangle/\partial\langle\tilde{T}\rangle_{ext} - 1} \quad = \quad \frac{Pr}{Pr_m}\left(\frac{u_b}{\langle\tilde{u}\rangle} - \frac{2}{3}\right) \tag{4.35}$$

$$C_{int}^{Ti} = \frac{1}{\partial\langle\tilde{T}_i\rangle/\partial\langle\tilde{T}\rangle_{int} - 1} \quad = \quad \frac{Pr}{Pr_m}\ \frac{1}{\gamma - 1}\left(\gamma\frac{u_b}{\langle\tilde{u}\rangle} + \frac{3 - 2\gamma}{3}\right) \tag{4.36}$$

In the present case, the coefficient $c = 1/Pr_m$ is the same for both source terms and is varying between $c = 1/Pr \approx 1.4$ at the wall and $c = 1/Pr_t \approx 1$ in the core of the channel (Figure 4.19c), which is conform with the values set to $c = 1$ for Gaviglio and $c = 1.34$ for Rubesin. Contrastingly, Huang *et al.* relate the coefficient to the turbulent Prandtl number $c = Pr_t$ whose value is $c \approx 1$ anyway. The relation (4.32) proposed by Huang *et al.* appears finally as a very general analogy where the $c$ coefficient is a function of the boundary conditions of the problem. A set of statistical CESRA relations can be further derived including the temperature derivative coefficient $C^{Ti}$ and the mixed Prandtl number $Pr_m$ :

$$\frac{T_{rms}}{\langle \tilde{T} \rangle} = C^{Ti}\ Pr_m\ (\gamma - 1)\ M_l^2\ \frac{u_{rms}}{\langle \tilde{u} \rangle} \tag{4.37}$$

$$< v'T' > = C^{Ti}\ Pr_m\ \frac{\langle \tilde{u} \rangle}{C_p} < u'v' > \tag{4.38}$$

$$R_{u'T'} = \frac{< u'T' >}{u_{rms} T_{rms}} = sign(C^{Ti}) = 1 \tag{4.39}$$

$$< v'T_i' > = < v'T' > \left(1 + \frac{1}{C^{Ti}\ Pr_m}\right) \tag{4.40}$$

Figures (4.21), (4.22) and (4.23) show the success of the modified SRA applied to the channel flow (CESRA) for both the cases $\mathcal{W}_{body}$ and $\mathcal{W}_{int}$ (equations 4.37-4.40). This would confirm that, although the entropic modes (total temperature fluctuations) are non-zero, there could exist a kind of universality of the turbulence structure in non adiabatic compressible boundary layers.

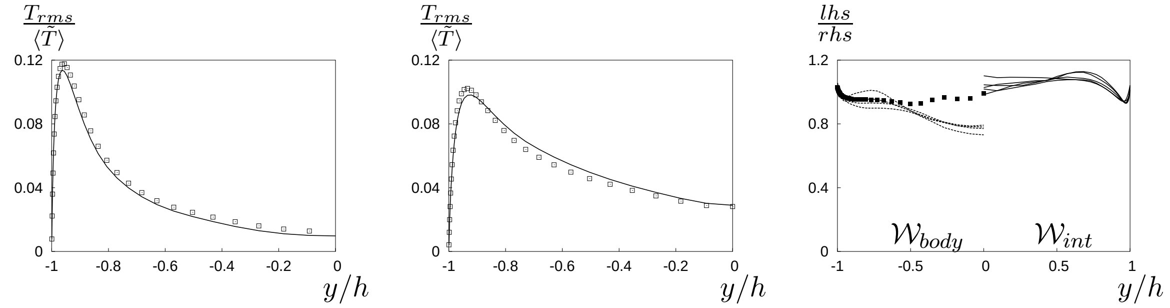

(a) $\mathcal{W}_{body} : M = 3, Re = 4880$ (b) $\mathcal{W}_{int} : M = 1.0, Re = 4880$ (c) equation 4.37

Figure 4.21: **Temperature RMS : —— , direct computation; □ , CESRA analogy; for** $Re = 4880$**,** $M = 1$**,** $\mathcal{W}_{body}$ **(a), for** $Re = 4880$**,** $M = 3$**,** $\mathcal{W}_{int}$ **(b). CESRA equation 4.37** $\frac{lhs}{rhs}$ **for** $\mathcal{W}_{body}$ **( - - - ),** $\mathcal{W}_{ext}$ **( ■ ) and** $\mathcal{W}_{int}$ **( —— ) at** $3000 \leq Re \leq 4880$**,** $0.3 \leq M \leq 2$ **(c).**

## 4.8 Summary

LES of compressible channel flow have been performed and analysed for the two source term descriptions (Section 2.3). Comparisons between these two source terms show a main difference in terms of heating effect, yielding a maximum temperature in the center of the channel about 4.5 times larger for the second formulation presently derived.

Compressibility and low Reynolds number effects have been analysed in terms of coherent structures and statistics. We found that the direct effects of compressibility on the mean flow appear to be rather small: the most notable differences may be attributed to the variation in fluid properties across the channel.

We proposed an analytical framework for the determination of the $c$ constant in the so-called modified strong Reynolds analogy by ***Huang et al.*** based on Crocco-Busemann type relations derived for compressible channel flow. We obtained $c = 1/Pr_m$ and showed that the account for

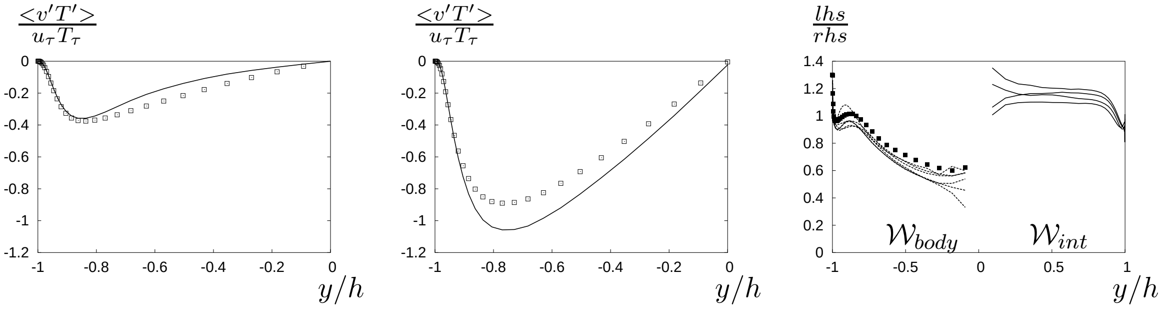

(a) $\mathcal{W}_{body} : M = 3, Re = 4880$ (b) $\mathcal{W}_{int} : M = 1.0, Re = 4880$ (c) equation 4.38

Figure 4.22: **Temperature wall-normal velocity correlation : —— , direct computation; □ , CESRA analogy; for $Re = 4880$, $M = 1$, $\mathcal{W}_{body}$ (a), for $Re = 4880$, $M = 3$, $\mathcal{W}_{int}$ (b). CESRA equation 4.38 $\frac{lhs}{rhs}$ for $\mathcal{W}_{body}$ ( - - - ), $\mathcal{W}_{ext}$ ( ■ ) and $\mathcal{W}_{int}$ ( —— ) at $3000 \leq Re \leq 4880$, $0.3 \leq M \leq 2$ (c).**

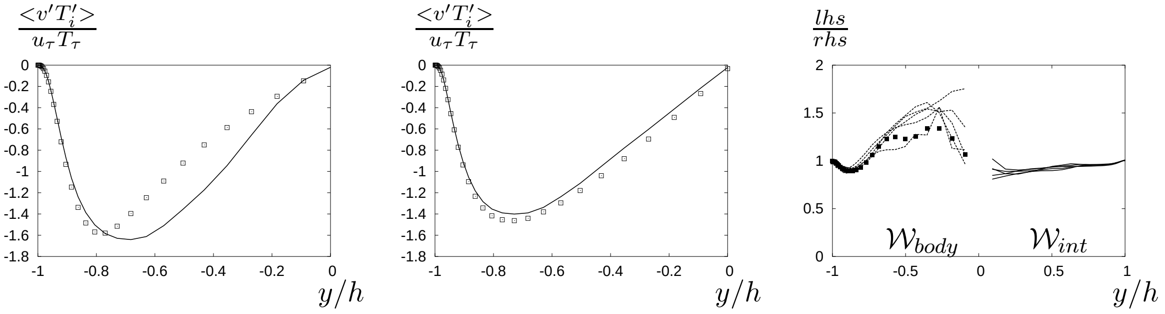

(a) $\mathcal{W}_{body} : M = 3, Re = 4880$ (b) $\mathcal{W}_{int} : M = 1.0, Re = 4880$ (c) equation 4.40

Figure 4.23: **Total temperature wall-normal velocity correlation : —— , direct computation; □ , CESRA analogy; for $Re = 4880$, $M = 1$, $\mathcal{W}_{body}$ (a), for $Re = 4880$, $M = 3$, $\mathcal{W}_{int}$ (b). CESRA equation 4.40 $\frac{lhs}{rhs}$ for $\mathcal{W}_{body}$ ( - - - ), $\mathcal{W}_{ext}$ ( ■ ) and $\mathcal{W}_{int}$ ( —— ) at $3000 \leq Re \leq 4880$, $0.3 \leq M \leq 2$ (c).**

the mixed Prandtl number $Pr_m$ in the CESRA yields a good fit of the results for both source term formulations.

# CHAPTER 5

# Spatially developing compressible channel flow with and without distortion by means of a streamwise adverse pressure gradient

In this chapter simultions of the turbulent compressible flow developing spatially with and without streamwise adverse pressure gradient are presented. These results might validate the model of the fully turbulent compressible channel flow with a $\mathcal{W}_{int}$ source term.

Firstly, a simulation of the turbulent compressible flow developing spatially is presented. The principle, described in Section 2.5, is to consider a fully developed channel flow in order to ensure realistic inflow conditions for the spatial channel. This one is split in several identical computational boxes. Non-reflecting outflow conditions are applied at the outlet of the spatial channel. The flow geometry is shown in Figure 5.1. [1]

The boundary conditions are checked and general flow features of the simulation are discussed.

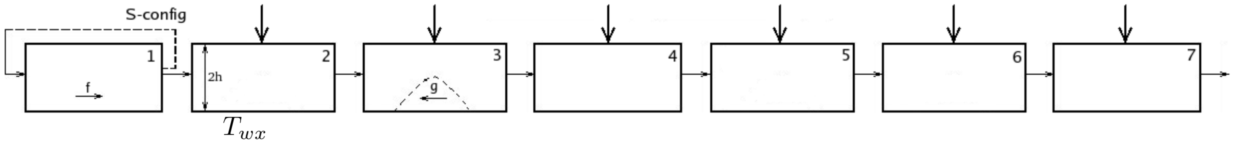

Figure 5.1: **Geometry of the spatially developing/separating channel flow**

In the next section, a simulation of a distorted compressible channel flow is presented. The flow distortion is the result of a pressure gradient change of sign in the streamwise direction. This change is done artificially using a distributed force implemented in the Navier-Stokes equations (see Section 2.6). We discuss the response of the subsonic turbulent flow to this change in pressure gradient.

Instantaneous and mean flow features and anisotropy invariants are investigated for both simulations, with and without streamwise adverse pressure gradient. The nature of fluctuating variables and the modified strong Reynolds analogy for the channel (CESRA) are also investigated for both simulations.

The chapter ends with a summary of the main results.

---

[1] In what follows, the computational box $n$ will be referred to as the spatial computational box $n-1$. Results from the spatial domain are compared with results from the incoming fully developed channel flow.

LES of spatially developing compressible channel flow, with and without streamwise adverse pressure gradient, were presently performed for geometries with 4 (not presented here) and 7 computational boxes, for a Reynolds number of $Re = 4,880$ and a Mach number of $M = 0.7$. A subsonic flow was chosen for mainly two reasons. First, in real flows, a subsonic region always exists close to the wall. And second, the most difficult case to treat from the wave propagations point of view is the subsonic case. Thus, the validation of the subsonic flow is needed before simulating supersonic cases.

The size of the computational domain is reported in Table 3.1. The results are compared to the fully developed channel flow presented in Chapter 4.

Statistics were computed considering only one homogeneous direction (i.e. the spanwise direction) and using Reynolds averaging procedures.

## 5.1 Spatially developing compressible channel flow

First, we are interested in the stability and convergence of the method used to impose both the inflow and the outflow boundary conditions. In Figure 5.2 the temporal evolution of the instantaneous mass flux is shown at two locations in the channel, at the centreline and at the first grid point, respectively. In the center of the channel, both the inlet and the outlet mass flux oscillate together around a mean value of 1.1, while, at the first grid point, the outlet mass flux takes negative values before oscillating around a mean value of 0.02. The mean value for the inlet mass flux is about 0.01. At the end of the simulation, Figure 5.3, both the inlet and the outlet mass flux, at the first grid point, are oscillating together.

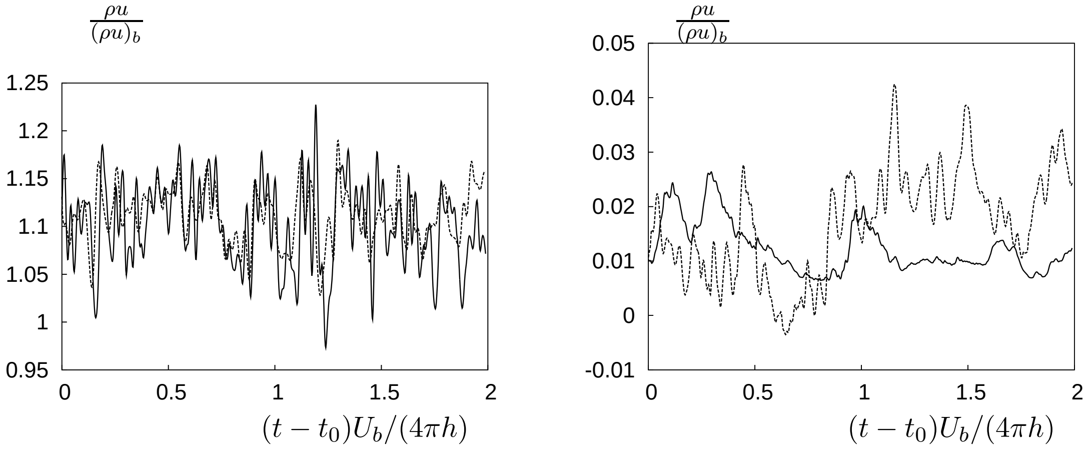

(a) Centreline

(b) First point of the grid

Figure 5.2: **Time variations of the inlet ( —— ) and the outlet ( - - - ) mass flux at (a) the centreline and (b) at the first grid point in the wall-normal direction.**

In order to check the inlet boundary condition, positive Q-criterion isovalues in the incoming fully developed channel flow and in the first spatial computational box are plotted in Figure 5.4. Since the velocity and the temperature of a slice of the inflow channel were imposed at the inlet, a continuity between the coherent structures in the two computational boxes is found.

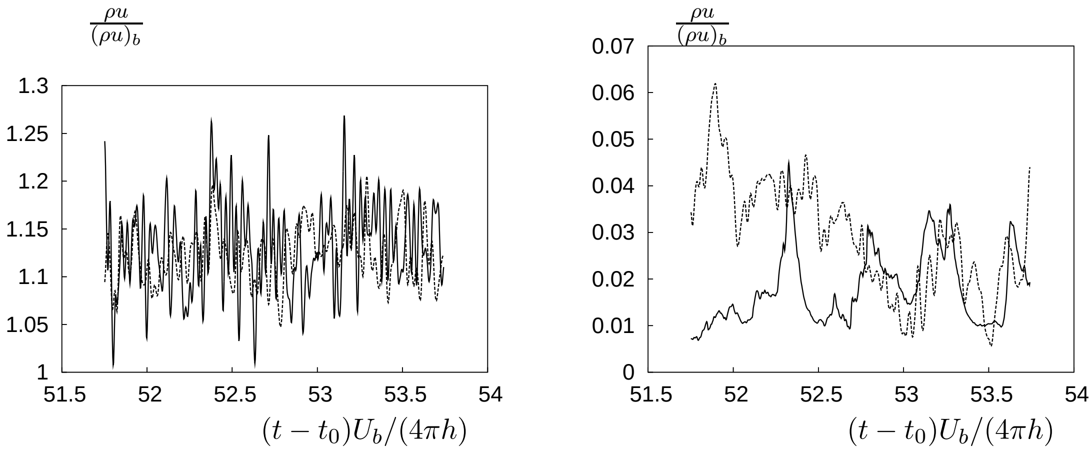

(a) Centreline

(b) First point of the grid

Figure 5.3: **Time variations of the inlet ( ——— ) and the outlet ( - - - ) mass flux at (a) the centreline and (b) at the first grid point in the wall-normal direction.**

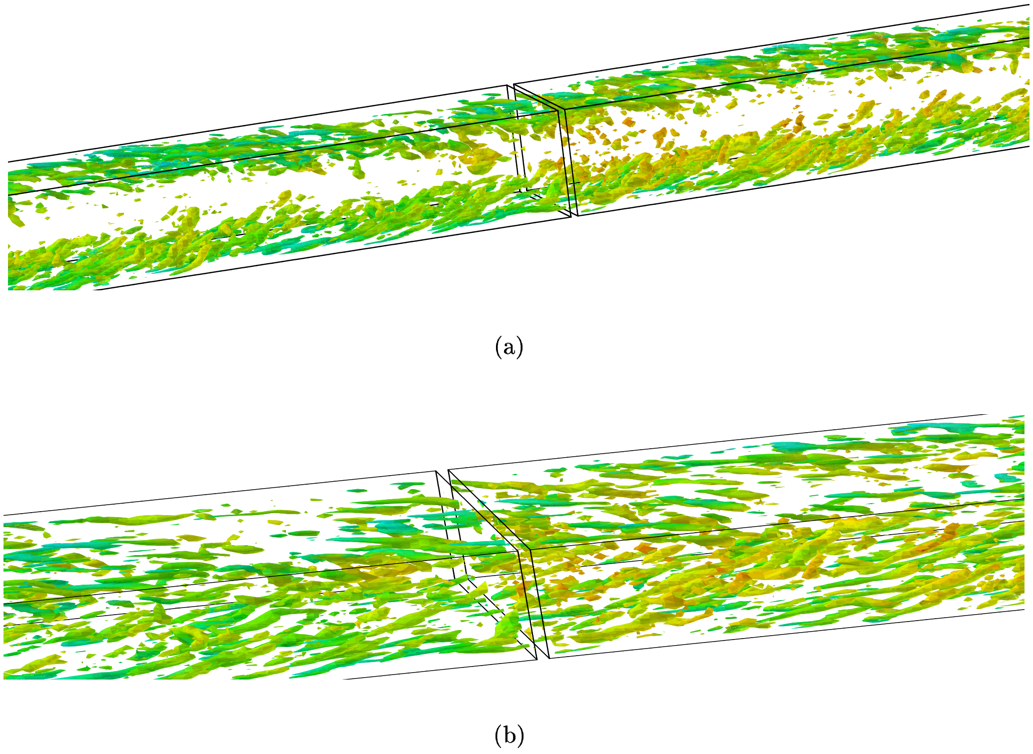

Figure 5.4: **Zoom of the positive Q-criterion isovalues:** $Q = \frac{u_b^2}{h^2}$ **in the inlet of the spatial channel.** $Re = 4,880$ **and** $M = 0.7$**.**

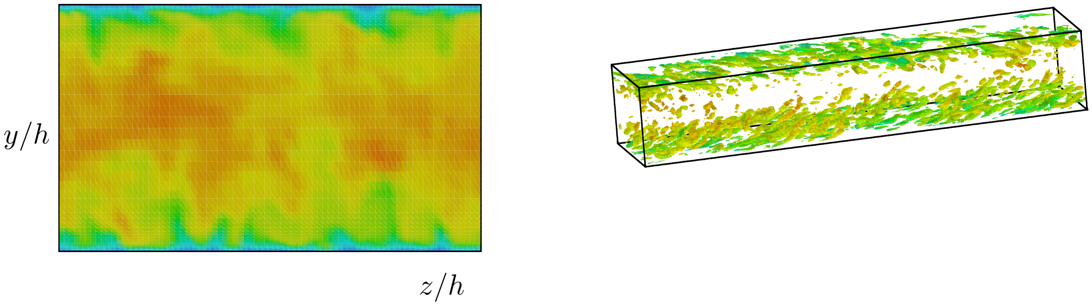

(a) first spatial computational box

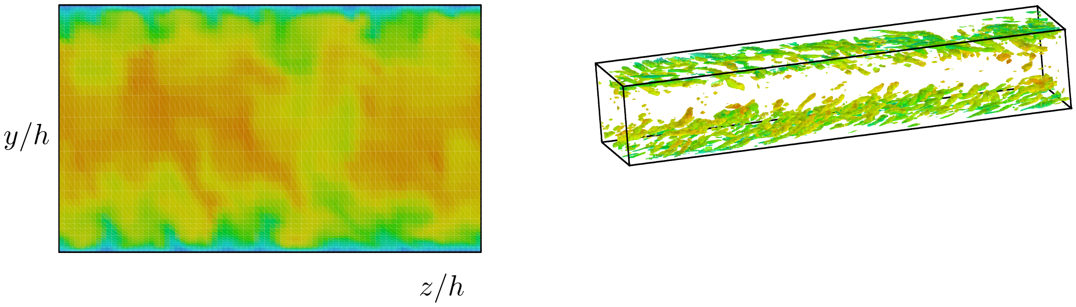

(b) second spatial computational box

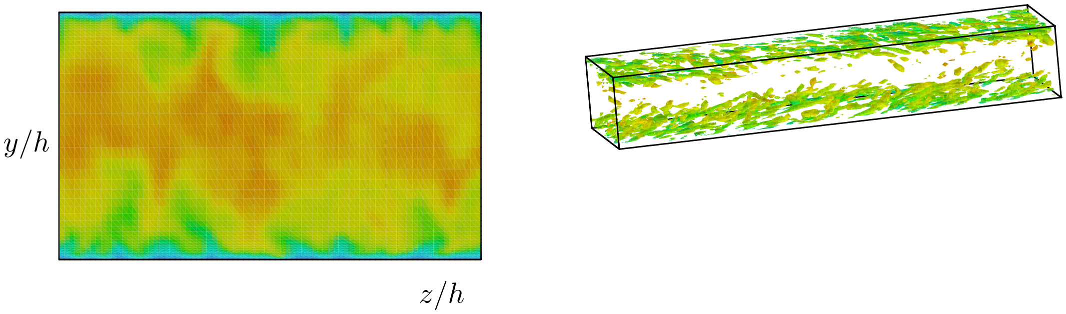

(c) sixth spatial computational box

Figure 5.5: **Contour plot of instantaneous streamwise velocity in the $yz$ plane (left) and positive Q-criterion isovalues: $Q = \frac{u_b^2}{h^2}$ (right) in the spatial channel.** $Re = 4,880$ **and** $M = 0.7$**.**

A quick check of the positive Q-criterion isovalues shows also a continuity in terms of coherent structures in the spatial channel (Figure 5.5, right). Instantaneous visualizations are presented for the first, second and sixth spatial computational boxes. The remaining plots can be found in Figure A.3. Near the wall, there are regions of slow moving fluid, known as low-speed streaks. These regions alternate with high-speed moving fluid. The low-speed streaks gradually lift up from the wall, oscillate and then break up violently. The term describing this sequence is 'bursting', coined by *Kline et al.* [45]. Nearly all of the turbulence production is occuring during bursting in the wall region [41]. Indication of the presence of mushroom shaped bursts, which have been seen experimentally [13], are illustrated in Figure 5.5, left.

Figures 5.6 and 5.7 show the $x$-profiles of both instantaneous and mean flow variables. As expected the streamwise velocity (Fig. 5.6a) is the same as in the fully developed channel flow. A drop in terms of pressure and temperature (Figs. 5.7c and 5.7a, respectively) is noticed in the streamwise direction which is an attribute of the naturally developing channel flow. Correct distributions are obtained in the spatial channel, although slight differences are found between expected and obtained distributions of the density (Fig. 5.7b) and, implicitely, of the pressure (Fig. 5.7c). These differences might explain the loss in the mean spanwise velocity (Fig. 5.6c) at the end of the channel.

To gain more insight into these results, isovalues of the mean flow variables are considered (Fig. 5.8). The mean pressure isovalues (Fig. 5.8f) show a constant pressure gradient in the spatial channel. However, small perturbations near the inlet and the outlet are observed. This behavior might be due to the no corner treatment.

No boundary layer behavior is observed in the streamwise velocity, density or temperature fields (Figs. 5.8a, 5.8e and 5.8d, respectively). The mean wall-normal and the mean spanwise velocities (Figs. 5.8b and 5.8c, respectively) seem to be marginally converged, consequently we will consider hereafter for their averaging an additional homogeneous direction, the streamwise direction of the flow.

In Figures 5.9 and A.1 all the important quantities at the wall are plotted. Both the velocity and temperature gradients (Figs. A.1a and A.1b, respectively) are increasing in the streamwise direction. Despite this, the wall friction $\tau_w$ and the friction velocity $u_\tau$ (Figs. A.1c and 5.9a, respectively) are nearly constant in the $x$-direction, apart from the inlet and the outlet. Contrary, increasing distributions are found for the wall heat flux $q_w$, the friction temperature $T_\tau$ and the friction Mach number $M_\tau$, respectively (Figs. A.1d, 5.9b and 5.9d, respectively). Values of the $M_\tau^c$ coefficient (Fig. 5.9e) are around 0.2, although a constant evolution of this coefficient was expected. All these quantities will be further used in the wall modelling.

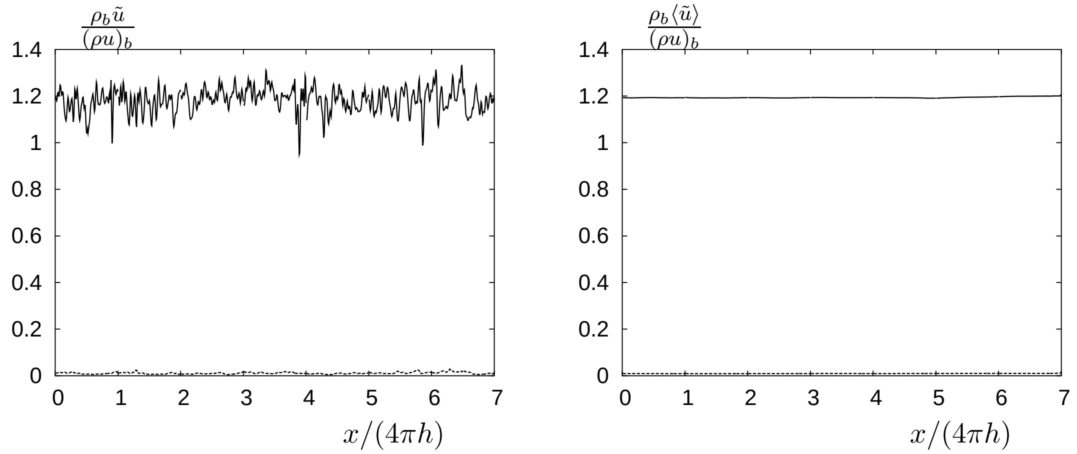

(a) Instantaneous and mean streamwise velocity

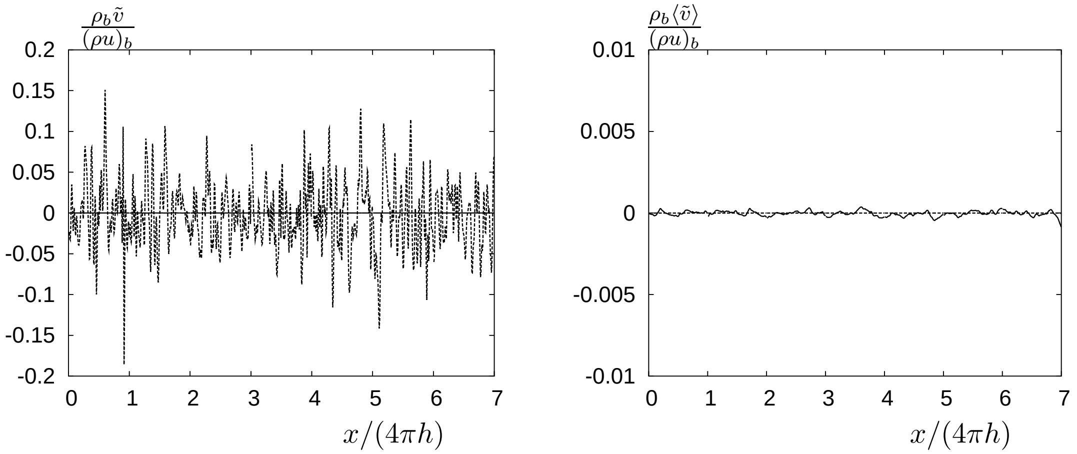

(b) Instantaneous and mean wall-normal velocity

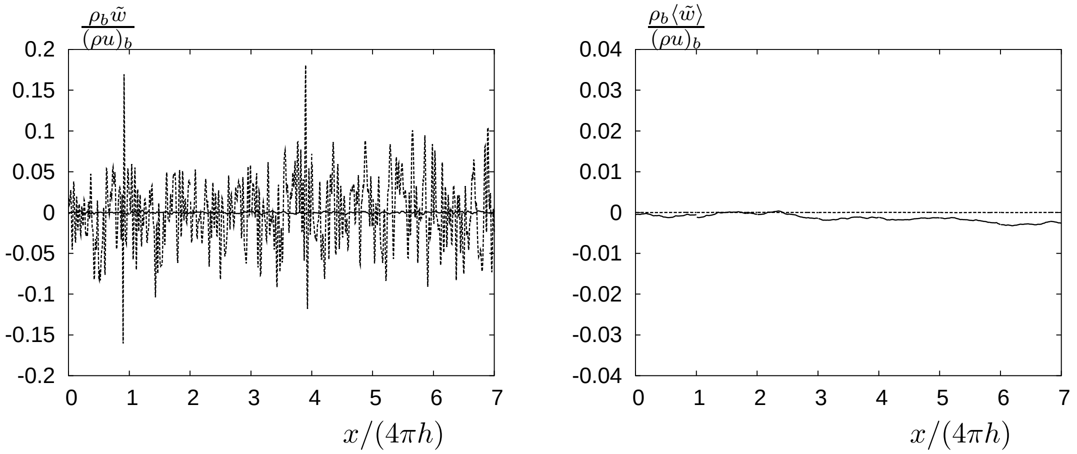

(c) Instantaneous and mean spanwise velocity

Figure 5.6: **Instantaneous and mean (a) streamwise, (b) wall-normal and (c) spanwise velocity profiles in the $x$-direction at the centreline ( —— ) and at the first grid point in the wall-normal direction ( - - - ).**

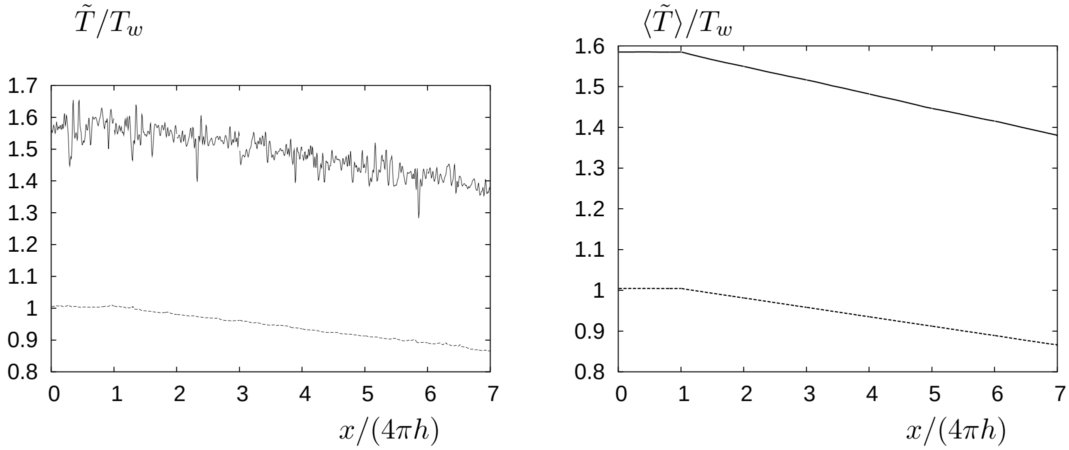

(a) Instantaneous and mean temperature

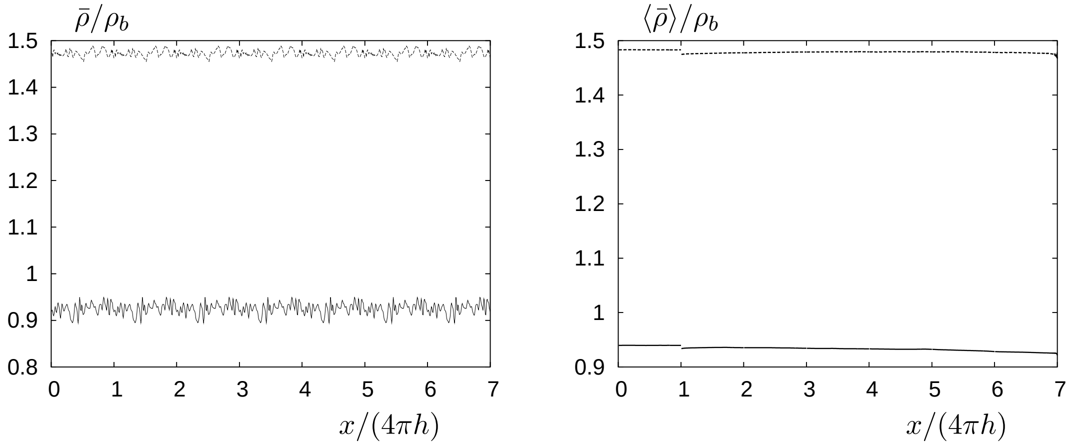

(b) Instantaneous and mean density

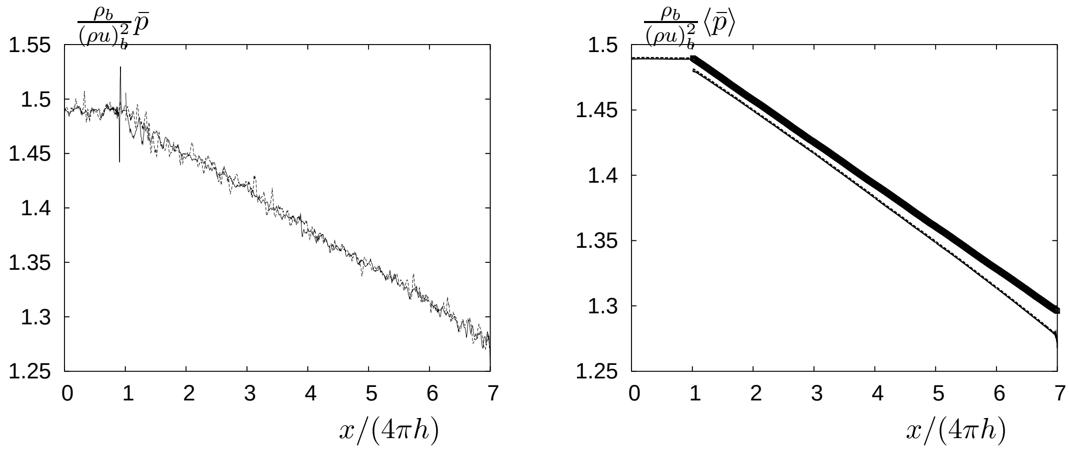

(c) Instantaneous and mean pressure

Figure 5.7: **Instantaneous and mean streamwise profiles of temperature (a), density (b) and pressure (c) at the centreline ( ——— ) and at the first grid point in the wall-normal direction ( - - - ).**

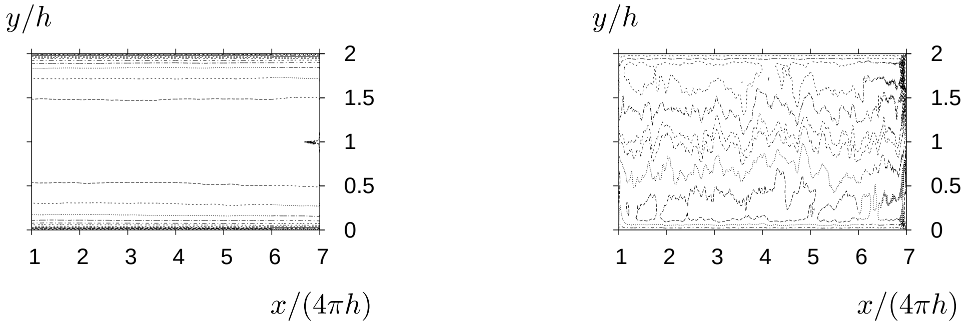

(a) Mean streamwise velocity

(b) Mean wall-normal velocity

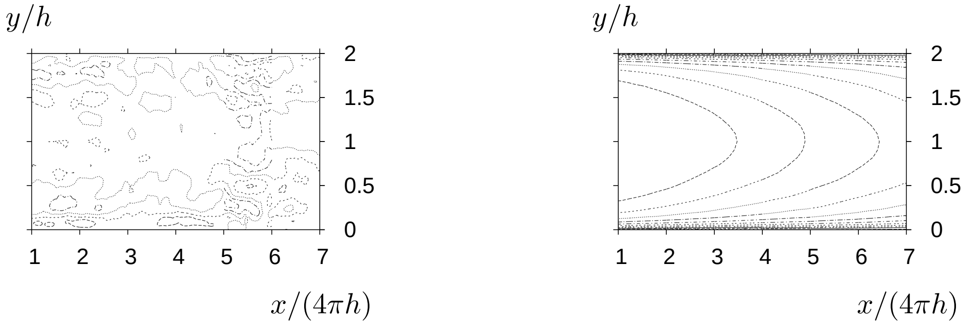

(c) Mean spanwise velocity

(d) Mean temperature

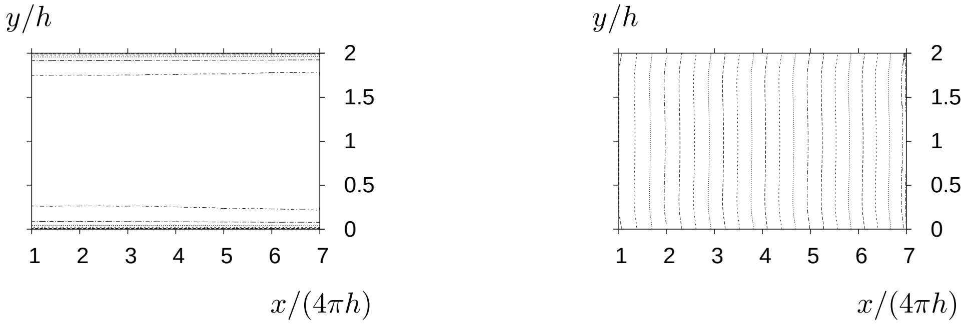

(e) Mean density

(f) Mean pressure

Figure 5.8: **Isovalues of mean streamwise (a), wall-normal (b) and spanwise (c) velocity, mean temperature (d), mean density (e) and mean pressure (f).**

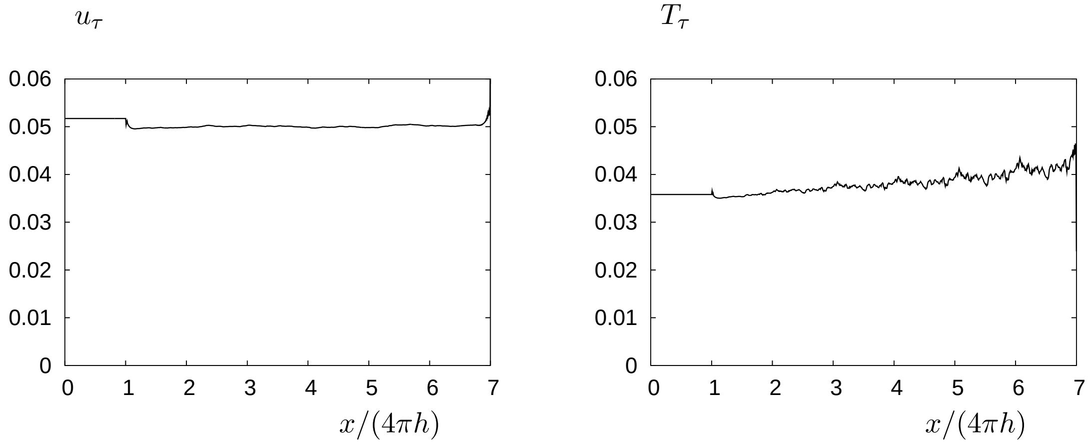

(a) Friction velocity

(b) Friction temperature

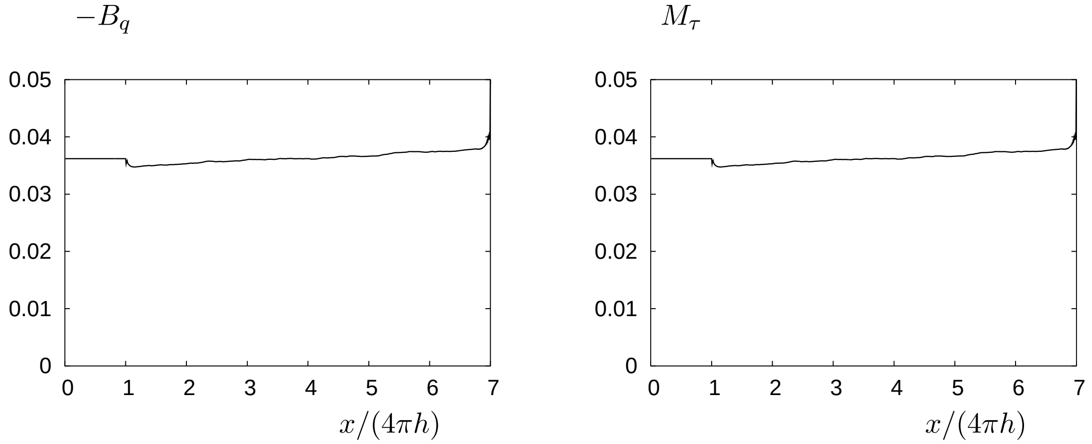

(c) Non-dimensional heat flux

(d) Friction Mach number

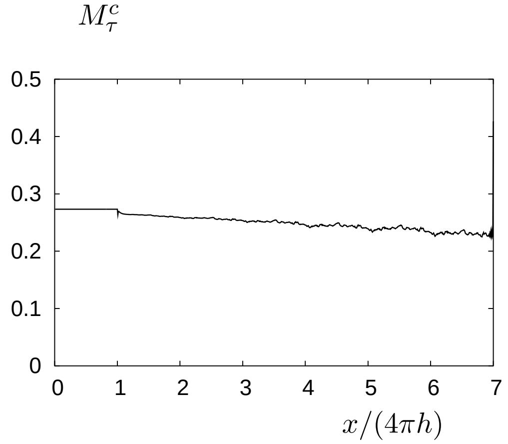

(e) $M_\tau^c = \frac{M_\tau}{\sqrt{-B_q}} = \frac{u_\tau}{\sqrt{\gamma R T_\tau}}$

Figure 5.9: **Distributions of the the friction velocity (a), the friction temperaure (b), the non-dimensional heat flux (c), friction Mach number (d) and the $M_\tau^c$ coefficient (e) in the spatially developing channel flow at $Re = 4880$ and $M = 0.7$.**

## 5.2 Distorted compressible channel flow

The spatially developing field described in Section 5.1 computed with $\mathcal{W}_{int}$ source term at the Reynolds number of $Re = 4880$ and the Mach number of $M = 0.7$ is used as initial condition for the simulation. The force (see Section 2.6) is applied in the second spatial computational box. The effect of this distributed force is to decelerate the flow near the lower wall while accelerating the flow near the opposite wall. This is clearly shown in Figure 5.10(a) via the velocity gradient on the lower and upper surfaces. The impact on the near-wall temperature is shown in Figure 5.10(b). It is noticed that the maximum distortions in both streamwise velocity and temperature are obtained nearly in the middle of the second spatial computational box.

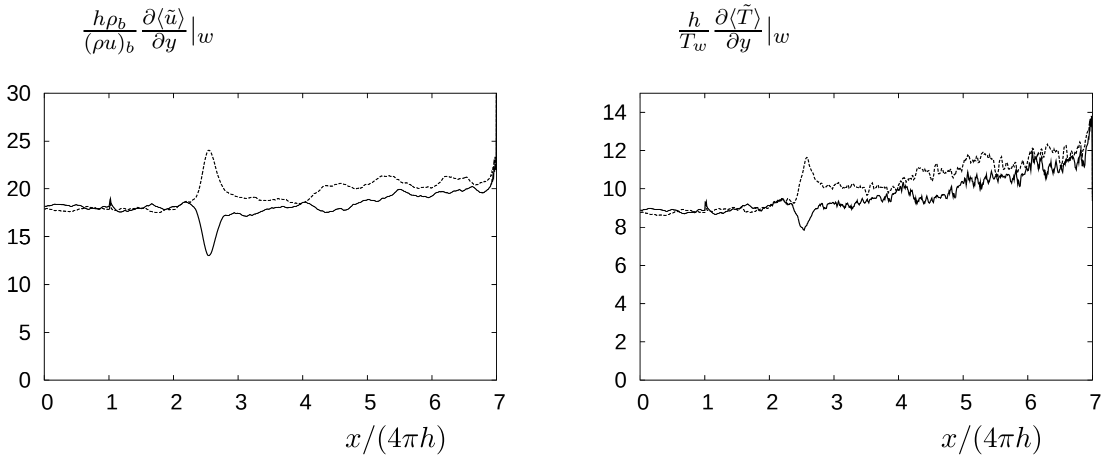

(a) Streamwise velocity gradient

(b) Temperature gradient

Figure 5.10: **Streamwise velocity gradient (a) and temperature gradient (b) on the lower ( —— ) and upper ( - - - ) surfaces of the channel.**

The coefficients of skin friction $C_f = \frac{2\tau_w}{\rho_b u_b^2}$, heat transfer $C_h = \frac{q_w}{\rho_b u_b c_p(\langle\tilde{T}_c\rangle - T_w)}$ (the $c$ subscript reffers to the values in the centre of the channel flow) and pressure $C_p = \frac{\langle\bar{p}\rangle - \langle\bar{p}_c\rangle}{U_b^2}$ are shown in Figures 5.11. The flow deceleration lead to a local distortion of the flow (Figure 5.11(c)) which starts at the $\frac{x}{4\pi h} \simeq 2.19$ location and ends at the $\frac{x}{4\pi h} \simeq 2.81$ location. The maximum distortion is obtained at the $\frac{x}{4\pi h} \simeq 2.55$ location, where the maximum value of the distributed force is met. There is only a slight perturbation in terms of temperature (Figure 5.11(b)) or pressure (Figure 5.11(c)). The dashed-line curve on the Figure 5.11(c) shows the corrected pressure by the pressure drop in the channel. The Reynolds Analogy factor $s = \frac{2C_h}{C_f}$ is plotted in Figure 5.11(d). It is nearly constant in the streamise direction except for the distortion region. A maximum value is met where the maximum value of the distributed force was applied.

The instantaneous and mean flow variables are plotted in Figures B.1 and B.2. The flow is locally perturbed: outside the region where the force was applied, all distributions of flow variables are identically to those of the spatially developing channel flow without streamwise adverse pressure gradient. The streamwise velociy and the density are mainly perturbed in the near-wall region, while at the centerline the distortion is bearly visible. The temperature field is less perturbed than the pressure field : at the scale used for the plot, even on the near-wall temperature distribution, it is difficult to see the flow perturbation.

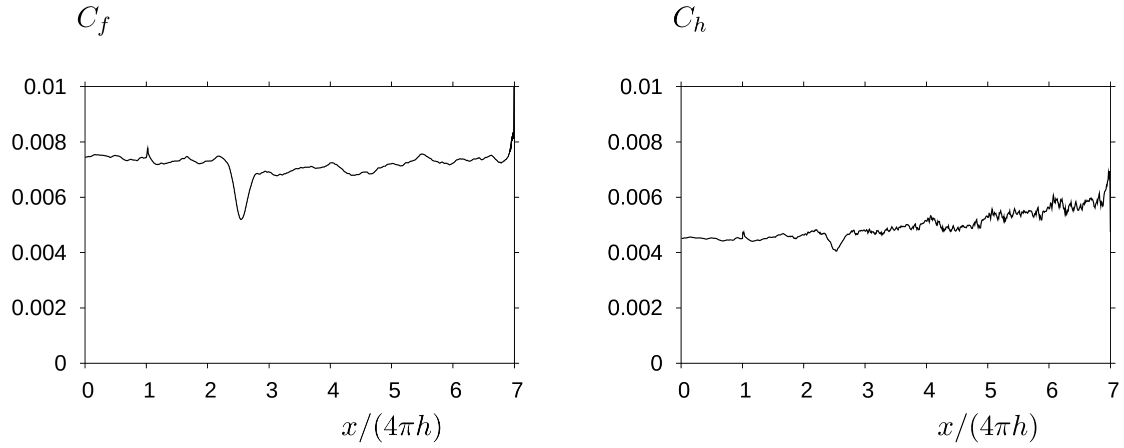

(a) Skin-friction coefficient

(b) Heat-transfer coefficient

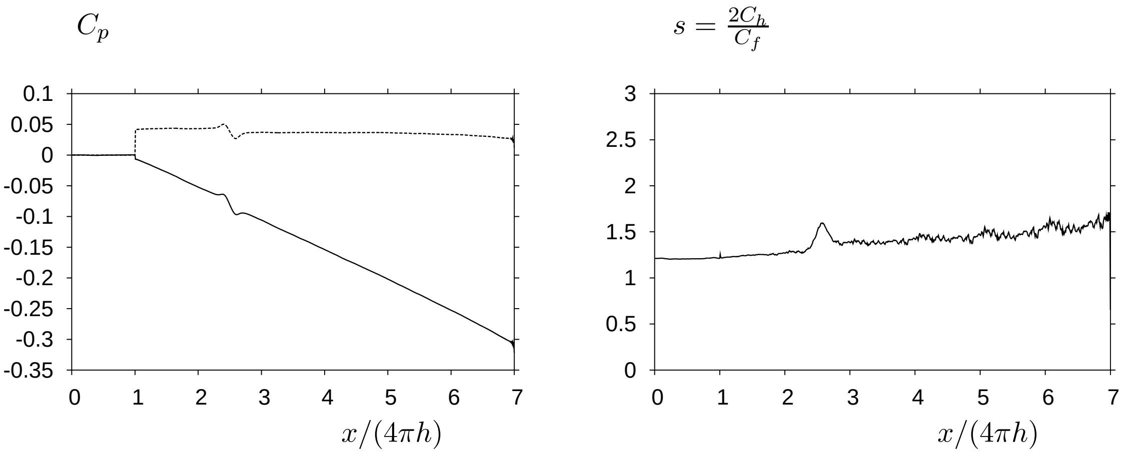

(c) Pressure coefficient

(d) Reynolds Analogy factor

Figure 5.11: **Distribution of skin-friction coefficient (a), heat-transfer coefficient (b), pressure coefficient not corrected ( —— ) and corrected ( - - - ) by the pressure drop (c) and Reynolds Analogy Factor (d).**

Contours of velocities, mean temperature, mean density and mean pressure (Figures B.3 and B.4) show also a weak and local perturbation. In the part of the channel behind the flow perturbation, the flow relaxes back towards steady channel flow.

The mean streamwise velocity isovalues in the distorted channel flow (Figures B.5 and B.6) show that the maximum velocity is met now in the upper part of the channel, instead of at the centerline for the third, fourth and fifth computational boxes. For the next computational boxes, the flow seems to relax back towards the steady behavior.

The behaviour of the instantaneous flowfield was also investigated using the positive Q-criterion isovalues (Figure B.7). Since the local perturbation is weak, no significant modifications in turbulence structure are observed. A growth of large scale structures it is noticed due to deceleration in the distorted region. A bigger thickness of the wall layer can also be observed in this region.

## 5.3 General features

### 5.3.1 Mean profiles

In this section, the adverse streamwise adverse pressure gradient effect on the mean profiles is investigated.

Mean profiles for the fully developed channel ( □ ), spatially developing channel at $\frac{x}{4\pi h} = 2.5$ ( ■ ) and distorted channel at $\frac{x}{4\pi h} \sim 2.55$ ( —— ) are plotted in Figure 5.12. These locations were chosen in order to compare the middle region of the second spatial computational box for simulations with and without streamwise adverse pressure gradient. Here the maximum distributed force value was applied.

As shown also in Figure A.2, in the case of a spatially developing channel flow whithout sreamwise adverse pressure gradient, there is minimal spatial variation in the flow variables except for the pressure and the temperature. It is noticed that the $\frac{\langle \tilde{T} \rangle - T_{wx}}{T_{wx}}$ is a homogeneous quantity in the streamwise direction, where $T_{wx}$ is the wall temperature in the spatial channel (Equation 2.34). Thus, the imposed source distribution used in the incoming fully developed channel flow is validated.

As mentioned, in the case of the distorted channel, the flow is decelerated near the lower wall, while it is accelerated near the opposite wall (Fig. 5.12a). Since the wall-normal velocity is nearly zero everywhere in the channel, the impact of the distortion on it is more important. A change in the wall-normal velocity distribution is observed: values are positive everywhere and an approximately ten-times maximum is obtained at the centreline. The spanwise velocity distribution seems to be completely reversed comparing to the other distributions (fully developed and spatially developing flows). Due to the streamwise adverse pressure gradient, the pressure is diminished on the lower wall and slightly augmented on the opposite wall. Consequently, there is a decrease near the lower wall and then an increase in the temperature distribution. The dynamic viscosity has the same behavior as the temperature because of the power law assumption $\langle \tilde{\mu} \rangle = \mu_w \left( \frac{\langle \tilde{T} \rangle}{T_w} \right)^{0.7}$. The derived Crocco-Busemann type relation for the temperature presents mainly increased values from the vicinity of the lower wall to the opposite wall. The density is increased near the lower wall and then decreased near the opposite wall. The entropy, computed based on the mean pressure and the mean density, has basicaly the same profile as the temperature.

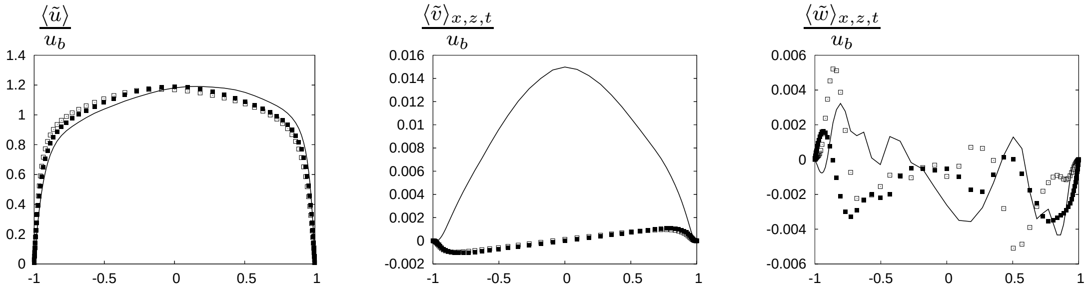

(a) Streamwise velocity

(b) Wall-normal velocity

(c) Spanwise velocity

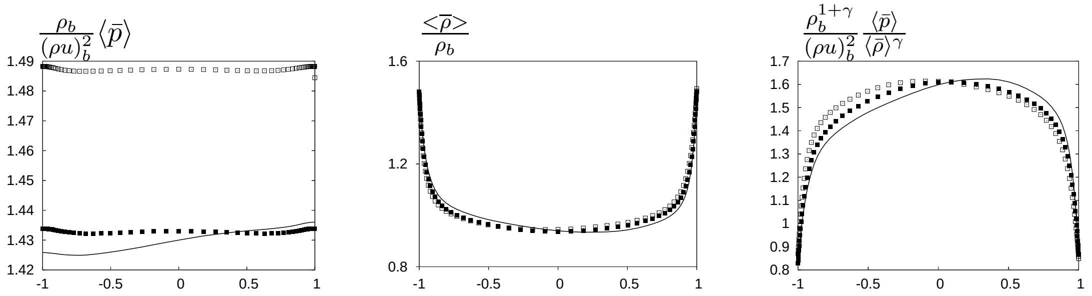

(d) Pressure

(e) Density

(f) Entropy

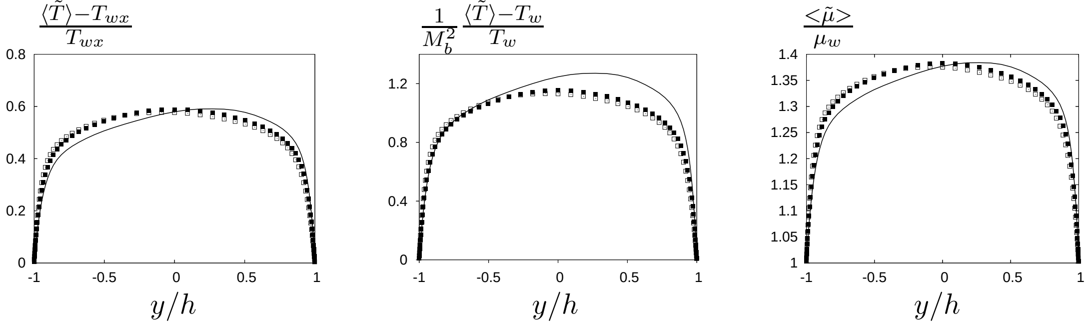

(g) Temperature

(h) Crocco-Bussemann temperature profile

(i) Dynamic viscosity

Figure 5.12: **Comparison between numerical results in fully developed channel ( □ ), second spatial computational box at $\frac{x}{4\pi h} = 2.5$ ( ■ ) and distorted channel at $\frac{x}{4\pi h} \sim 2.55$ ( —— ): profiles of (a) mean streamwise velocity, (b) mean wall-normal velocity, (c) spanwise velocity, (d) mean pressure, (e) mean density, (f) entropy, (g) mean temperature, (h) Crocco-Busemann type relation (4.7), (i) mean dynamic viscosity.**

Figure 5.13 shows mean velocity profiles close to the lower wall at different streamwise stations. The velocity-profile slopes are slightly modified. The flow decelerates upstream the maximum distortion, while accelerating downstream of the maximum distortion. The considered stations are

- in the non-distorted region: $\frac{x}{4\pi h} = 2, 2.03, 2.11, 2.19, 2.23$;

- in the region upstream of the maximum distortion: $\frac{x}{4\pi h} = 2.27, 2.3, 2.34, 2.38, 2.42, 2.46, 2.5, 2.55$;

- in the region downstream of the maximum distortion: $\frac{x}{4\pi h} = 2.55, 2.58, 2.62, 2.66, 2.7, 2.73, 2.77, 2.81, 2.89$;

- and in the recovery region of the flow: $\frac{x}{4\pi h} = 2.97, 3.05, 3.125, 3.2, 3.28, 3.36$.

The results for these stations will be further analysed in the modelling part.

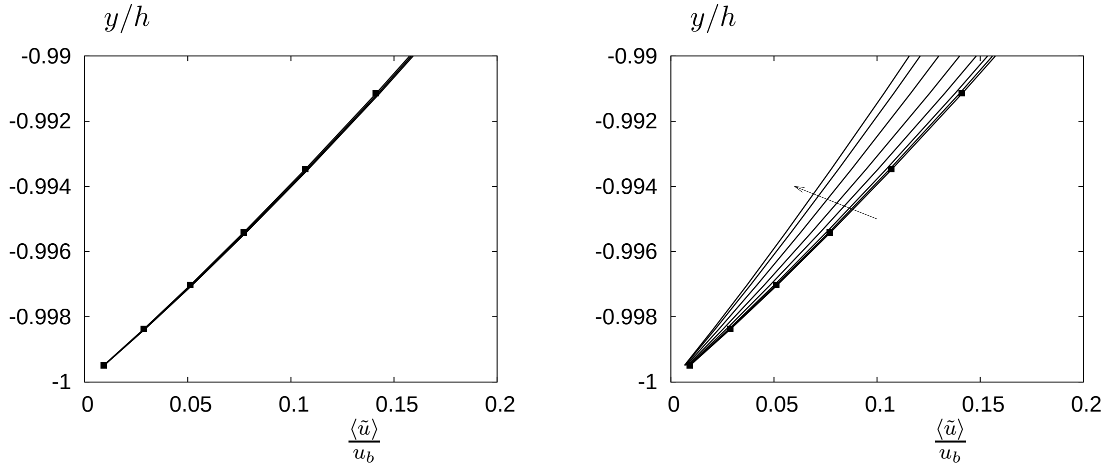

(a) Non-distorted region

(b) Region upstream of maximum distortion

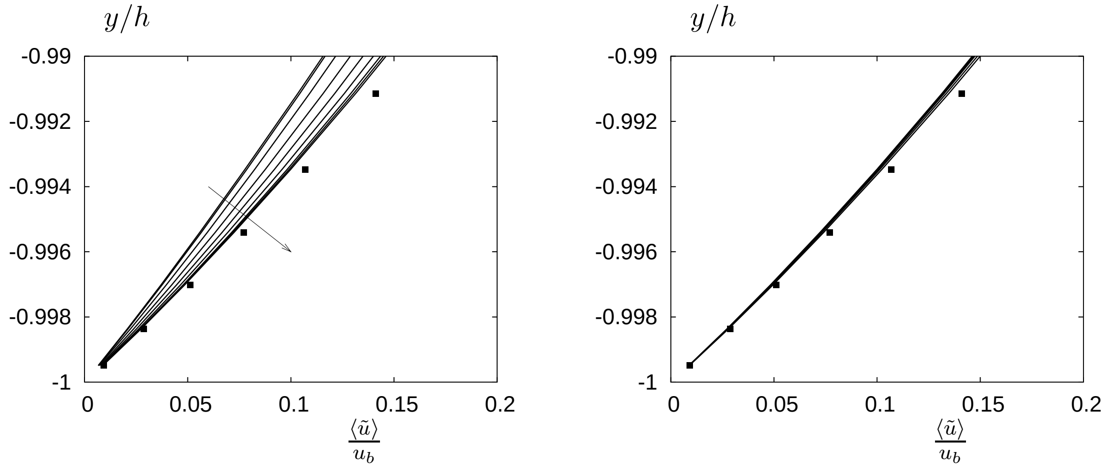

(c) Region downstream of maximum distortion

(d) Region of recovery flow

Figure 5.13: **Velocity profiles above the lower wall of the channel at different streamwise stations: region non-distorted (a), upstream of the maximum distortion (b), downstream of the maximum distortion (c) and of the recovering flow (d). The arrow shows the trend of the profiles in the flow direction.**

### 5.3.2 Anisotropy invariant study

Examination of the anisotropy invariants indicates that the flow anisotropy is weakly affected by the streamwise adverse pressure gradient. Figure 5.14 shows the invariant maps for both simulations, whith and without perturbation. The entire distorted flowfield is plotted on it.

Detailed analysis is carried out for different locations in the distorted flow (Figure 5.15). As the flow approaches maximum distortion (Figure 5.15(a), left) the near-wall turbulence is ressembling the axisymmetric expansion turbulence with the wall flow tending towards one-component turbulence (Figure 5.15(a), right). From the maximum distortion point (Figure 5.15(b), left and 5.15(b), right), both wall and the near-wall turbulence tend back towards the initial turbulence.

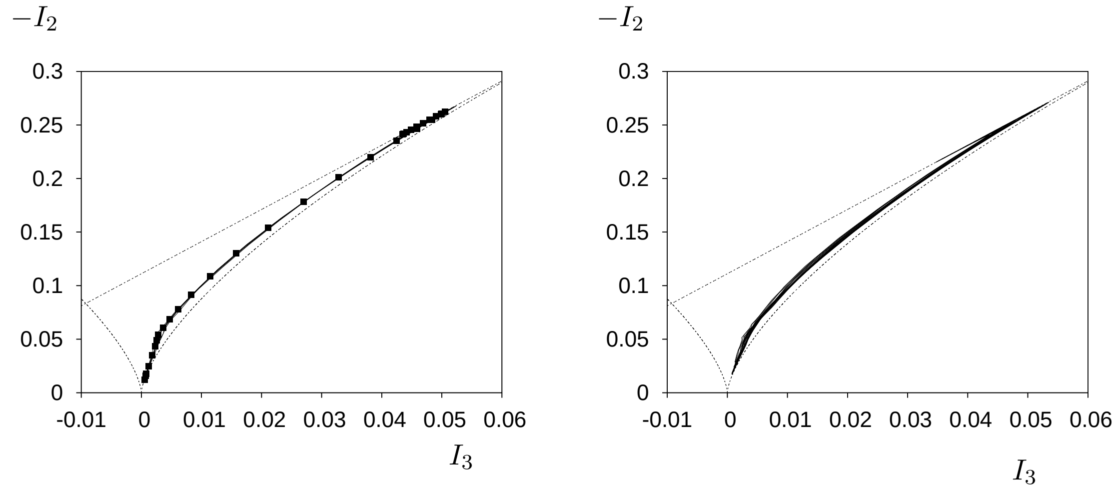

(a) without streamwise adverse pressure gradient

(b) with streamwise adverse pressure gradient

Figure 5.14: **Anisotropy invariant map for $\mathcal{W}_{int}$ source term simulations at $Re = 4880$ & $M = 0.7$ without (a) and with (b) perturbation. The profiles are shown for the near-wall region of the lower wall only. Anisotropy map boundaries ( - - - ).**

### 5.3.3 Modified Strong Reynolds Analogy for the channel (CESRA)

An important point in turbulent compressible flows is the Morkovin's hypothesis. Levels of fluctuating variables for the simulation without streamwise adverse pressure gradient are shown in Figure 5.16. They are in good agreement with those for the fully developed channel flow except for the pressure, which might be due to the pressure drop effect which does not play a role in the periodical case. Nevertheless, the pressure criterion is much better verified than the total temperature condition. The maximum rms pressure values are less than about 0.5% (Figure 5.16(a)) everywhere in the channel, although for the first spatial computational box the level of pressure fluctuations is found larger. Quite large turbulent Mach number is found, especially near the walls (Figure 5.16(c)). The large density and temperature fluctuations are associated with the near-wall $M_t$ (Figures 5.16(e) and 5.16(d), respectively). The entropic mode is not negligible since the maximum rms total temperature values is around 7% (Figure 5.16(b)).

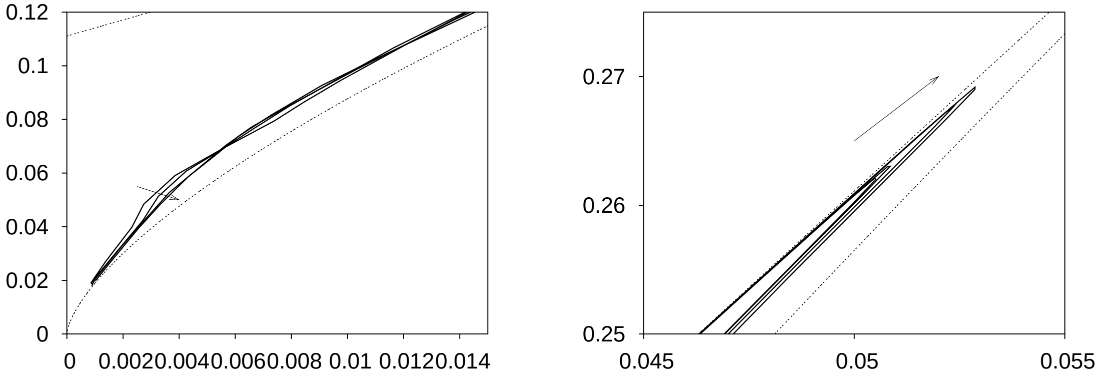

(a) upstream of maximum distortion

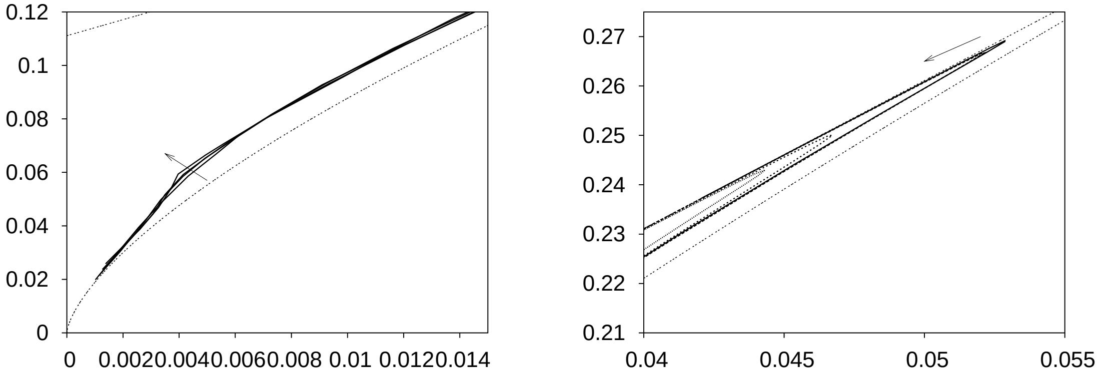

(b) downstream of maximum distortion

Figure 5.15: **Zoom of the anisotropy map ( —— ) upstream of maximum distortion (a) and downstream of maximum distortion (b). The arrow shows the trend of the profiles in the flow direction. Anisotropy map boundaries ( - - - ).**

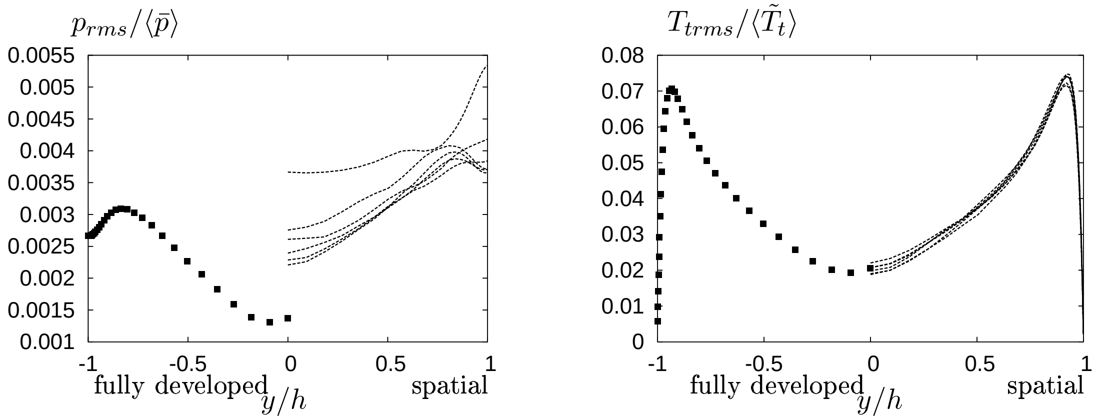

(a) Pressure

(b) Total temperature

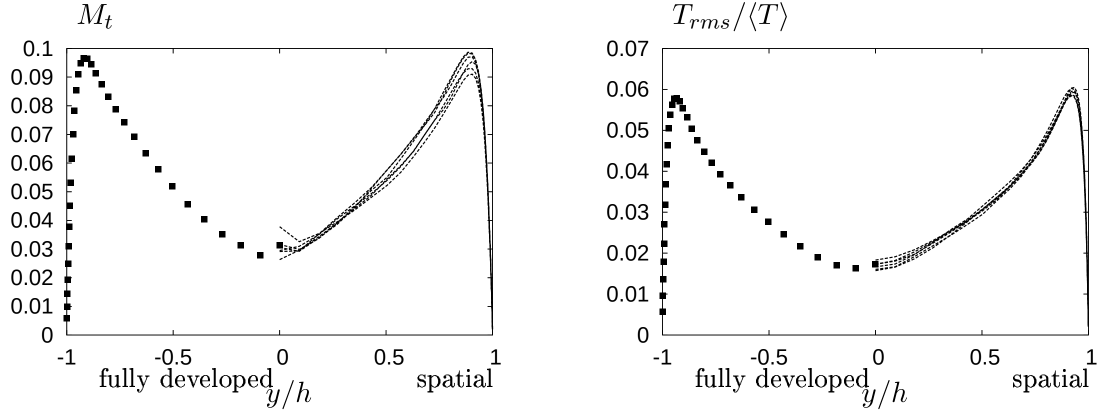

(c) $M_t = \frac{\sqrt{u_{rms}^2+v_{rms}^2+w_{rms}^2}}{\gamma R\langle\tilde{T}\rangle}$

(d) Temperature

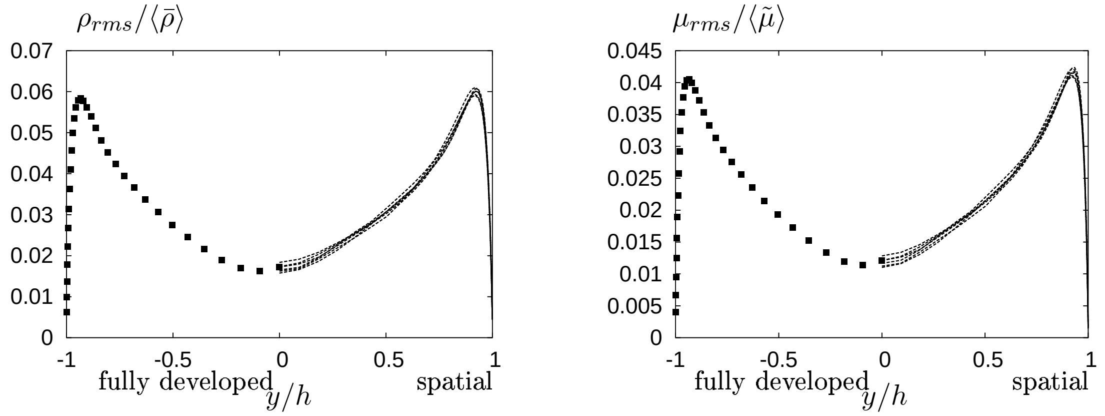

(e) Density

(f) Viscosity

Figure 5.16: **Spatial channel: pressure fluctuations (a), total temperature fluctuations (b), turbulent Mach number (c), temperature fluctuations (d), density fluctuations (e) and viscosity fluctuations (f): fully developed channel ( ■ ) and spatial computational boxes ( —— ).**

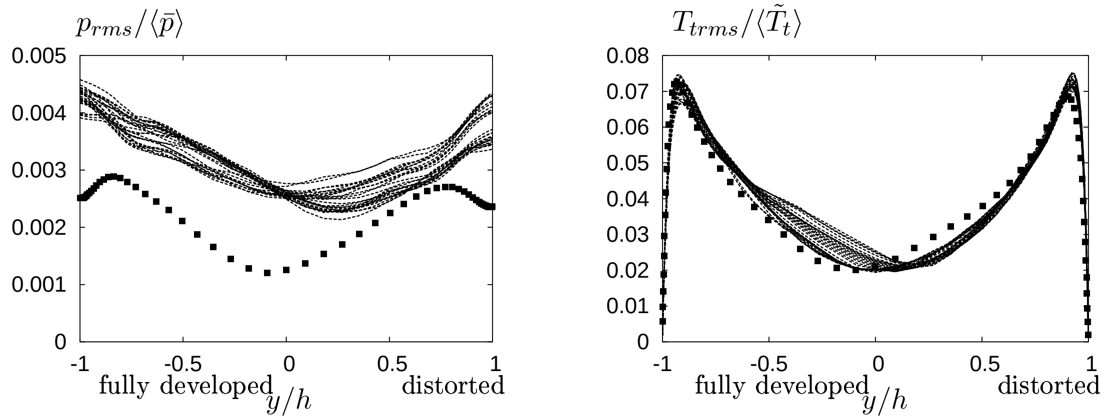

(a) Pressure

(b) Total temperature

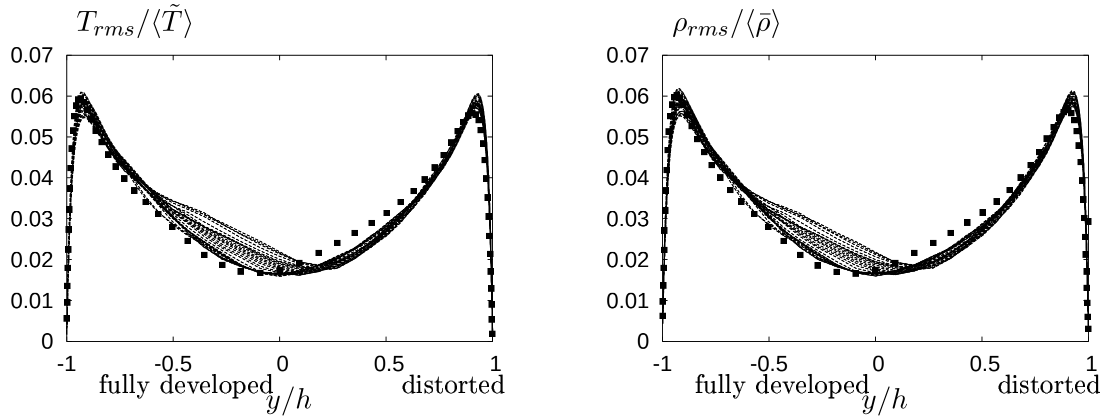

(c) Temperature

(d) Density

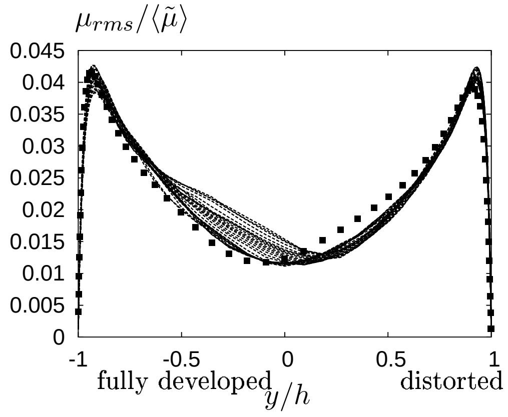

(e) Viscosity

Figure 5.17: **Distorted channel: pressure fluctuations (a), total temperature fluctuations (b), temperature fluctuations (c), density fluctuations (d) and viscosity fluctuations (e): fully developed channel ( ■ ) and spatial computational boxes ( —— ).**

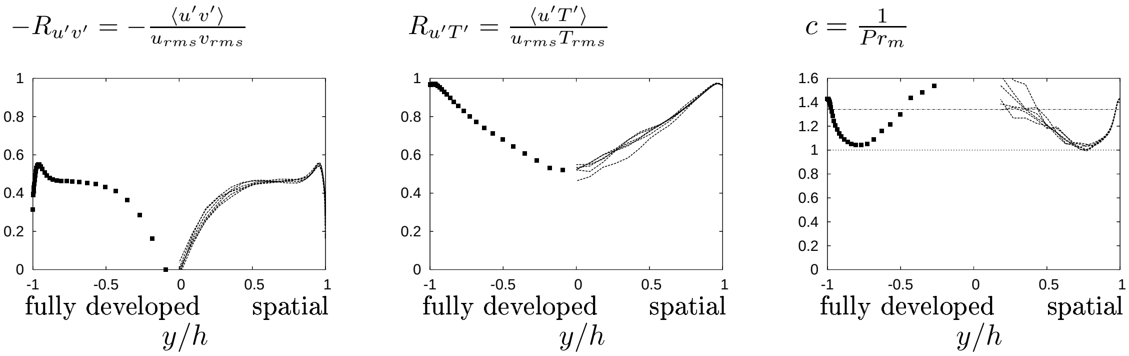

(a) uv correlation (b) ut correlation (c) MSRA $c$ coefficient

Figure 5.18: **Spatial channel: correlation coefficient for the Reynolds stress tensor (a), correlation coefficient for the turbulent heat flux (b) and MSRA $c$ coefficient: fully developed channel ( ■ ) and spatial computational boxes ( —— ).**

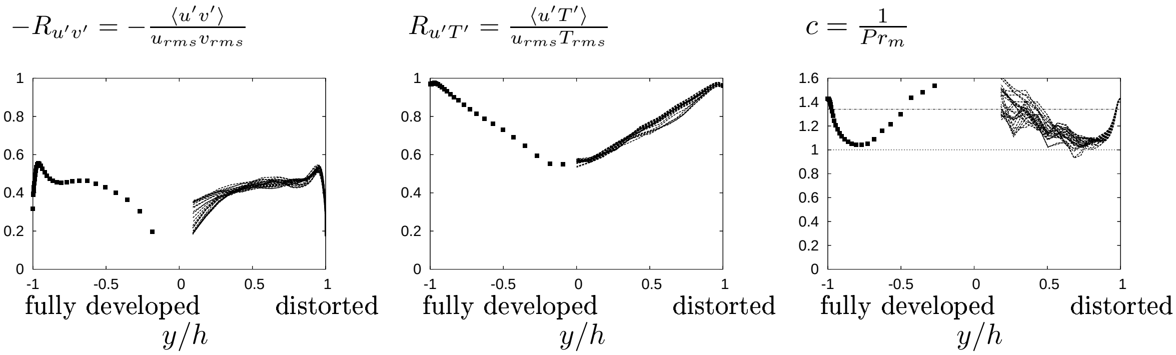

(a) uv correlation (b) ut correlation (c) MSRA $c$ coefficient

Figure 5.19: **Distorted channel: correlation coefficient for the Reynolds stress tensor (a), correlation coefficient for the turbulent heat flux (b) and MSRA $c$ coefficient: fully developed channel ( ■ ) and spatial computational boxes ( —— ).**

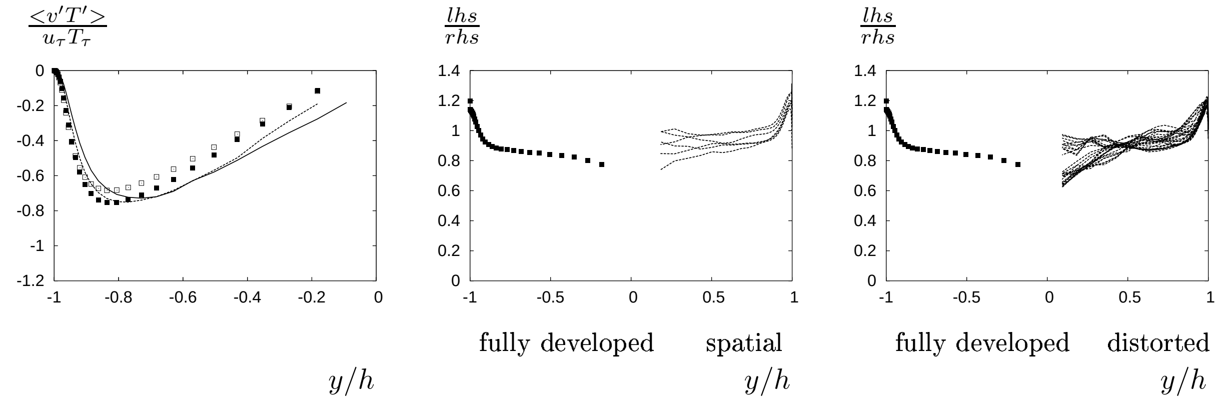

(a) Equation 4.38

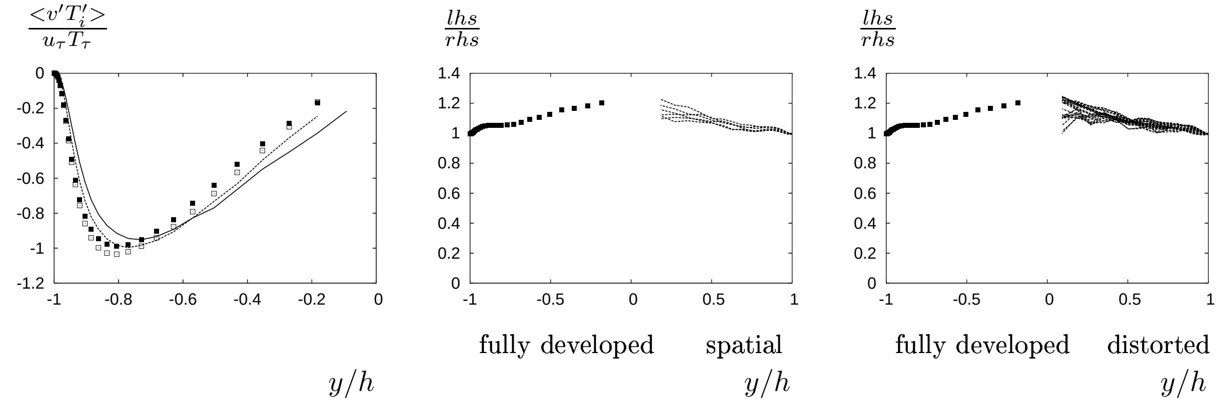

(b) Equation 4.40

Figure 5.20: **Temperature (a) and total temperature streamwise velocity correlation (b). Left: CESRA Analogy ( □ ), direct computation: fully developed channel flow ( ■ ), spatially developed channel flow at** $\frac{x}{4\pi h} = 2.5$ **( - - - ) and distorted channel flow at** $\frac{x}{4\pi h} \sim 2.55$ **( —— ). Right: fully developed channel ( ■ ) and spatial computational boxes ( —— ).**

Levels of flow variables fluctuations for the simulation with streamwise adverse pressure gradient are shown in Figure 5.17. The distortion being local and weak, the fluctuations levels are basically the same as for the spatially developing or for the fully developed channel flows in the near-wall region. Contrary, in the core of the channel larger levels are found. With maximum rms pressure values less than about 0.5% (Figure 5.17(a)) everywhere in the channel, the acoustic criterion is better verified than the entropic condition. The latter is not negligible, the maximum rms total temperature being around 7.5%.

As presented in the Section 4.7, a positive correlation between streamwise velocity fluctuations and temperature fluctuations is found in the buffer region layer (Figures 5.18 and 5.19). It is noticed that the shear stress correlation and the MSRA $c$ coefficient seem to be much sensitive to the distorsion.

The derived MSRA relations for the channel flows (4.38) and (4.40) are successfully applied for both compressible flows, with and without streamwise pressure gradient (Figures 5.20 and **??**, respectively). This allows us to conclude that the modified strong Reynolds analogy developed for the channel is valid whichever source term or channel configuration is used.

## 5.4 Summary

In this chapter first a model of the turbulent compressible flow developing spatially was validated. Inflow and outflow conditions were checked in terms of instantaneous and mean variables. The streamwise development of these variables indicates differences between naturally developing and periodic channel flow. A main result is the homogeneity of the quantity $\frac{\langle\tilde{T}\rangle - T_{wx}}{T_{wx}}$. Thus, the hypothesis made to derive the $\mathcal{W}_{int}$ source term used to model the pressure drop in a fully developed channel flow is validated.

Next, a body forcing method of obtaining a turbulent incompressible bubble [32] has been extended to a compressible turbulent flow. The simulation was shown to generate a weak and local distorted region in the flow where the distributed force was applied. The flow near the the lower surface was investigated using anisotropy invariants and instantaneous visualization. Correlations between velocity and temperature fluctuations were examined using the modified strong Reynolds analogy for the channel (CESRA). The shear stress correlation, MSRA $c$ coefficient, heat and total temperature fluxes were found to be more sensitive to the distortion.

Data from the simulations investigated in this chapter will be used as a reference for the modelling work in Chapters 7 and 8.

# Part III

# MODELLING RESULTS

# CHAPTER 6

# Wall layer description

Based on the mean velocity profile, the flow is usually divided into three regions. These are, starting from the wall: the inner, buffer and outer layers. In the outer layer the viscosity effects are negligible, as shown in Figures 6.1-6.3(a). Large scales are found and they are well resolved using Large Eddy Simulations. In the inner layer, the region closest to the wall, the effects of viscosity cannot be neglected and play an important role in the behavior of the wall layer (for example, in a separated wall layer). In this layer the small scales are predominant and LES is less efficient in simulating them. The buffer layer is the intermediate region between the inner and the outer layers.

Figures 6.1-6.3 describe fully developed flow and spatially developing flow with and without streamwise adverse pressure gradient in terms of turbulent viscosity and turbulent conductivity, turbulent Prandtl number and mixed Prandtl number, for all source terms and various Reynolds and Mach numbers (see Table 6.1). These are the needed quantities for modelling. In the near-wall region, all these quantities have the same behavior whichever source term or flow configuration is considered. Here, as mentioned above, the viscosity effects are dominant. This attribute of the wall-bounded flow will be used in what follows for the modelling developments.

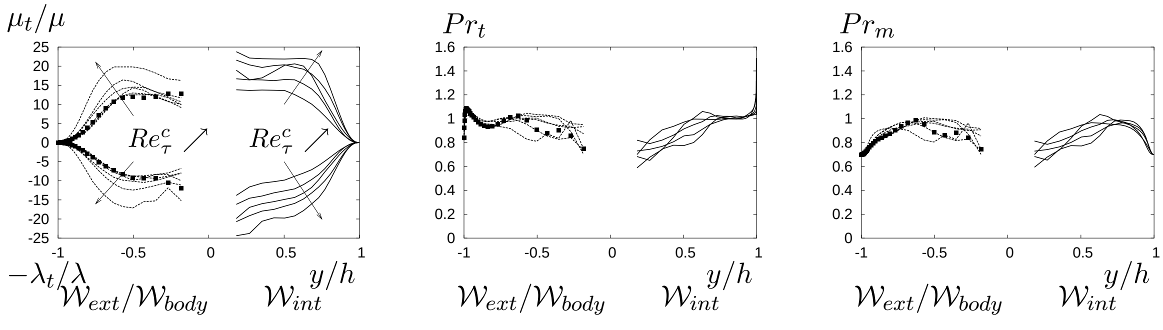

(a) Viscous versus turbulent viscosity/conductivity

(b) Turbulent Prandtl number

(c) Mixed Prandtl number

Figure 6.1: **Viscous versus turbulent viscosity/conductivity (a), turbulent Prandtl number (b), mixed Prandtl number (c), for fully developed channel flow simulations with $\mathcal{W}_{body}$ ( - - - ), $\mathcal{W}_{ext}$ ( ■ ) and $\mathcal{W}_{int}$ ( —— ).**

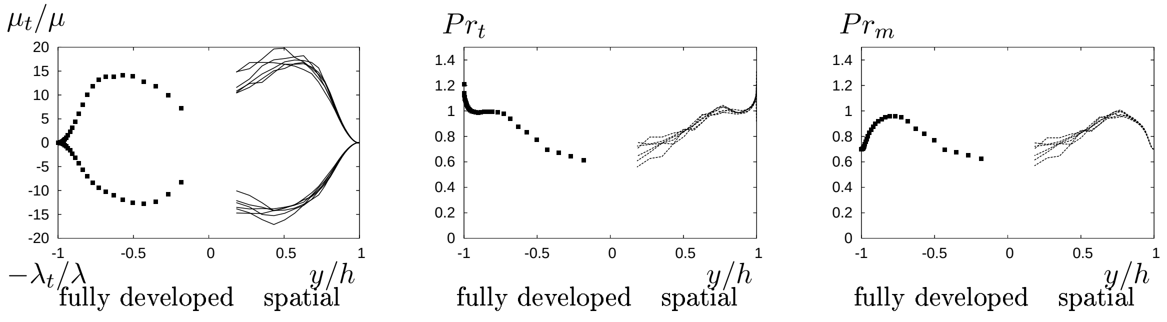

(a) Viscous versus turbulent viscosity/conductivity

(b) Turbulent Prandtl number

(c) Mixed Prandtl number

Figure 6.2: **Viscous versus turbulent viscosity/conductivity (a), turbulent Prandtl number (b), mixed Prandtl number (c), for spatially developed channel flow simulations with $\mathcal{W}_{int}$, $Re = 4880$ and $M = 0.7$: fully developed channel flow ( ■ ) and spatial computational box ( —— ).**

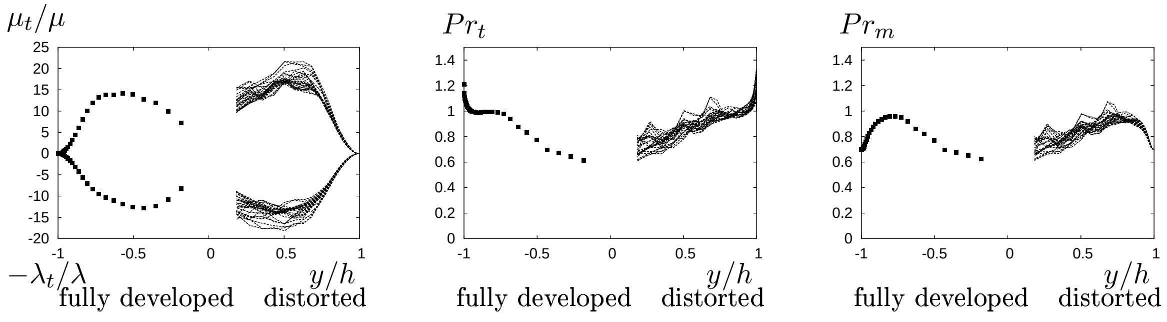

(a) Viscous versus turbulent viscosity/conductivity

(b) Turbulent Prandtl number

(c) Mixed Prandtl number

Figure 6.3: **Viscous versus turbulent viscosity/conductivity (a), turbulent Prandtl number (b), mixed Prandtl number (c), for distorted channel flow simulations with $\mathcal{W}_{int}$, $Re = 4880$ and $M = 0.7$: fully developed channel flow ( ■ ) and spatial computational box ( —— ).**

| Source | Mach | Reynolds | $Re_\tau$ | $Re_\nu$[6] | $Re_{sl}$[34] | $Re^c_\tau$ | $\lambda^+_z$ | $\lambda^{c+}_z$ | $\Delta y^+_w$ | $\Delta y^{c+}_w$ |
|---|---|---|---|---|---|---|---|---|---|---|
|  | 0 | Kim *et al.*[43] | 180 | 180 | 180 | 180 | 100 | 100 | 0.05 | 0.05 |
| $\mathcal{W}_{int}$ | 0.3 | 3000 | 193 | 108 | 171 | **182** | – | – | 0.10 | 0.10 |
|  | 1 |  | 280 | 69 | 105 | 169 | – | – | 0.14 | 0.14 |
|  | 1.5 |  | 385 | 35 | 71 | 161 | – | – | 0.20 | 0.19 |
| $\mathcal{W}_{body}$ | 0.3 | 3000 | 188 | 182 | 184 | **185** | 128 | 127 | 0.10 | 0.10 |
|  | 1 |  | 203 | 153 | 166 | **182** | 145 | 130 | 0.10 | 0.10 |
|  | 1.5 |  | 219 | 122 | 145 | 175 | 170 | 137 | 0.11 | 0.11 |
|  | 2 |  | 241 | 96 | 126 | 169 | 190 | 134 | 0.12 | 0.12 |
|  | 1.5 | Coleman *et al.*[14] | 222 |  | ≈ **151** |  | 150 | ≈ 130 | 0.1 | 0.1 |
| $\mathcal{W}_{int}$ | 0.3 | 4880 | 297 | 252 | 264 | **280** | – | – | 0.15 | 0.15 |
|  | 0.7 |  | 368 | 168 | 211 | **277** | – | – | 0.19 | 0.19 |
|  | 1 |  | 440 | 111 | 167 | 267 | – | – | 0.22 | 0.22 |
|  | 1.5 |  | 578 | 54 | 109 | **241** | – | – | 0.29 | 0.29 |
|  | 3 |  | 1010 | 6 | 27 | 166 | – | – | 0.51 | 0.50 |
| $\mathcal{W}_{body}$ | 1 | 4880 | 310 | 231 | 252 | **278** | 180 | 160 | 0.16 | 0.16 |
|  | 3 |  | 459 | 86 | 141 | **240** | – | – | 0.23 | 0.23 |
|  | 3 | Coleman *et al.*[14] | 451 |  | ≈ **150** |  | 300 | ≈ 160 | 0.2 | 0.2 |
| $\mathcal{W}_{ext}$ | 3 | 4880 | 462 | 83 | 138 | **238** | 315 | 165 | 0.23 | 0.23 |

Table 6.1: **Characteristics of the simulations. Comparisons are made with the DNS of Kim *et al.* [43] for $M = 0.0$ and Coleman *et al.* [14] for $M = 1.5$ and $M = 3.0$. Reynolds number cases in bold will be further compared.**

In order to achieve a reliable simulation of the inner layer several solutions exist, among them,

- refinement of the grid near the wall in order to catch smaller eddies. In this case, the simulation reaches a level close to DNS with the consequence of increasing calculation and time costs;
- modelling of the inner layer and computing the outer layer only. Then the first grid point can be further away from the wall in comparison with a DNS and the simulation uses a coarser grid over the whole domain. This solution is the most economical way to run an LES of a wall-bounded flow, but wall models must be used;
- simulations combining a RANS-type near wall model and an LES model: to resolve the outer part, LES is applied and the RANS model is used to treat the near-wall region.

The state-of-the-art in wall-layer models has been summarized by *Piomelli* & *Balaras* [67] as follows:

- simple models which work fairly well in simple flows (for example, the logarithmic law in terms of prediction of mean skin-friction coefficient and outer velocity profile or for the evaluation of the Reynolds stresses outside a transition layer);
- zonal models for more complex configurations (for example, backward-facing step and the airfoil trailing edge);
- no extensive tests of wall-layer models in complex configurations exist (for example, three-dimensional shear-driven boundary layer).

For wall-bounded compressible flows, two wall layers exist: the velocity wall layer and the thermal wall layer characterized by a steep transverse temperature gradient.

The relation relating the thickness of the velocity wall layer, $\delta$ and the thickness of the thermal wall layer, $\delta_T$ is

$$\frac{\delta_T}{\delta} \sim \frac{1}{\sqrt{Pr}}$$

. Therefore, the thermal wall layer in a gas may be expected to be approximately of the same order of magnitude as the velocity wall layer, whereas for liquids it is smaller.

First consider the averaged Navier-Stokes equations written for a statistically 2D compressible stationary flow in a channel (including Equations 2.29 and 3.11). For relatively low Mach numbers, at least non-hypersonic cases [6], we showed that Favre and Reynolds averaging were not much different (see Section 4.4). Therefore we neglect density (and viscosity) fluctuations and end up with the relations for streamwise momentum transport and total energy:

$$0 = -\frac{\partial\langle\bar{p}\rangle}{\partial x} + \frac{\partial}{\partial y}\left[(\langle\tilde{\mu}\rangle + \mu_t)\frac{\partial\langle\tilde{u}\rangle}{\partial y}\right] \tag{6.1}$$

$$0 = -\frac{\gamma}{\gamma-1}\langle\tilde{u}\rangle\frac{\partial\langle\bar{p}\rangle}{\partial x} + \frac{\partial}{\partial y}\left[(\langle\tilde{\lambda}\rangle + \lambda_t)\frac{\partial\langle\tilde{T}_i\rangle}{\partial y}\right] \tag{6.2}$$

where the Reynolds stress and the turbulent heat flux are classically related to the mean velocity and mean temperature gradients, based on turbulent viscosity $\mu_t$ and turbulent diffusivity $\lambda_t$

$$-\langle\bar{\rho}\rangle\langle u'v'\rangle = \mu_t\frac{\partial\langle\tilde{u}\rangle}{\partial y} \tag{6.3}$$

$$\langle\bar{\rho}\rangle C_p\langle T'v'\rangle = \lambda_t\frac{\partial\langle\tilde{T}\rangle}{\partial y} \tag{6.4}$$

The term involving kinetic energy has been considered negligible since the Prandtl number is $Pr = 0.7$ and the turbulent Prandtl and the mixed Prandtl numbers are around 1 in the near-wall region.

Turbulent and viscous contributions are blended in the mixed Prandtl number (Equation 4.19), which is either equal to the Prandtl number $Pr = 0.7$ at the wall or to the turbulent Prandtl number $Pr_t = \frac{\mu_t C_p}{\lambda_t}$ in the turbulent region, with $0.8 \le Pr_t \le 1.05$ (Figures 6.1b,c-6.3b,c).

These relations are used in what follows to obtain the wall-layer laws for the streamwise velocity and temperature.

# CHAPTER 7

# Modelling of an attached wall layer

In this chapter classical laws of the wall for both the velocity and the total temperature are presented. Then, an improvement of the van Driest transformation is proposed which accounts for both density and viscosity changes in the wall layer. Consistently, a new integral wall scaling which accounts for strong temperature gradients at the wall is developed for the present non-adiabatic compressible flows and rms scaling is investigated. The chapter ends with a brief summary.

## 7.1 Wall unit for attached compressible wall layers

In the viscous sublayer near the wall, the turbulent stresses and heat fluxes are negligible in (6.1) and (6.2) as shown in Figure 6.1a. The flow properties can be used as weighting factor to define an integral velocity and an integral total temperature [6, 11, 17, 33, 59] which fit the classical linear laws, respectively:

$$I_1^+ = \int_0^{\langle\tilde{u}\rangle^+} \frac{\langle\tilde{\mu}(\tilde{T})\rangle}{\mu_w} d\langle\tilde{u}\rangle^+ = y^+ \tag{7.1}$$

$$I_2^+ - T_w^+ = \int_{T_w^+}^{\langle\tilde{T}_i\rangle^+} \frac{\langle\tilde{\mu}(\tilde{T})\rangle}{\mu_w} d\langle\tilde{T}_i\rangle^+ = Pr\ y^+ \tag{7.2}$$

where $u^+ = u/u_\tau$, $T_i^+ = T_i/T_\tau$, the $^+$ superscript being referred to the usual wall unit involving a friction velocity and a friction temperature, based on wall friction $\tau_w$ and wall heat flux $q_w$ for compressible flows (Equations 3.1 and 3.2). A similar transformation is presently proposed [7, 31] to define rather an integral lengthscale $y^{c+}$ which is equivalent to the standard $y^+$ wall unit in the asymptotic incompressible case ($\langle\tilde{\mu}\rangle = \mu_w$),

$$y^{c+} = \int_0^{y^+} \frac{\mu_w}{\langle\tilde{\mu}(\tilde{T})\rangle} dy^+ \tag{7.3}$$

Equations (7.1) and (7.2) then become

$$\langle\tilde{u}\rangle^+ = y^{c+} \tag{7.4}$$

$$\langle\tilde{T}_i\rangle^+ - T_w^+ = \left(\langle\tilde{T}\rangle^+ - T_w^+\right) + \frac{\gamma-1}{2} Pr\ M_\tau^{c2}\ \langle\tilde{u}\rangle^{+2} = Pr\ y^{c+} \tag{7.5}$$

which is conform with the expected linear law at the wall for both the velocity and the total temperature, and accounts for near wall temperature variations in an alternative way to the existing compressible scaling [6, 34, 48]. For the present channel flow, the resulting integral Reynolds number

$$Re_\tau^c = h^{c+} = \int_0^{h^+} \frac{\mu_w}{\langle \tilde{\mu}(\tilde{T}) \rangle} dy^+ \tag{7.6}$$

has the expected decaying behavior for increasing Mach number, *e.g.* $Re_\tau^c = 238$ for $[M = 3, Re = 4880, \mathcal{W}_{ext}]$ and $Re_\tau^c = 267$ for $[M = 1, Re = 4880, \mathcal{W}_{int}]$, in contrast with the standard friction Reynolds number $Re_\tau = h^+$ (table 6.1). The present integral lengthscale is very practical since it may be used to build a realistic friction Reynolds number for compressible boundary layers $Re_\delta^c = \delta^{c+}$ similar to the one proposed by Bradshaw [6] $Re_\nu = \sqrt{\frac{\rho_w}{\rho_e}} \frac{u_\tau \delta}{\nu_e}$ or the semi local-scaling from Huang et *al.* [34] $Re_{sl} = \frac{\rho_e u_\tau^e \delta}{\mu_e}$. All these Reynolds number definitions account for the flow properties and yield for increasing Mach number the same decaying tendency, which fits the qualitative behavior described on the visualizations in the Section 4.2. What is specific to the present integral scaling is that it is analytically derived from Navier-Stokes equations, and not from an order of magnitude analysis, which is the case in previous scaling proposals, and therefore constitutes a theoretical improvement. A quantification of the relation between the integral and semi-local scalings can be obtained as well analytically, $dy^* = \frac{\rho_b}{\rho_w} \frac{\mu(\tilde{T})}{\mu_b} dy^{c+}$, where $\mu(\tilde{T})$ is strongly increasing from the wall to the center of the channel for the present isothermal-wall case. A quantitative comparison of the two scalings is done in Figure 7.1 and 7.2 and shows a similar trend for both, although the integral behavior increases consequently the wall gradient effects in the present formulation. A quantitative measure of the difference of the two procedures can be performed based on the normalised half-width of the channel $h^* = Re_{sl} = 141$ with the semi-local scaling and $h^{c+} = Re_\tau^c = 240$ with the integral scaling, for the case $Re = 4880, M = 3$ (Table 6.1). Notice that the integral scaling yields values which are qualitatively closer to what we expect for incompressible reference channel flow in the sense that one should worry about friction Reynolds number values lower than 150 for fully turbulent cases. It is even more critical with the definition given by Bradshaw which predicts for the present flow case $Re_\nu = 86$. It is finally interesting to note that assuming a constant temperature $\tilde{T} = T_0 \in [T_w; T_b]$ such as $\rho_b \mu(T_0) = \rho_w \mu_b$, the semi-local scaling can be considered as a simplified form of the integral scaling and thus is worth using for engineering applications, since an integral function is no longer necessary.

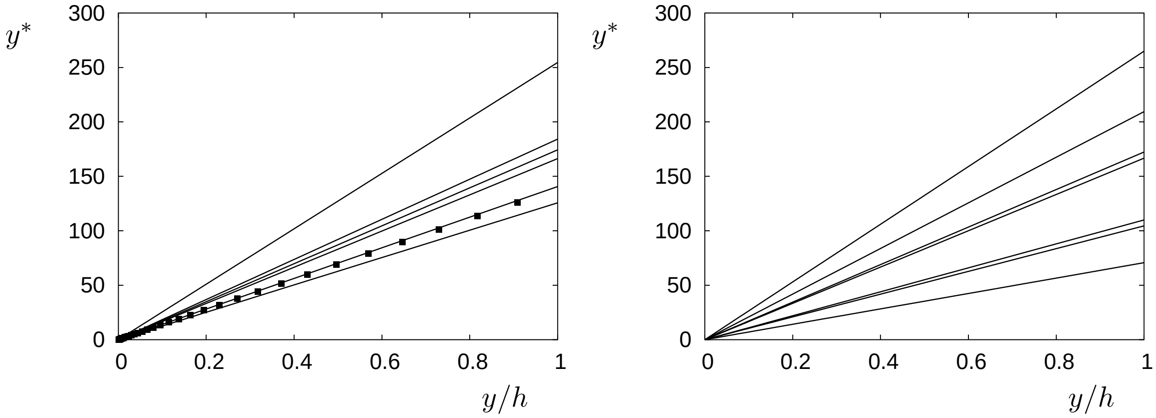

(a) $\mathcal{W}_{ext}$ and $\mathcal{W}_{body}$

(b) $\mathcal{W}_{int}$

Figure 7.1: **Semi-local wall unit for (a) $\mathcal{W}_{body}$ ( - - - ) and $\mathcal{W}_{ext}$ ( ■ ) and (b) $\mathcal{W}_{int}$.**

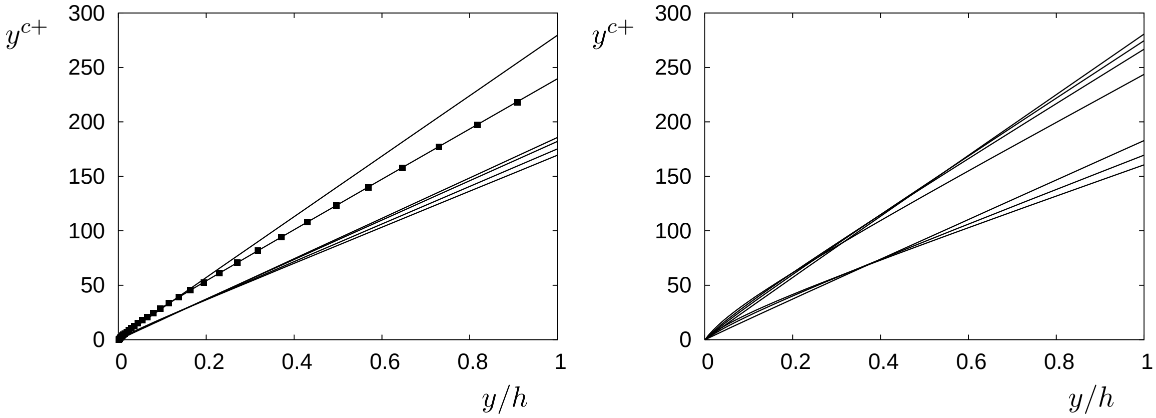

(a) $\mathcal{W}_{ext}$ and $\mathcal{W}_{body}$

(b) $\mathcal{W}_{int}$

Figure 7.2: **Present integral wall unit for (a) $\mathcal{W}_{body}$ ( - - - ) and $\mathcal{W}_{ext}$ ( ■ ) and (b) $\mathcal{W}_{int}$.**

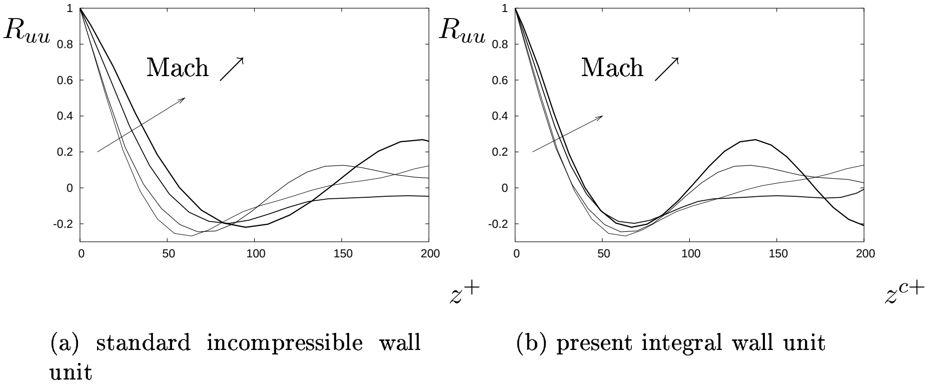

(a) standard incompressible wall unit

(b) present integral wall unit

Figure 7.3: **Spanwise correlation of the streamwise velocity in the near wall region** $y^{c+} = 2.5$ **for a compressible channel flow:** $0.3 \leq M \leq 2$, $Re = 3000$, $\mathcal{W}_{body}$.

On Figure (7.3) we show the transverse correlation of the streamwise velocity $R_{uu}$ near the wall at $y^{c+} = 2.5$. The first minimum indicates half the spanwise wavelength of the streaks, $\lambda_z^+ \simeq 2z^+(R_{uu}min)$. With the standard incompressible wall scaling the width of the streaks $\lambda_z^+$ increases with Mach number, for constant Reynolds number (Table 3.2). Once the present temperature correction is applied, the spanwise wavelength of the streaks remains nearly constant, about $\lambda_z^{c+} \approx 130$ for $Re = 3000$ and $\lambda_z^{c+} \approx 160$ for $Re = 4880$. Furthermore, the integral lengthscale which represents the surface below the correlation profile is constant (Figure 7.3). This is a strong argument for turbulence universality in compressible boundary layers in the sense of Bradshaw[6]: *' The Mach number invariance of the integral lengthscale is our most conclusive check on Morkovin's hypothesis at present.'*

## 7.2 Improvement of the van Driest transformation

For compressible flows, velocity and temperature profiles do not fit the incompressible laws of the wall because of the changes in flow properties described in the chapters above.

Above the buffer layer, viscous terms are negligible with respect to the turbulent stresses $\langle\tilde{\mu}\rangle \ll \mu_t$ and $\langle\tilde{\lambda}\rangle \ll \lambda_t$ (Figure 6.1a). In the present intermediate Reynolds number case, under this assumption and neglecting the streamwise pressure gradient correction on the law of the wall, Equations 6.1 and 6.2 write

$$\mu_t \frac{\partial\langle\tilde{u}\rangle}{\partial y} = \tau_w \left(1 - \frac{y}{h}\right) \tag{7.7}$$

$$\lambda_t \frac{\partial\langle\tilde{T}_i\rangle}{\partial y} = -q_w \left(1 - \frac{u_{by}}{u_b}\frac{y}{h}\right) \tag{7.8}$$

with $\int_0^y \langle\tilde{u}\rangle(y)dy = u_{by}y$.

Equations 7.7 and 7.8 are recast using the mixing length theory $\mu_t = \langle\bar{\rho}\rangle(\kappa y)^2 \frac{\partial\langle\tilde{u}\rangle}{\partial y}$ with

$\kappa = 0.41$ [6, 31] and express in the standard wall unit,

$$d\langle\tilde{u}\rangle^+ = \sqrt{\frac{\rho_w}{\langle\bar{\rho}\rangle}}\frac{1}{\kappa\ y^+}dy^+ \tag{7.9}$$

$$d\langle\tilde{T}_i\rangle^+ = \sqrt{\frac{\rho_w}{\langle\bar{\rho}\rangle}}\frac{Pr_t}{\kappa\ y^+}dy^+ \tag{7.10}$$

The van Driest transformation [6, 33] consists in correcting the velocity and temperature variations in the boundary layer based on changes in density. A logarithmic law which fits relatively well the incompressible boundary layer profile (Figures 7.4a and 7.5a) is obtained for both the transformed velocity [6, 14] and the total temperature [11, 17], whatever source term is considered to model the flow in a compressible channel,

$$\langle\tilde{u}\rangle^+_{VD} = \int_0^{\langle\tilde{u}\rangle^+}\sqrt{\frac{\langle\bar{\rho}\rangle}{\rho_w}}d\langle\tilde{u}\rangle^+ = \frac{1}{\kappa}\ ln\ y^+ + C \tag{7.11}$$

$$\langle\tilde{T}_i\rangle^+_{CDS} - T^+_w = \int_{T_w}^{\langle\tilde{T}_i\rangle^+}\frac{1}{Pr_t}\sqrt{\frac{\langle\bar{\rho}\rangle}{\rho_w}}d\langle\tilde{T}_i\rangle^+ = \frac{1}{\kappa}\ ln\ y^+ + C_3 \tag{7.12}$$

where the subscript $CDS$ refers to the transposition of the VD transformation to the total temperature by Carvin *et al.*[11, 17].

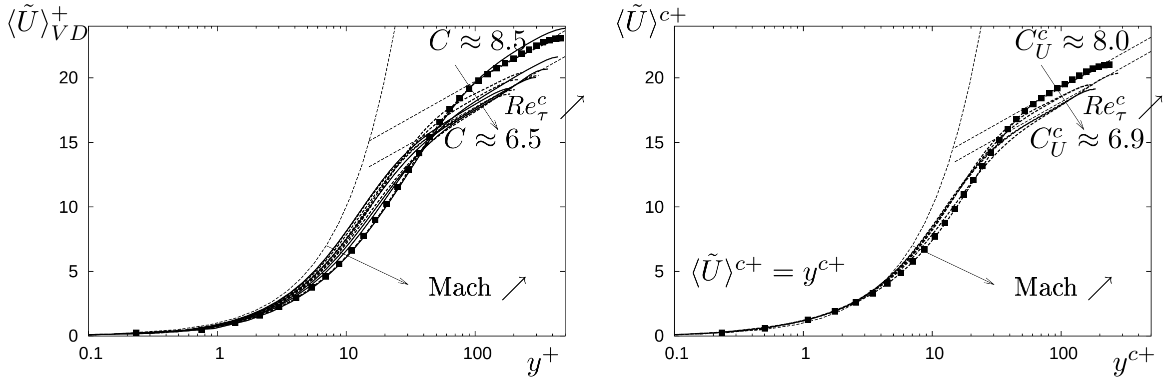

(a) VD transformation

(b) present integral transformation

Figure 7.4: **Mean velocity profiles in a compressible channel at** $Re = 3000$ **and** $Re = 4880$**, for** $\mathcal{W}_{body}$ **( - - - ),** $\mathcal{W}_{ext}$ **( ■ ) and** $\mathcal{W}_{int}$ **( —— ).** $0.3 \leq M \leq 2$.

Looking in more details, the buffer layer thickness is strongly Mach number dependent, a drawback that we relate to the viscosity changes in the near wall region which are not accounted for in the definition of $y^+$. The present integral scaling $y^{c+}$ is considered in order to improve the van Driest transformation, accounting for both $\langle\bar{\rho}\rangle$ and $\langle\tilde{\mu}\rangle$ variations in the boundary layer. Equations 7.11 and 7.12 are modified to include the integral wall scaling $y^{c+}$,

$$d\langle\tilde{u}\rangle^+ = \left(\frac{y^{c+}}{y^+}\frac{\langle\tilde{\mu}\rangle}{\mu_w}\sqrt{\frac{\rho_w}{\langle\bar{\rho}\rangle}}\right)\frac{1}{\kappa\ y^{c+}}dy^{c+} \tag{7.13}$$

$$d\langle\tilde{T}_i\rangle^+ = \left(\frac{y^{c+}}{y^+}\frac{\langle\tilde{\mu}\rangle}{\mu_w}\sqrt{\frac{\rho_w}{\langle\bar{\rho}\rangle}}\right)\frac{Pr_t}{\kappa\ y^{c+}}dy^{c+} \tag{7.14}$$

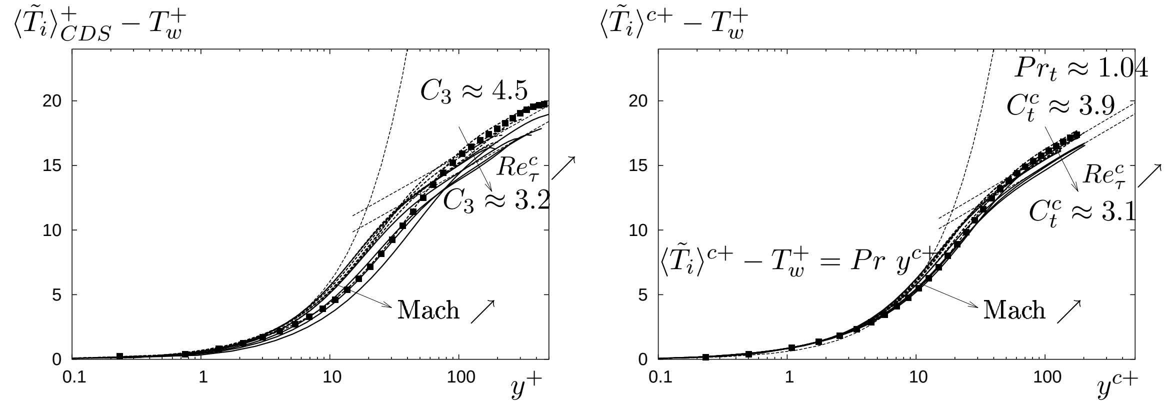

(a) VD transformation

(b) present integral transformation

Figure 7.5: **Mean total temperature profiles in a compressible channel at** $Re = 3000$ **and** $Re = 4880$**, for** $\mathcal{W}_{body}$ **( - - - ),** $\mathcal{W}_{ext}$ **( ■ ) and** $\mathcal{W}_{int}$ **( —— ).** $0.3 \leq M \leq 2$.

This leads to the following alternative integral transformation for both the velocity and total temperature, [7]

$$\langle\tilde{u}\rangle^{c+} = \int_0^{\langle\tilde{u}\rangle^+} \frac{y^+}{y^{c+}} \frac{\mu_w}{\langle\tilde{\mu}\rangle} \sqrt{\frac{\langle\bar{\rho}\rangle}{\rho_w}}\ d\langle\tilde{u}\rangle^+ = \frac{1}{\kappa}\ ln\ y^{c+} + C_u^c \tag{7.15}$$

$$\begin{aligned}\langle\tilde{T}_i\rangle^{c+} - T_w^+ &= = \int_{T_w^+}^{\langle\tilde{T}_i\rangle^+} \frac{y^+}{y^{c+}} \frac{\mu_w}{\langle\tilde{\mu}\rangle} \sqrt{\frac{\langle\bar{\rho}\rangle}{\rho_w}}\ d\langle\tilde{T}_i\rangle^+ = \frac{Pr_t}{\kappa}\ ln\ y^{c+} + C_t^c \qquad (7.16)\\ &= \left[\langle\tilde{T}\rangle^+ + \frac{\gamma-1}{2} Pr_m\ M_\tau^{c2}\ \langle\tilde{u}\rangle^{+2}\right]^c\end{aligned}$$

The present transformation is efficient since the buffer layer zone is much more compact than with the van Driest transformation (Figures 7.4b and 7.5b). The overprediction of the constant of the log-law up to $C_U^c \approx 8.0$ with respect to the expected incompressible value may be due to the specific wall boundary conditions in a channel. It is especially sensitive to the source term considered. Down to very low Mach numbers the wall heat flux $q_w$ is non-zero ($M_\tau^c \approx 0.3 - 0.4$ for $\mathcal{W}_{body}$ and $M_\tau^c \approx 0.1 - 0.2$ for $\mathcal{W}_{int}$) and the boundary conditions are not really adiabatic in contrast with the incompressible case which is defined with $M_\tau^c = \frac{M_\tau}{\sqrt{-B_q}} = \infty$. The constant of the log-law for the temperature $C_t^c \approx 3.0 - 4.0$ is close to the experimental values $C_3 \approx 3$ and $C_3 \approx 3.6$ obtained for compressible boundary layers by Debiève *et al.* [17] and Michel *et al.* [60], respectively. Finally, for either source term $\mathcal{W}_{body}$ and $\mathcal{W}_{int}$, a universal logarithmic law is obtained, based on the present integral transformation. The scatter in the value of $C_u^c$ and $C_t^c$ is reduced in comparison to the one obtained with the VD transformation.

For a spatially developing flow, the wall temperature $T_{wx}$ has to be considered, thus the VD transformation (Equation 7.12) and the present integral transformation (Equation 7.16) for the total temperature read

$$\langle\tilde{T}_i\rangle^+_{CDS} - T^+_{wx} = \int_{T_{wx}}^{\langle\tilde{T}_i\rangle^+} \frac{1}{Pr_t}\sqrt{\frac{\langle\bar{\rho}\rangle}{\rho_w}}\, d\langle\tilde{T}_i\rangle^+ = \frac{1}{\kappa}\, ln\ y^+ + C_3 \tag{7.17}$$

$$\begin{aligned}\langle\tilde{T}_i\rangle^{c+} - T^+_{wx} &= \int_{T_{wx}}^{\langle\tilde{T}_i\rangle^+} \frac{y^+}{y^{c+}}\frac{\mu_w}{\langle\tilde{\mu}\rangle}\sqrt{\frac{\langle\bar{\rho}\rangle}{\rho_w}}\, d\langle\tilde{T}_i\rangle^+ = \frac{Pr_t}{\kappa}\, ln\ y^{c+} + C^c_t \\ &= \left[\langle\tilde{T}\rangle^+ + \frac{\gamma-1}{2} Pr_m\ M^{c2}_\tau\ \langle\tilde{u}\rangle^{+2}\right]^c\end{aligned} \tag{7.18}$$

In Figures 7.6 and 7.7, the VD and the present integral transformations for velocity and total temperature are plotted for the spatially developing channel flow computed with $\mathcal{W}_{int}$ source term at the Reynolds number of $Re = 4880$ and the Mach number of $M = 0.7$. Very good agreements are obtained in the near-wall region between the integral laws and computed results for both, the velocity and the total temperature (Figures 7.6(b) and 7.7(b)). As shown in Section **??**, the quantity $\frac{\langle\tilde{T}\rangle - T_{wx}}{T_{wx}}$ and, consequently, $\langle\tilde{T}\rangle^+ - T^+_{wx}$ and $\langle\tilde{T}\rangle^{c+} - T^+_{wx}$ are homogeneous in the streamwise direction of the flow. For the present simulation, this result is not met since the non-dimensional heat flux $B_q$ is not constant in the streamwise direction (see Section 5.1).

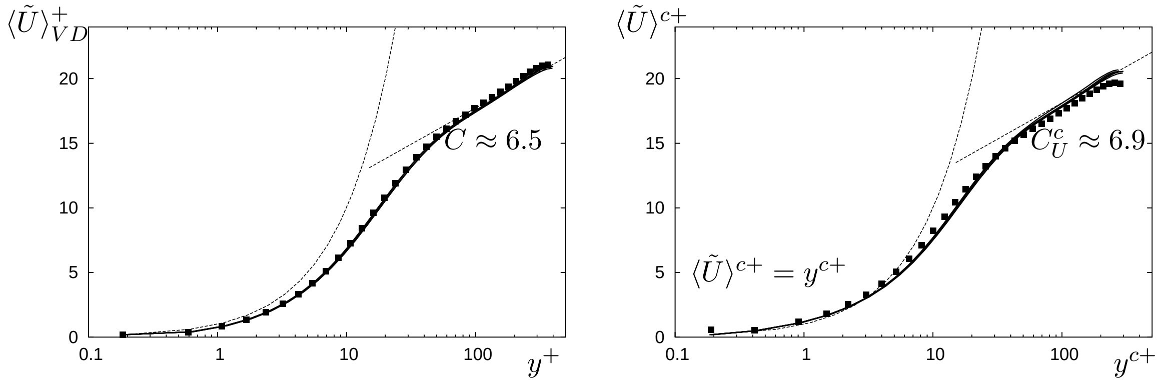

(a) VD transformation

(b) present integral transformation

Figure 7.6: **Mean velocity profiles in the spatially developing compressible channel at** $Re = 4880$, $M = 0.7$ **with** $\mathcal{W}_{int}$**: analytical laws ( - - - ), fully developed channel ( ■ ) and spatial computational boxes ( —— ).**

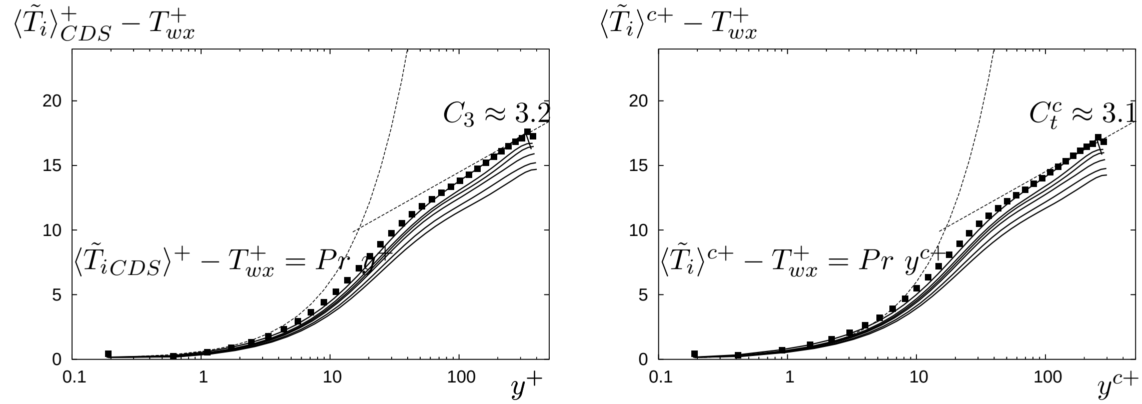

(a) VD transformation

(b) present integral transformation

Figure 7.7: **Mean total temperature profiles in the spatially developing compressible channel at $Re = 4880$, $M = 0.7$ with $\mathcal{W}_{int}$: analytical laws ( - - - ), fully developed channel ( ■ ) and spatial computational boxes ( —— ).**

## 7.3 RMS scaling

Huang *et al.* [34] propose a 'semi-local' renormalisation for the velocity fluctuations in order to account for density changes in the near wall region as well. The definition of the van Driest transformation valid for velocity increments (Equation 7.9) is used as an analogy for the RMS quantities:

$$analogy \left\{ \begin{array}{c} d\langle\tilde{u}\rangle^+_{VD} = \sqrt{\frac{\langle\bar{\rho}\rangle}{\rho_w}} d\langle\tilde{u}\rangle^+ \\ u^*_{rms} = \sqrt{\frac{\langle\bar{\rho}\rangle}{\rho_w}} u^+_{rms} \\ v^*_{rms} = \sqrt{\frac{\langle\bar{\rho}\rangle}{\rho_w}} v^+_{rms} \\ w^*_{rms} = \sqrt{\frac{\langle\bar{\rho}\rangle}{\rho_w}} w^+_{rms} \end{array} \right. \tag{7.19}$$

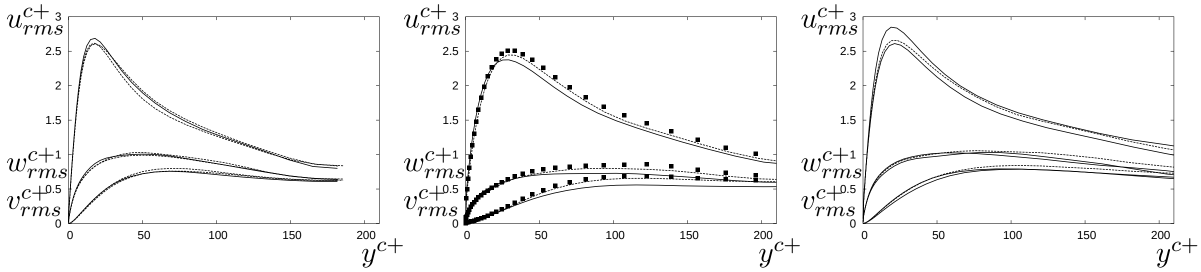

(a) $Re^c_\tau \approx 185$

(b) $Re^c_\tau \approx 240$

(c) $Re^c_\tau \approx 280$

Figure 7.8: **Streamwise, spanwise and wall-normal velocity fluctuations normalised with the present integral scaling, for $\mathcal{W}_{body}$ ( - - - ), $\mathcal{W}_{ext}$ ( ■ ) and $\mathcal{W}_{int}$ ( —— ). Table 6.1 : $Re^c_\tau \approx 185$ (a), $Re^c_\tau \approx 240$ (b) and $Re^c_\tau \approx 280$ (c).** $3000 \leq Re \leq 4880$, $0.3 \leq M \leq 2$.

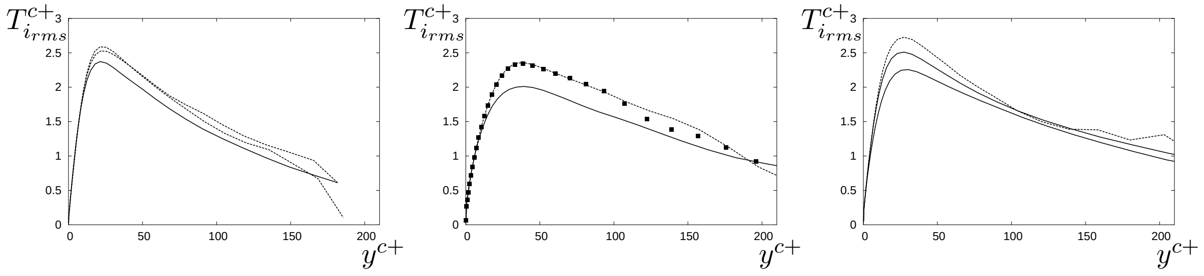

(a) $Re^c_\tau \approx 185$ (b) $Re^c_\tau \approx 240$ (c) $Re^c_\tau \approx 280$

Figure 7.9: **Total temperature fluctuations normalised with the present integral scaling, for $\mathcal{W}_{body}$ ( - - - ), $\mathcal{W}_{ext}$ ( ■ ) and $\mathcal{W}_{int}$ ( —— ). Table 6.1 : $Re^c_\tau \approx 185$ (a), $Re^c_\tau \approx 240$ (b) and $Re^c_\tau \approx 280$ (c). $3000 \leq Re \leq 4880$, $0.3 \leq M \leq 2$.**

We propose to consider a similar analogy to transpose Equations 7.13 and 7.14 for velocity and total temperature fluctuations, based on changes in both density and viscosity in the near wall region:

$$
analogy \begin{cases} d\langle\tilde{u}\rangle^{c+} = \frac{y^+}{y^{c+}} \frac{\mu_w}{\langle\tilde{\mu}\rangle} \sqrt{\frac{\langle\bar{\rho}\rangle}{\rho_w}} d\langle\tilde{u}\rangle^+ \\ u^{c+}_{rms} = \frac{y^+}{y^{c+}} \frac{\mu_w}{\langle\tilde{\mu}\rangle} \sqrt{\frac{\langle\bar{\rho}\rangle}{\rho_w}} u^+_{rms} \\ v^{c+}_{rms} = \frac{y^+}{y^{c+}} \frac{\mu_w}{\langle\tilde{\mu}\rangle} \sqrt{\frac{\langle\bar{\rho}\rangle}{\rho_w}} v^+_{rms} \\ w^{c+}_{rms} = \frac{y^+}{y^{c+}} \frac{\mu_w}{\langle\tilde{\mu}\rangle} \sqrt{\frac{\langle\bar{\rho}\rangle}{\rho_w}} w^+_{rms} \end{cases} \tag{7.20}
$$

$$
analogy \begin{cases} d\langle\tilde{T}_i\rangle^{c+} = \frac{y^+}{y^{c+}} \frac{\mu_w}{\langle\tilde{\mu}\rangle} \sqrt{\frac{\langle\bar{\rho}\rangle}{\rho_w}} d\langle\tilde{T}_i\rangle^+ \\ T^{c+}_{i_{rms}} = \frac{y^+}{y^{c+}} \frac{\mu_w}{\langle\tilde{\mu}\rangle} \sqrt{\frac{\langle\bar{\rho}\rangle}{\rho_w}} T^+_{i_{rms}} \end{cases} \tag{7.21}
$$

the total temperature RMS being computed from the definition $\tilde{T}_i = \tilde{T} + \frac{Pr_m}{2C_p}\ \tilde{u}_k^2$. We show that the weighting factor $\frac{y^+}{y^{c+}} \frac{\mu_w}{\langle\tilde{\mu}\rangle} \sqrt{\frac{\langle\bar{\rho}\rangle}{\rho_w}}$, introduced in the present new integral scaling yields a relatively constant RMS profile whatever source term is considered. One will note that two simulations with different source terms but the same integral Reynolds number $Re^c_\tau$ fit nearly perfectly for all three velocity components and the total temperature, once the fluctuations have been rescaled with Equations 7.20 and 7.21. The Coleman *et al.* [14] and Huang *et al.* [34] papers analyse the results of the combined van-Driest / semi-local scaling applied to two test cases (their two computed cases A and B) with the same semi-local Reynolds number $Re_{sl} = 150$ (Table 6.1 and their Figure 18b p. 175), which is a fully consistent procedure. A similar consistent comparison was also performed more recently by Morinishi *et al.* [61], (their Figure 6 p. 285). In the present work, we perform as well a consistent analysis of the LES results in the sense that the proposed integral scaling is applied to both the distance to the wall and the velocity or temperature amplitude. We finally compare rescaled results with the same integral Reynolds number $Re^c_\tau = 185$ on Figures 7.8a and 7.9a, $Re^c_\tau = 240$ on Figures 7.8b and 7.9b, and $Re^c_\tau = 280$ on Figures 7.8c and 7.9c. Our conclusions are finally the same as those of Coleman *et al.* and Morinishi *et al.* and show that for a given consistent scaling (whatever semi-local or integral) the behavior of the velocity and total temperaure RMS is relatively universal. These results confirm the universality of the turbulent scales in a compressible channel flow.

In Figures 7.10 and 7.11 the velocity and total temperature fluctuations normalized with the present integral scaling are plotted for the spatially developing channel flow computed with the $\mathcal{W}_{int}$ source formulation at the Reynolds number of $Re = 4880$ and the Mach number of $M = 0.7$. Good agreements between velocity fluctuations in spatially developing channel flow and fully developed channel flow, respectively, are found, whereas those concerning the total temperature do not fit, certainly due to the non-constant distribution of the non-dimensional heat flux $B_q$ in the spatially developing channel flow.

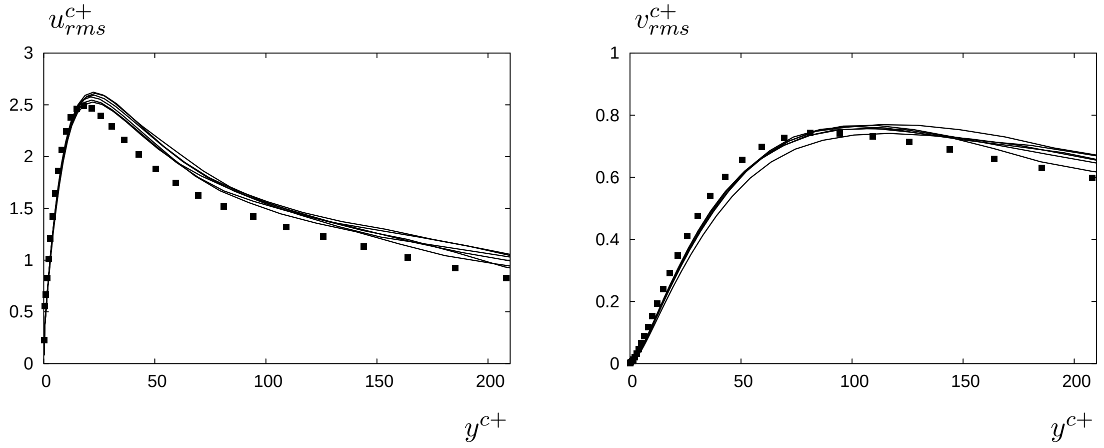

(a) Streamwise velocity fluctuations

(b) Wall-normal velocity fluctuations

Figure 7.10: **Streamwise (a) and wall-normal (b) velocity fluctuations normalised with the present integral scaling: fully developed channel ( ■ ) and spatial computational boxes ( —— ).**

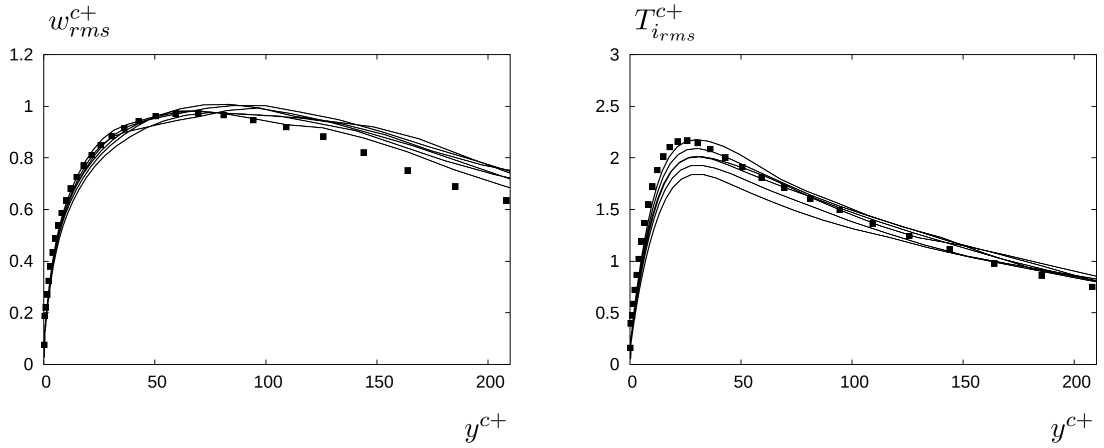

(a) Spanwise velocity fluctuations

(b) Total temperature fluctuations

Figure 7.11: **Spanwise velocity fluctuations (a) and total temperature fluctuations (b) normalised with the present integral scaling: fully developed channel ( ■ ) and spatial computational boxes ( —— ).**

## 7.4 Summary

We developed a so-called integral scaling for wall-bounded flows which is used to improve both the wall unit definition and the van Driest transformation in a consistent way. Both viscosity/conductivity and density effects are accounted for (in reference to Morkovin 1961) in the analytical developments we performed, and we showed that they play a key role in non-adiabatic boundary layers with strong wall temperature gradients, such as the wall layer in a fully developed or spatially developing compressible channel flow. The resulting integral Reynolds number provides a measure of the turbulent state of the compressible flow which is fully in the bound of the equivalent incompressible friction Reynolds number. We demonstrated, based on the present integral scaling, that for compressible turbulent channel flow, and irrespective of the source term considered, a relative universality of the wall layer property exists. One of the key ideas is to consider cases which have the same integral Reynolds number $Re_{\tau}^{c}$, as Huang *et al.* [34] did, with their semi-local scaling applied for two test cases with the same Reynolds number $Re_{sl}$. Our conclusions are, therefore, consistent with those of Morinishi *et al.* [61] and do not clearly differ from some of the recent work on pressure strain effect on the inner scaling for compressible channel flow by Foysi *et al.* [27], in which the semi-local compressible wall scaling was applied to cases with different $Re_{sl}$ numbers.

# CHAPTER 8

# Modelling of a distorted/separated wall layer

For flows with adverse streamwise pressure gradients, the traditional scaling is no longer applicable [85, 84, 90]. Thus, in the present chapter a new scaling is developed for the velocity and the total temperature based on wall friction, pressure gradient and wall heat flux. This scaling is applied to the velocity and temperature flow fields obtained from the distorted compressible channel flow (see Chapter 5.2). The chapter will end with a summary.

## 8.1 Wall scaling for compressible wall layers including $\frac{\partial p}{\partial x}$

For separated compressible wall layers, the streamwise pressure gradient $\frac{\partial \langle \bar{p} \rangle}{\partial x}$ cannot be neglected with respect to wall friction $\tau_w = \mu_w \frac{\partial \langle \tilde{u} \rangle}{\partial y}|_w$ and wall heat flux $q_w = -\lambda_w \frac{\partial \langle \tilde{T} \rangle}{\partial y}|_w$ (for non adiabatic wall conditions). [1] Therefore, velocity and total temperature are dependent on this set of parameters:

$$I_1 = I_1(\tau_w, \frac{\partial \langle \bar{p} \rangle}{\partial x}, \mu_w) \tag{8.1}$$

$$I_2 = I_2(\tau_w, q_w, \frac{\partial \langle \bar{p} \rangle}{\partial x}, \mu_w, \lambda_w, y) \tag{8.2}$$

Simpson [76] defined a streamwise pressure gradient based velocity $u_p$ in addition to the standard friction velocity $u_\tau$ as

$$u_p = \left| \frac{\mu_w}{\langle \tilde{\rho}_w \rangle^2} \frac{\partial \langle \bar{p} \rangle}{\partial x} \right|^{1/3} \tag{8.3}$$

These velocity scales, $u_\tau$ and $u_p$, will be referred to as inner scales, since the near-wall region is considered.

In order to describe which of the two effects, friction and pressure gradient, is preponderant, the ratio $\alpha \in [0, 1]$ is defined as [57, 66]

$$\alpha = \frac{u_\tau^2}{u_\tau^2 + u_p^2} = \frac{u_\tau^2}{u_{\tau p}^2} \tag{8.4}$$

---

[1] In this section only the viscous layer is examined, thus the turbulent viscosity $\langle \tilde{\mu}_t \rangle$ is neglected.

where $u_{\tau p}$ is a combined friction/streamwise pressure gradient velocity (referred to as extended inner velocity scale or extended inner scaling, alternatively),

$$u_{\tau p} = \sqrt{u_\tau^2 + u_p^2} \tag{8.5}$$

Note that, for a separated flow, the zero values of the $\alpha$ ratio correspond to the separation and reattachment points and its negative values mark the recirculation bubble.

We extend the non-dimensional procedure described above for the temperature and define a streamwise pressure gradient based temperature $T_p$ and a combined friction/streamwise pressure gradient temperature $T_{\tau p}$, respectively:

$$T_p = \frac{u_p^2}{2C_p} \tag{8.6}$$

$$T_{\tau p} = T_p + T_\tau \tag{8.7}$$

The ratio $\beta \in [0,1]$ defined by

$$\beta = \frac{T_\tau}{T_\tau + T_p} \tag{8.8}$$

quantifies the relative importance of each of the two involved inner temperature scales, $T_\tau$ and $T_p$.

Based on the extended inner scale for the velocity, $u_{\tau p}$, and for the temperature, $T_{\tau p}$, the non-dimensional velocity, $\langle\tilde{u}\rangle^*$, the non-dimensional total temperature $\langle\tilde{T_i}\rangle^*$ and the non-dimensional length $y^*$ are defined as

$$\langle\tilde{u}\rangle^* = \frac{\langle\tilde{u}\rangle}{u_{\tau p}} \tag{8.9}$$

$$\langle\tilde{T_i}\rangle^* = \frac{\langle\tilde{T_i}\rangle}{T_{\tau p}} \tag{8.10}$$

$$y^* = \frac{\rho_w y u_{\tau p}}{\mu_w} \tag{8.11}$$

The ratio between classical $(\langle\tilde{u}\rangle^+; \langle\tilde{T_i}\rangle^+; y^+)$ and extended $(\langle\tilde{u}\rangle^*; \langle\tilde{T_i}\rangle^*; y^*)$ inner coordinates can be expressed in terms of $\alpha$ and $\beta$ as

$$\frac{\langle\tilde{u}\rangle^*}{\langle\tilde{u}\rangle^+} = \sqrt{\alpha} \tag{8.12}$$

$$\frac{\langle\tilde{T_i}\rangle^*}{\langle\tilde{T_i}\rangle^+} = \beta \tag{8.13}$$

$$\frac{y^*}{y^+} = \frac{1}{\sqrt{\alpha}} \tag{8.14}$$

Extended laws of the wall for the velocity and the total temperature might be now derived from Equations 6.1 and 6.2 as functions of only non-dimensional parameters $(y^*, \alpha, \beta)$,

$$\langle\tilde{u}\rangle^* = f(y^*, \alpha) \tag{8.15}$$

$$\langle\tilde{T_i}\rangle^* = f(y^*, \alpha, \beta) \tag{8.16}$$

After integration from the wall, Equations 6.1 and 6.2 write:

$$\begin{aligned}
\frac{\langle\tilde{\mu}(T)\rangle}{\mu_w}\frac{\partial\langle\tilde{u}\rangle^*}{\partial y^*} &= sign\left(\frac{\partial\langle\bar{p}\rangle}{\partial x}\right)(1-\alpha)^{3/2}y^* + sign(\tau_w)\alpha && (8.17)\\
\frac{\langle\tilde{\mu}(T)\rangle}{\mu_w}\frac{\partial\langle\tilde{T_i}\rangle^*}{\partial y^*} &= \frac{2\gamma}{\gamma-1}sign\left(\frac{\partial\langle\bar{p}\rangle}{\partial x}\right)(1-\beta)\sqrt{1-\alpha}Pr\int_0^{y^*}\langle\tilde{u}\rangle^* dy^* && (8.18)\\
&+ sign(-q_w)\beta\sqrt{\alpha}Pr
\end{aligned}$$

Integration of Equation 8.17 from the wall leads to a parabolic velocity profile [85, 84, 90]:

$$\langle\tilde{u}\rangle^*(y^*) = sign(\tau_w)\alpha y^{c*} + sign\left(\frac{\partial\langle\bar{p}\rangle}{\partial x}\right)\frac{(1-\alpha)^{3/2}}{2}y_2^{c*2} \tag{8.19}$$

where

$$y^{c*} = \int_0^{y^*}\frac{\mu_w}{\langle\tilde{\mu}(T)\rangle}dy^* = \frac{\mu_w}{\mu_1}y^* \tag{8.20}$$

$$y_2^{c*^2} = \int_0^{y^{*2}}\frac{\mu_w}{\langle\tilde{\mu}(T)\rangle}dy^{*^2} = \frac{\mu_w}{\mu_2}y^{*^2} \tag{8.21}$$

are based on the integral lengthscale definition of Equation (7.1).

Finally, integration of Equation (8.18) from the wall leads to a polynomial total temperature profile:

$$\begin{aligned}
\langle\tilde{T_i}\rangle^*(y^*) &= T_{wx}^* + sign(-q_w)\beta\sqrt{\alpha}Pr y^{c*} && (8.22)\\
&+ \frac{\gamma}{\gamma-1}sign\left(\frac{\partial\langle\bar{p}\rangle}{\partial x}\right)(1-\beta)Pr\left[\frac{\alpha\sqrt{1-\alpha}}{3}\frac{\mu_w}{\mu_1}y_3^{c*^3} + \frac{(1-\alpha)^2}{12}\frac{\mu_w}{\mu_2}y_4^{c*^4}\right]
\end{aligned}$$

with

$$y_3^{c*^3} = \int_0^{y^{*3}}\frac{\mu_w}{\langle\tilde{\mu}(T)\rangle}dy^{*^3} = \frac{\mu_w}{\mu_3}y^{*^3} \tag{8.23}$$

$$y_4^{c*^4} = \int_0^{y^{*4}}\frac{\mu_w}{\langle\tilde{\mu}(T)\rangle}dy^{*^4} = \frac{\mu_w}{\mu_4}y^{*^4} \tag{8.24}$$

For flows with zero pressure gradient ($\alpha = \beta = 1.0$), we obtain the classical law of the wall for compressible boundary layer (Equations 7.1 and 7.2) with $\langle\tilde{u}\rangle^* = \langle\tilde{u}\rangle^+$, $\langle\tilde{T_i}\rangle^* = \langle\tilde{T_i}\rangle^+$ and $y^{c*} = y^{c+}$. For flows with zero wall friction ($\alpha = 0.0$) and zero wall heat flux ($\beta = 0.0$), we obtain a quadratic law accounting for the pressure gradient effect only:

$$\begin{aligned}
\langle\tilde{u}\rangle^*(y) &= \frac{1}{2}y_2^{c*2} && (8.25)\\
\langle\tilde{T_i}\rangle^*(y) &= T_{wx}^* + \frac{1}{12}\frac{\gamma}{\gamma-1}\frac{\mu_w}{\mu_2}Pr\ y_4^{c*4} && (8.26)
\end{aligned}$$

We present the results for the distorted channel flow computed with $\mathcal{W}_{int}$ source term at the Mach number of $M = 0.7$ and the Reynolds number of $Re = 4880$ (chapter 5.2). As expected, the lowest value of $\alpha$ ratio is obtained at about $\frac{x}{4\pi h} = 2.55$ (Figure 8.2(a)). The temperature field is less perturbed than the velocity field, thus the values of the $\beta$ ratio remain about $\beta = 1$ in full channel (Figure 8.2(b)).

All the inner scales are plotted in Figure 8.1. The effect of the streamwise adverse pressure gradient is obvious on the classical inner scales. Due to the weak perturbation, the streamwise pressure gradient based inner scales, $u_p$ and $T_p$, respectively, are smaller than the classical ones, $u_\tau$ and $T_\tau$, especially for the temperature.

Although the streamwise pressure gradient effect is weak for this simulation, the extended velocity law for the wall fits better the computed profiles (Figure 8.3).

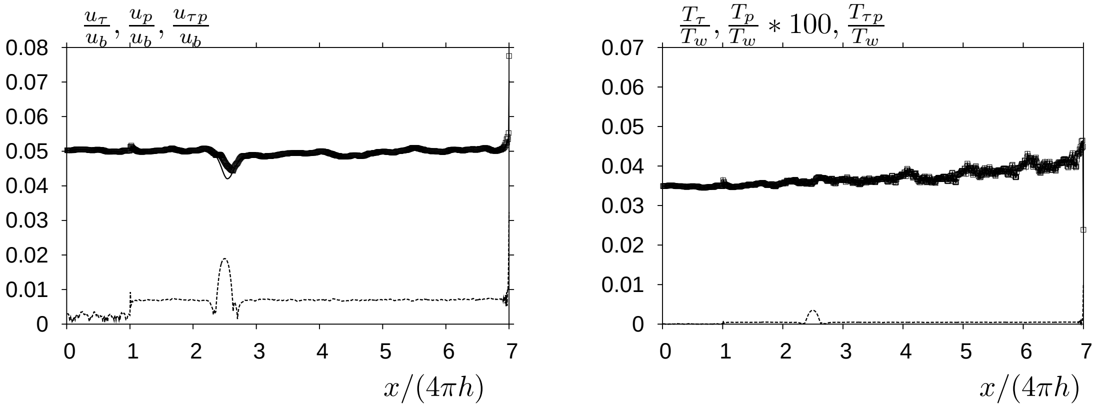

(a) inner velocity scales

(b) inner temperature scales

Figure 8.1: **Inner velocity scales (a) and inner temperature scales (b):** $u_\tau, T_\tau$ ( —— ), $u_p, T_p * 100$ **( - - - ) and** $u_{\tau p}, T_{\tau p}$ **( ■ ).**

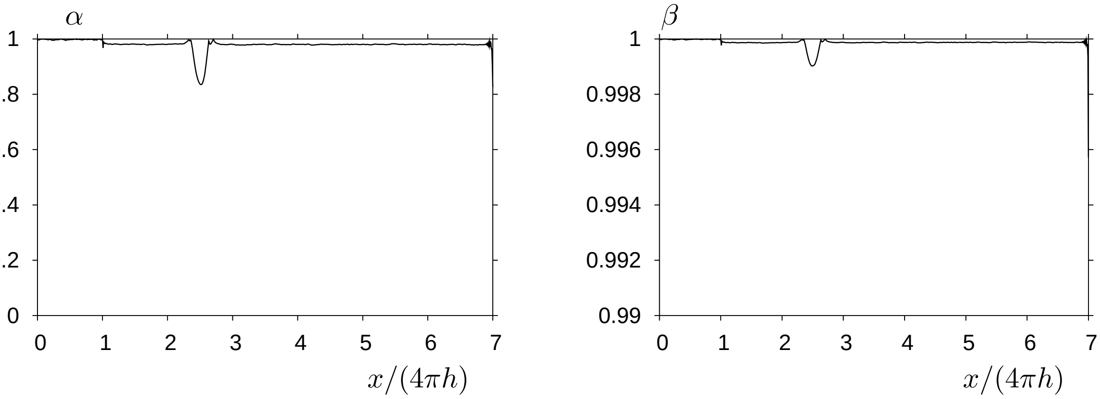

(a) $\alpha$ ratio

(b) $\beta$ ratio

Figure 8.2: $\alpha$ **and** $\beta$ **ratios in the distorted compressible channel at** $M = 0.7$ **and** $Re = 4880$, $\mathcal{W}_{int}$**.**

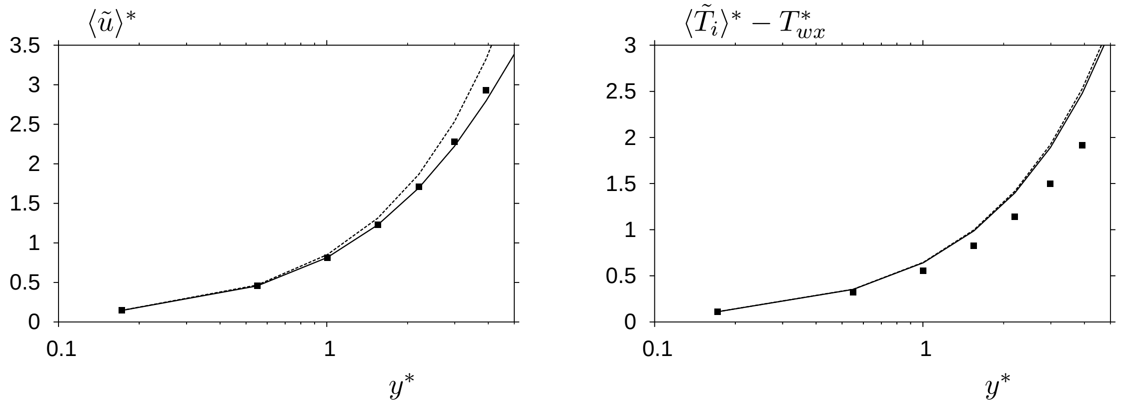

(a) velocity law

(b) temperature law

Figure 8.3: **Mean velocity (a) and mean total temperature (b) profiles in the distorted compressible channel: classical law ( - - - ), extended law ( —— ) and computational results ( ■ ).**

## 8.2 RMS scaling

Based on the $\alpha$ and $\beta$ parameters previously defined, the velocity and the temperature fluctuations might be written, respectively,

$$u^*_{rms} = \frac{u_{rms}}{u_{\tau p}} = u^+_{rms}\,\sqrt{\alpha} \tag{8.27}$$

$$v^*_{rms} = \frac{v_{rms}}{u_{\tau p}} = v^+_{rms}\,\sqrt{\alpha} \tag{8.28}$$

$$w^*_{rms} = \frac{w_{rms}}{u_{\tau p}} = w^+_{rms}\,\sqrt{\alpha} \tag{8.29}$$

$$T^*_{rms} = \frac{T_{rms}}{T_{\tau p}} = T^+_{rms}\,\beta \tag{8.30}$$

All these fluctuations are plotted in Figures 8.4 and 8.5 for different locations: upstream of the maximum distortion $\frac{x}{4\pi h} = 2.1875$ ( —— ), at the maximum distortion $\frac{x}{4\pi h} = 2.55$ ( ■ ) and downstream of the maximum distortion $\frac{x}{4\pi h} = 2.89$ ( □ ). The trend obtained with the $\alpha$, $\beta$ scaling seems to deserve better the universality than the classical scaling.

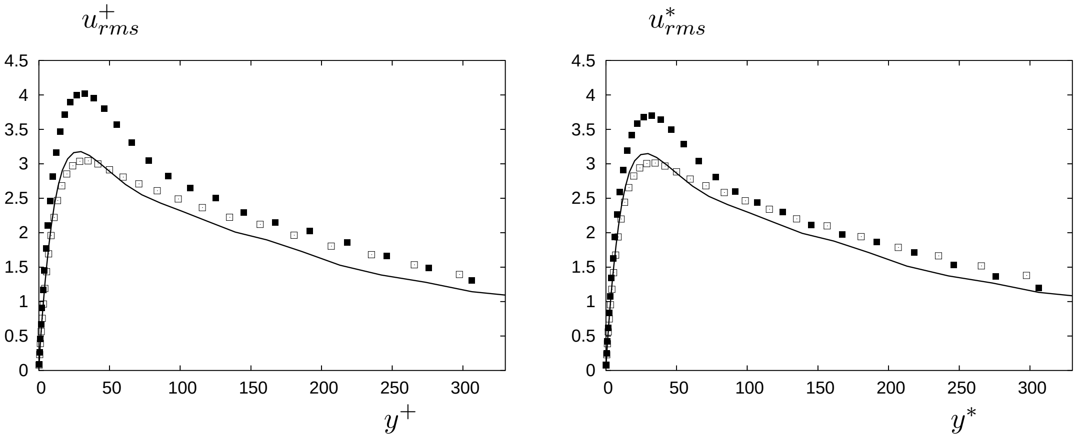

(a) Streamwise velocity fluctuations

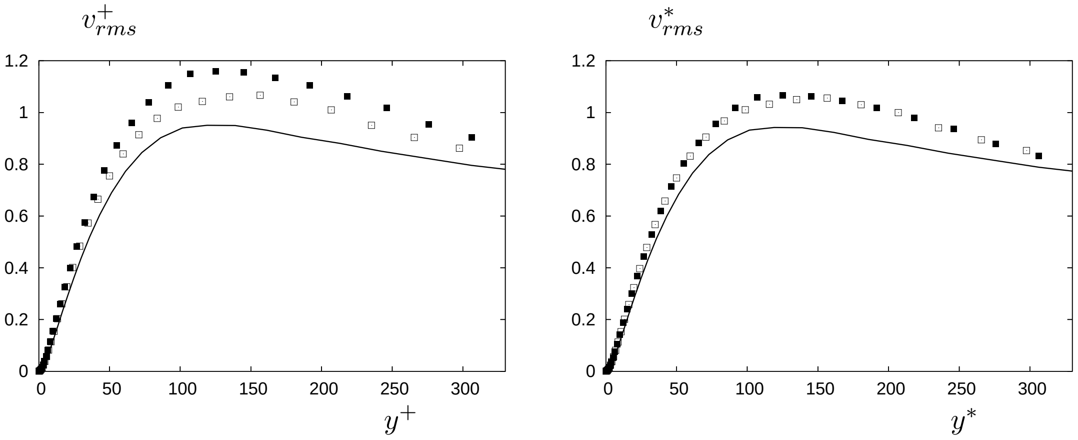

(b) Wall-normal velocity fluctuations

Figure 8.4: **Streamwise (a) and wall-normal (b) velocity fluctuations normalized with the classical scaling (left) and the present inner scaling (right): upstream of the maximum distortion** $\frac{x}{4\pi h} = 2.1875$ **( —— ), at the maximum distortion** $\frac{x}{4\pi h} = 2.55$ **( ■ ) and downstream of the maximum distortion** $\frac{x}{4\pi h} = 2.89$ **( □ ).**

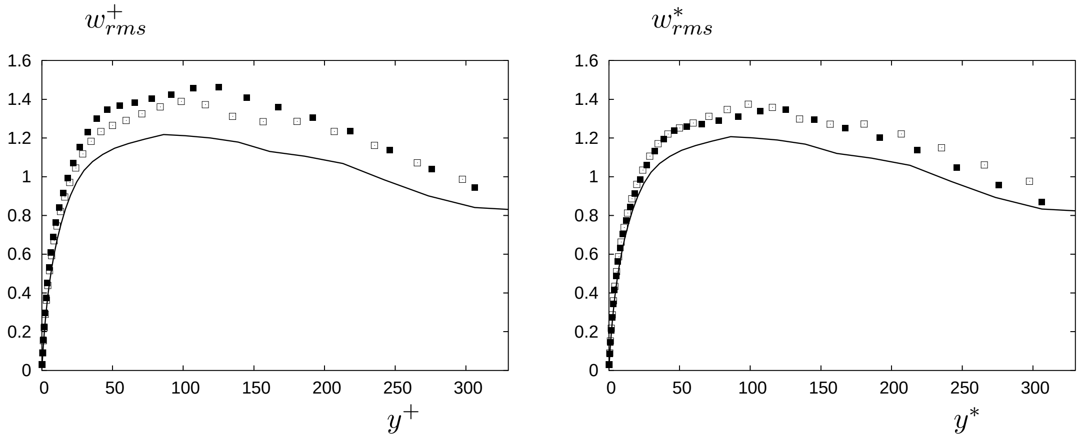

(a) Spanwise velocity fluctuations

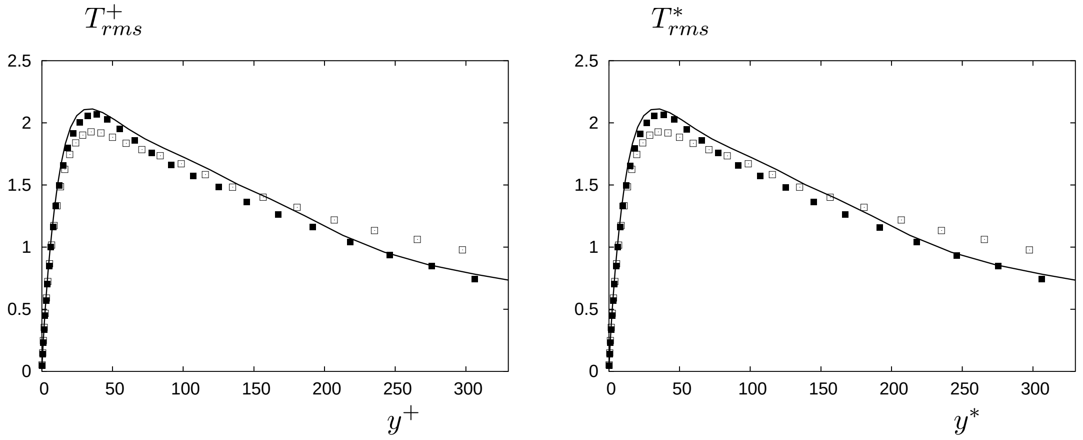

(b) Temperature fluctuations

Figure 8.5: **Spanwise velocity (a) and temperature (b) fluctuations normalized with the classical scaling (left) and the present inner scaling (right): upstream of the maximum distortion $\frac{x}{4\pi h} = 2.1875$ ( —— ), at the maximum distortion $\frac{x}{4\pi h} = 2.55$ ( ■ ) and downstream of the maximum distortion $\frac{x}{4\pi h} = 2.89$ ( □ ).**

## 8.3 Summary

Extended laws of the wall for the viscous sublayer have been developed. They account for the contributions of the pressure gradient in compressible turbulent flows. Two parameters, $\alpha$ and $\beta$, have been defined in order to quantify which effect, wall friction / wall heat flux and streamwise pressure gradient, is preponderant. Based on these parameters, analytical velocity and total temperature profiles have been derived from simplified boundary layer equations. An integral length scale $y^{c*}$ has been defined which accounts for viscosity and density changes in the boundary layer. A priori investigations of the scaling show good agreements in the distorted compressible turbulent channel flow when using wall model formulations including streamwise pressure gradient effects. The next step will be to develop an equivalent model in the turbulent region, accounting for turbulent stresses and turbulent heat fluxes.

# CHAPTER 9

# Discussion and Conclusions

LES of isothermal-wall compressible turbulent channel flows were performed in this PhD thesis. We revisited the description of the forcing term for compressible channel flow so that the streamwise periodic simulation resembles as much as possible the spatially evolving channel flow within its fully developed turbulent state. This requires, in addition to an artificial force term in the momentum equation, an artificial heat source term in the internal energy equation. It slightly increases the interest of using compressible channel flows as a realistic tool for wall modeling, in the sense that it accounts for the streamwise temperature loss induced by pressure drop in a spatially developing compressible channel flow. An important result is the homogeneity of the $\frac{\langle\tilde{T}\rangle - T_{wx}}{T_{wx}}$ quantity, which validates the hypothesis made to derive the $\mathcal{W}_{int}$ source term used to model the pressure drop in a fully developed channel flow. Comparisons with the classical source formulation derived in the incompressible context show a main difference in terms of heating effect, yielding a maximum temperature in the center of the channel about 4.5 times larger. Nevertheless, the channel flow configuration appears as a typical wall-bounded flow family that can be further investigated in order to *'simulate non-physical flows to gain insights into real flows'* [42].

A main effort was done to implement both, inlet and outlet boundary conditions based on the characteristic analysis [86, 87, 68]. A fully developed channel flow is considered in order to ensure realistic inflow conditions for the spatial channel. Non-reflecting outflow conditions are applied at the outlet of the spatial channel. Accurate results have been obtained, although the outlet boundary condition is not perfect and an additional hypothesis concerning the diffusive terms in the total energy equation might be used.

We extended a body forcing method, used by Howard [32] to obtain a turbulent incompressible bubble, to a compressible turbulent flow. This consists in using a distributed force to model an adverse streamwise pressure gradient. Only a distorted region has been generated due the low amplitude of the distributed force artificially implemented in our compressible Navier-Stokes solver. Although the obtained channel flow is only weakly distorted, we found that the streamwise pressure gradient influences the mean velocity and mean temperature profiles, especially in the near-wall region, and modifies the distributions of wall friction and wall heat flux, respectively.

All these simulations, fully compressible developed channel flow, spatially developing compressible channel flow and distorted compressible channel flow, respectively, have been analysed in terms of statistics and coherent structures.

We proposed an analytical framework for the determination of the $c$ constant in the so-called modified strong Reynolds analogy (CESRA) by Huang *et al.* based on Crocco-Busemann type relations derived for compressible channel flow. We obtained $c = 1/Pr_m$ and showed that the used of the mixed Prandtl number yields a good fit of the results for fully developed channel flow, independent of the source term formulation used, and, also, for spatially developing and distorted channel flow.

The van Driest transformation for the velocity and Carvin *et al.* transformation for the temperature, which consider only the density correction, have been improved in a consistent way for the present isothermal-wall channel flows. We developed a so-called integral scaling which accounts for both viscosity/conductivity and density effects. The resulting integral Reynolds number provides a measure of the turbulent state of the compressible flow. Based on the present integral scaling, we demonstrated that for compressible turbulent channel flow, irrespective of the source term considered, a relative universality of the wall layer property exists.

We proposed an extended scaling for the near-wall region of distorted and separated compressible turbulent boundary layers. This scaling takes into account the influence of the wall shear stress, the wall heat flux and the adverse streamwise pressure gradient. Based on the present scaling, extended inner velocity, $u_{\tau p}$, temperature, $T_{\tau p}$, and length scales, $u^*$ and $u^{c*}$, have been defined. In the viscous region, analytical laws of the wall for the velocity and the total temperature have been derived. They are function only of three parameters: the wall distance $y^*$, and the dimensionless parameters $\alpha$ and $\beta$. The $\alpha$ parameter quantifies the relative importance of the streamwise pressure gradient with respect to the wall shear stress. The $\beta$ parameter quantifies which of the two effects, wall heat flux and streamwise pressure gradient, respectively is preponderant. These laws of the wall coincide with the classical ones for vanishing streamwise pressure gradients. The present scaling has been successfully applied to the distorted compressible channel flow.

As future work, we may summarize:

- an improvement of the outlet boundary condition. The starting point is the viscous condition concerning $\frac{\partial}{\partial x}\left(\mu \frac{\partial T}{\partial x}\right)$ presently considered to be zero.

- once the boundary conditions improved and validated for the subsonic case, supersonic compressible channel flows with and without pressure gradient distortion might be simulated.

- in order to obtain a separation bubble in the compressible turbulent channel flow, a longer domain might be needed to disturb in a similar manner. Also, an increase of the amplitude of the distributed force applied to model the streamwise adverse pressure gradient might be necessary. For an incompressible channel flow, Howard used a force amplitude of 40.

- to develop extended laws in the turbulent region of distorted/separated compressible channel flows for the velocity and total temperature, respectively. These laws have to account for adverse streamwise pressure gradients, turbulent stresses and turbulent heat fluxes.

- it could be interesting to apply these turbulent modelling issues to compressible boundary layers data as well. A possible success could confirm the universality of the turbulent scales in turbulent flows.

# Appendix

# APPENDIX A

# Spatially developing channel flow

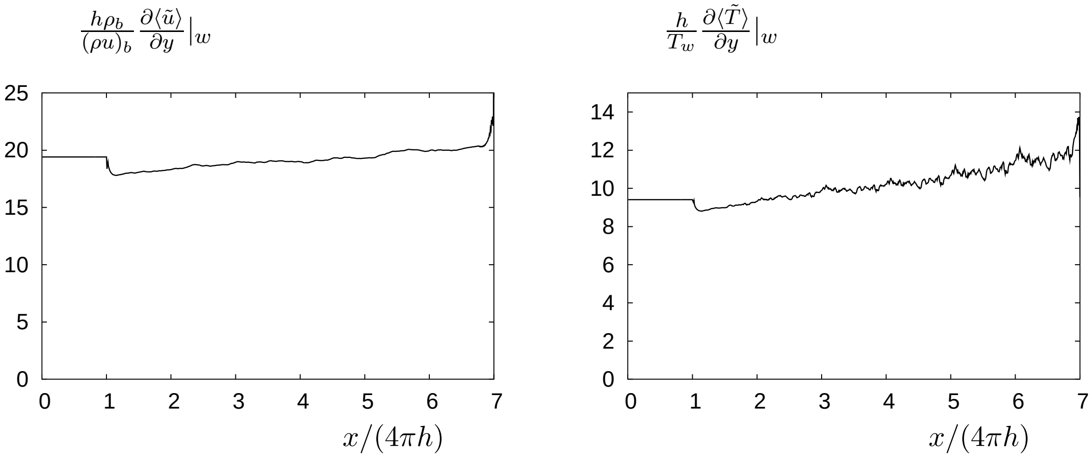

(a) Wall streamwise velocity gradient

(b) Wall temperature gradient

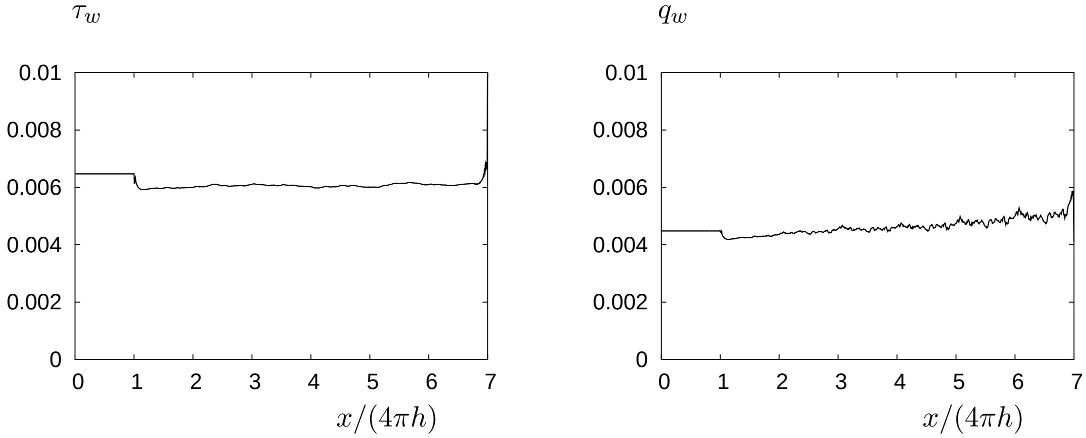

(c) Wall friction

(d) Wall heat flux

Figure A.1: **Distributions of the wall streamwise velocity gradient (a), the wall temperature gradient (b), the wall friction (c) and the wall heat flux (d) in the spatially developing channel flow at $Re = 4880$ and $M = 0.7$.**

[1]

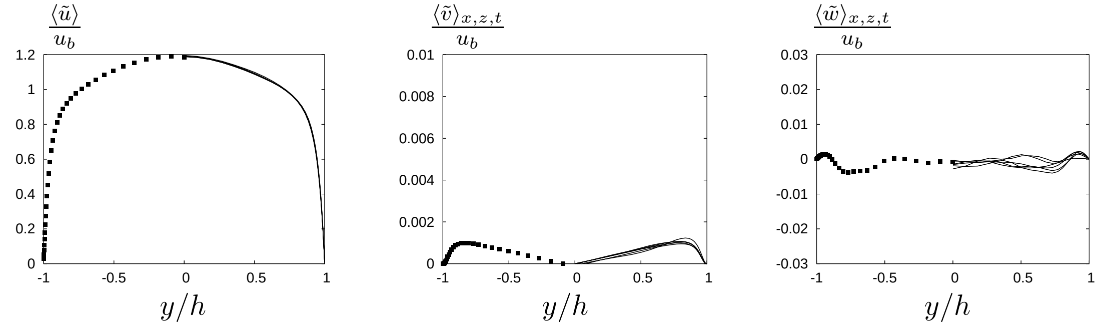

(a) Streamwise velocity

(b) Wall-normal velocity

(c) Spanwise velocity

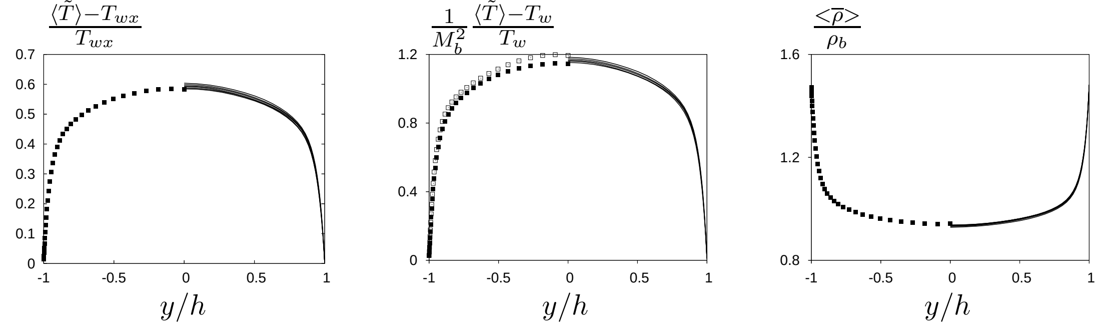

(d) Temperature

(e) Crocco-Bussemann temperature profile

(f) Density

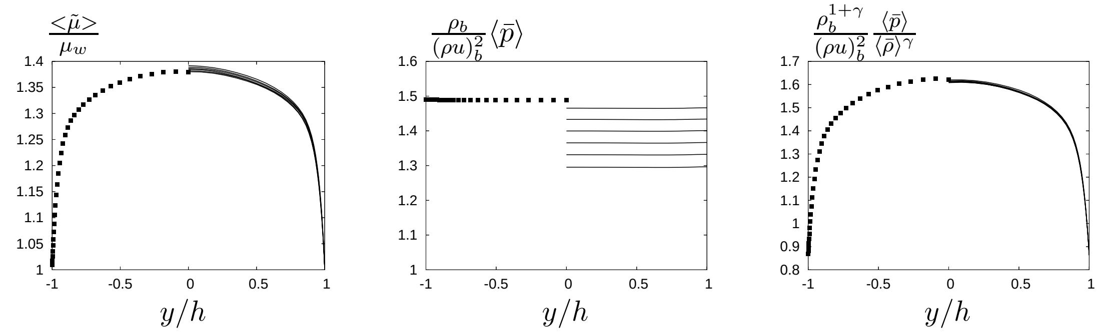

(g) Dynamic viscosity

(h) Pressure

(i) Entropy

Figure A.2: **Comparison between numerical results in fully developed channel ( ■ ) and spatial computational boxes ( —— ): profiles of (a) mean streamwise velocity, (b) mean wall-normal velocity, (c) spanwise velocity, (d) mean temperature, (e) Crocco-Busemann type relation (4.7), (f) mean density, (g) mean dynamic viscosity, (h) mean pressure and (i) entropy.**

---

[1] Transverse profiles are plotted at six consecutive locations in the spatial channel ($x/(4\pi h) = 1.5$, 2.5, 3.5, 4.5, 5.5 and 6.5, see Figure 5.1. In order to plot the entropy profile, the pressure in the spatial computational boxes was corrected in terms of the pressure gradient loss ($f = \frac{\partial\langle\bar{p}\rangle}{\partial x}$).

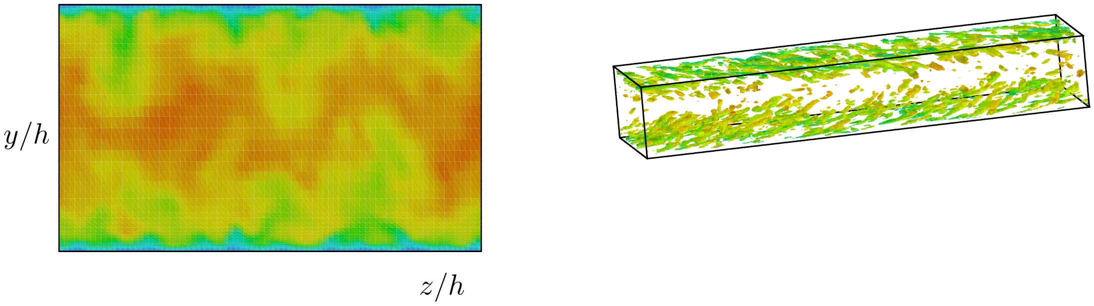

(a) third spatial computational box

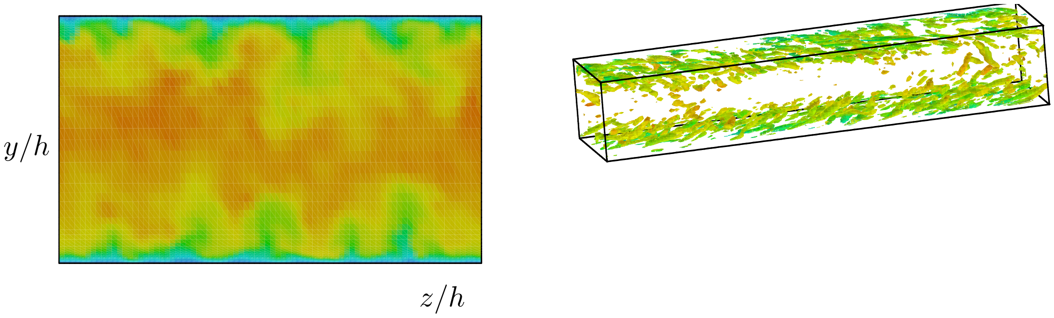

(b) fourth spatial computational box

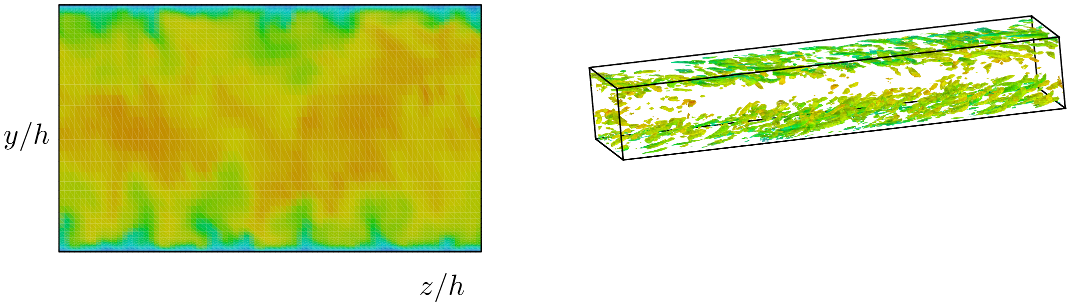

(c) fifth spatial computational box

Figure A.3: **Contour plot of instantaneous streamwise velocity in the $yz$ plane (left) and positive Q-criterion isovalues: $Q = \frac{u_b^2}{h^2}$ (right) in the spatial channel.**

# APPENDIX B

## Distorted channel flow

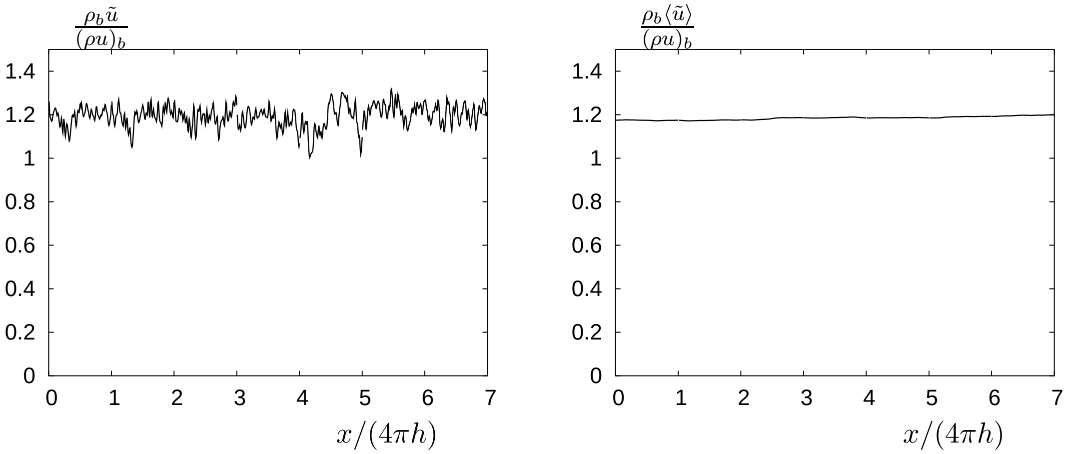

(a) at the centreline

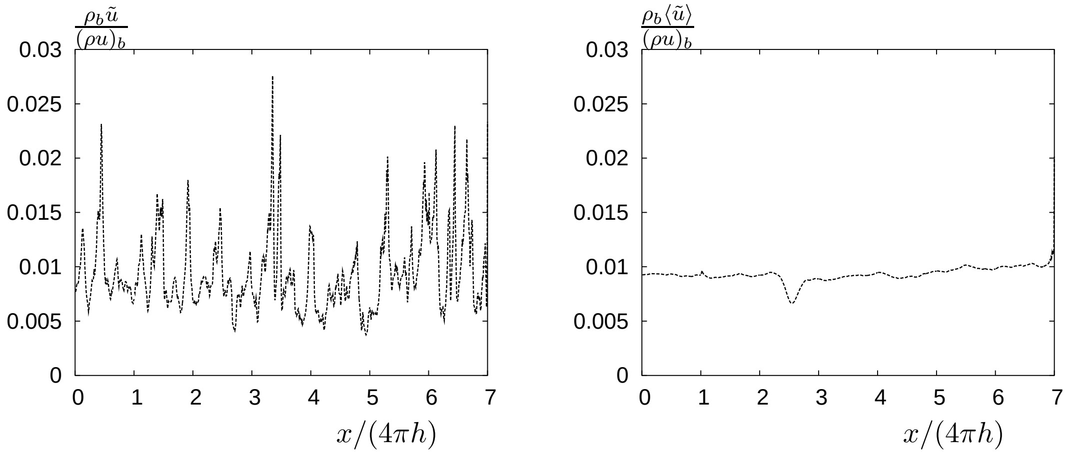

(b) at the first grid point

Figure B.1: **Instantaneous and mean streamwise velocity profiles in the $x$-direction at the centreline (a) and at the first grid point in the wall-normal direction (b).**

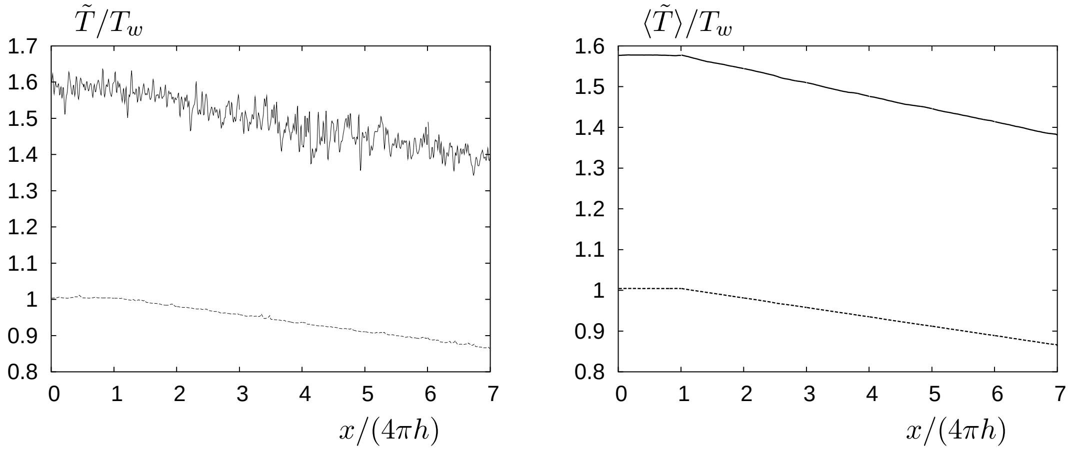

(a) Instantaneous and mean temperature

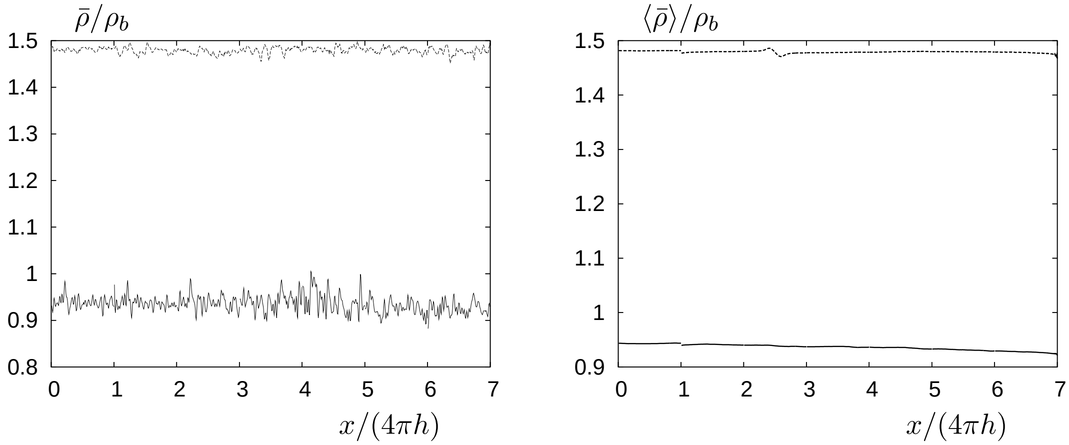

(b) Instantaneous and mean density

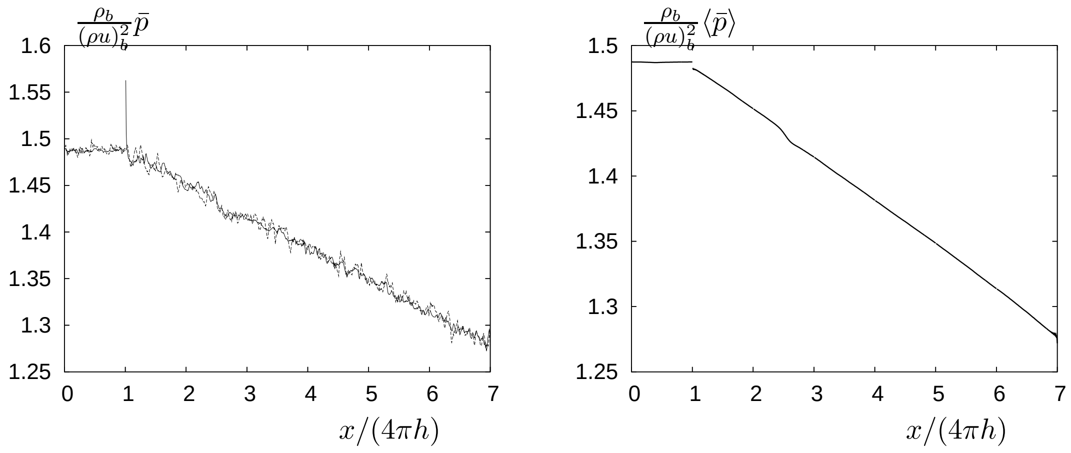

(c) Instantaneous and mean pressure

Figure B.2: **Instantaneous and mean streamwise profiles of temperature (a), density (b) and pressure (c) at the centreline ( —— ) and at the first grid point in the wall-normal direction ( - - - ).**

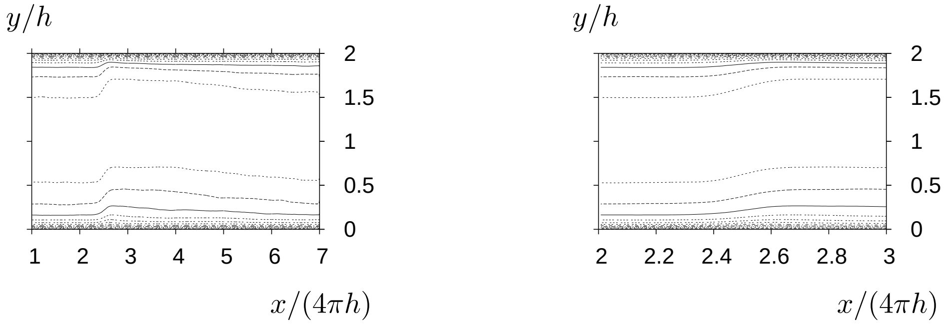

(a) Mean streamwise velocity

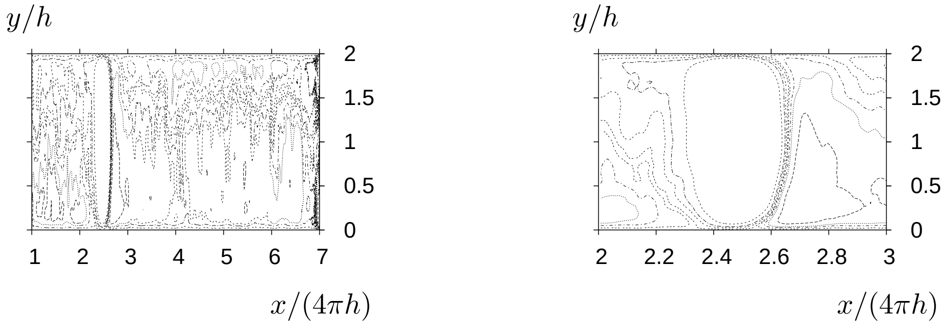

(b) Mean wall-normal velocity

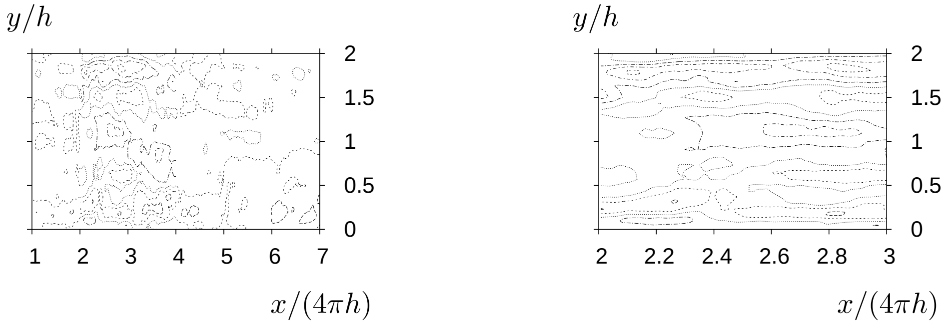

(c) Mean spanwise velocity

Figure B.3: **Isovalues of mean velocites in the streamwise direction (a), in the wall-normal direction (b) and in the spanwise direction (c): all the spatial computational boxes (left) and the second spatial computational box (right).**

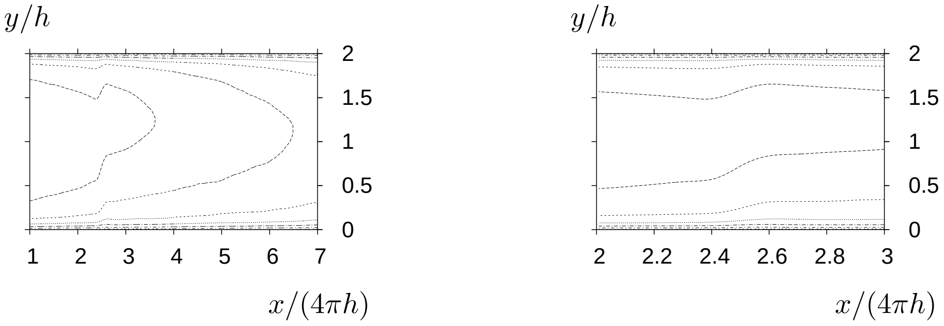

(a) Mean temperature

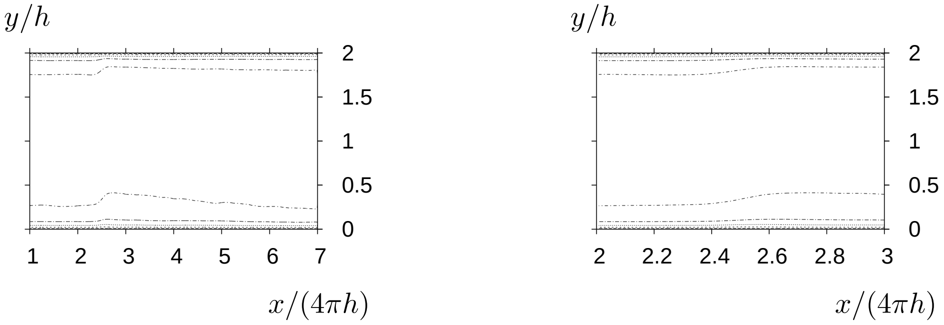

(b) Mean density

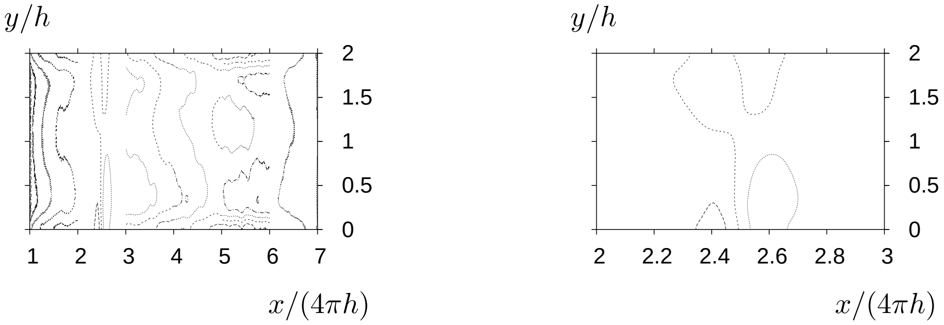

(c) Mean pressure corrected by the pressure drop

Figure B.4: **Isovalues of the mean temperature (a), the mean density (b) and mean pressure corrected by the pressure drop (c): all the spatial computational boxes (left) and the second spatial computational box (right).**

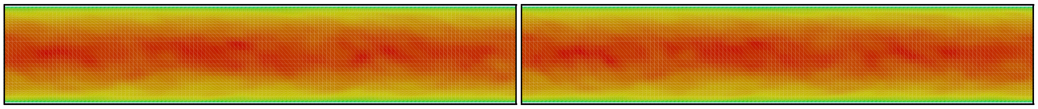

(a) inflow channel and first spatial computational box

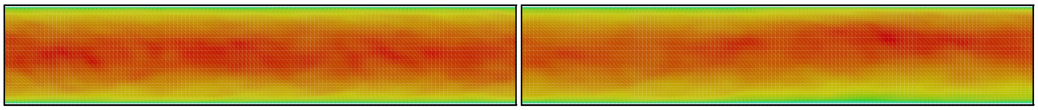

(b) first and second spatial computational boxes

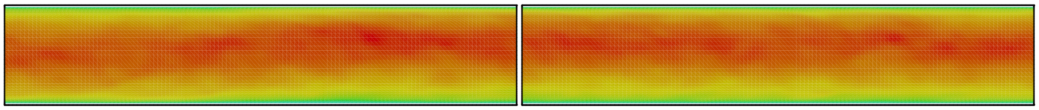

(c) second and third spatial computational boxes

Figure B.5: **Isovalues of the mean streamwise velocity**

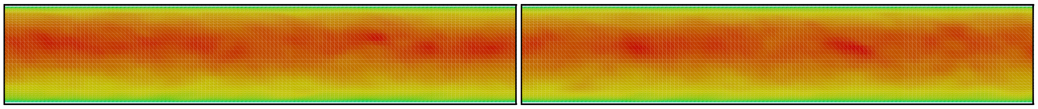

(a) third and fourth spatial computational boxes

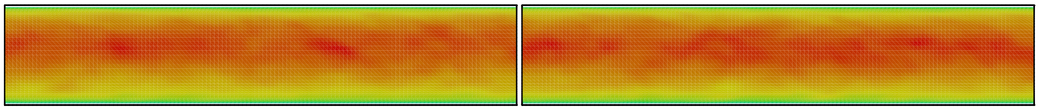

(b) fourth and fifth spatial computational boxes

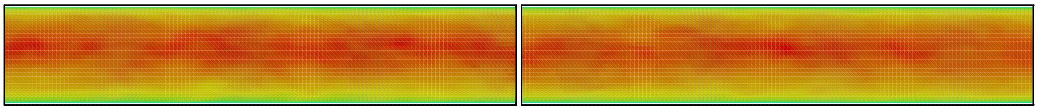

(c) fifth and sixth spatial computational boxes

Figure B.6: **Isovalues of the mean streamwise velocity**

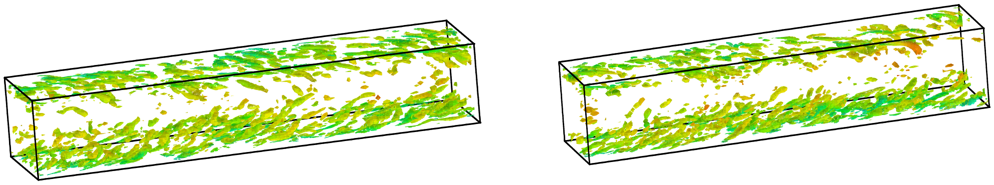

(a) first spatial computational box

(b) second spatial computational box

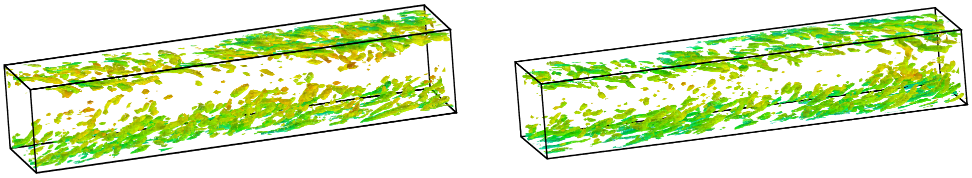

(c) third spatial computational box

(d) fourth spatial computational box

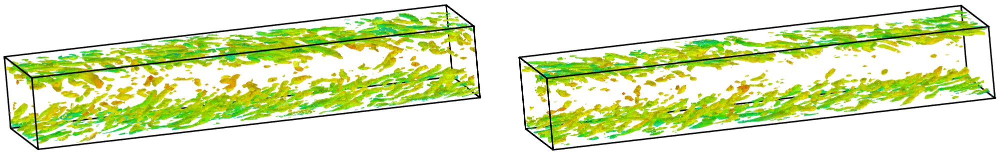

(e) fifth spatial computational box

(f) sixth spatial computational box

Figure B.7: **Positive Q-criterion isovalues:** $Q = \frac{u_b^2}{h^2}$ **in the distorted channel.** $Re = 4,880$ **and** $M = 0.7$**.**

# BIBLIOGRAPHY

[1] http://www.mpi-forum.org/docs/mpi1-report.pdf.

[2] A.E. Alving and H.H. Fernholz. Turbulence measurements around a mild separation bubble and downstream of reattachement. *J. Fluid Mech.*, 332:297–328, 1996.

[3] R.A. Antonia, J. Kim, and L.W.B. Browne. Some characteristics of small-scale turbulence in a turbulent duct flow. *J. Fluid Mech.*, 233:369–388, 1991.

[4] V. Baskaran, J. Smits, and P.N. Joubert. A turbulent flow over a curved hill part 1. growth of an internal boundary layer. *J. Fluid Mech.*, 182:47–83, 1987.

[5] V. Baskaran, J. Smits, and P.N. Joubert. A turbulent flow over a curved hill part 2. effects of streamline curvature and streamwise pressure gradient. *J. Fluid Mech.*, 232:377–402, 1991.

[6] P. Bradshaw. Compressible turbulent shear layers. *Annu. Rev. Fluid. Mech.*, 9:33–54, 1977.

[7] C. Brun, M. Haberkorn, and P. Comte. Compressibility effects in fully developed channel flow up to $mach = 5$. *5th Euromech Fluid Mechanics Conference, Toulouse*, 2003.

[8] C. Brun, M. Petrovan Boiarciuc, M. Haberkorn, and P. Comte. Large eddy simulation of compressible channel flow. arguments in favour of universality of compressible turbulent wall bounded flows. *Theor. Comput. Fluid Dyn.*, 2008. DOI 10.1007/s00162-007-0073-y.

[9] A. Busemann. In Leipzig Geest und Portig, editor, *Handbuch der physik*, volume 4, 1931.

[10] Strikwerda J. C. Initial boundary value problems for incompletely parabolic systems. *Commun. Pure Appl. Math.*, 30:797–822, 1977.

[11] C. Carvin, J.F. Debiève, and A.J. Smits. The near wall temperature profile of turbulent boundary layers. *AIAA Meeting*, 1988.

[12] T. Cebeci and J Smith. *Analysis of turbulent boundary layers.* Academic Press, New York, 1974.

[13] D.G. Clark and N.D. Sandham. Flow visualisation patterns in a direct navier-stokes simulation of turbulent flow. 1995. QMW-EP-1107.

[14] G. Coleman, J. Kim, and R. Moser. A numerical study of turbulent supersonic isothermal-wall channel flow. *J. Fluid Mech.*, 305:159–183, 1995.

[15] P. Comte and M. Lesieur. Large-eddy simulations of compressible turbulent flows. In *Advances in turbulence modelling*, pages 77–79. Von Karman Institute, 1998. lecture series 1998-05.

[16] L. Crocco. Sulla transmissione del calore da una lamina pilana a un fluido scorrente ad alta velocità. *L'Aerotecnica*, 12:181–197, 1932. Translated as NACA TM 690.

[17] J.F. Debiève, P. Dupont, D.R. Smith, and A.J. Smits. Supersonic turbulent boundary layer subjected to step changes in wall temperature. *AIAA J.*, 35(1):51–57, 1997.

[18] P. Dengel and H.H. Fernholz. An experimental investigation of an incompressible turbulent boundary layer in the vicinity of separation. *J. Fluid Mech.*, 212:615–636, 1990.

[19] M. Dianat and I.P. Castro. Turbulence in a separated boundary layer. *J. Fluid Mech.*, 226:91–123, 1991.

[20] Y. Dubief. Simulation des grandes échelles de la turbulence de la région de proche paroi et des écoulements décollés. In *PhD Thesis*, 2000. Institut National Polytechnique de Grenoble, Grenoble.

[21] F. Ducros. Simulations numériques directes et des grandes échelles de la turbulence de la région de proche paroi et des écoulements décollés. In *PhD Thesis*, 1995. Grenoble.

[22] F. Ducros, P. Comte, and M. Lesieur. Large-eddy simulation of transition to turbulence in a boundary layer developing spatially over a flat plate. *J. Fluid Mech.*, 326:1–36, 1996.

[23] J.-P. Dussauge and J. Gaviglio. The rapid expansion of a supersonic turbulent flow: role of bulk dilatation. *J. Fluid Mech.*, 174:81–112, 1987.

[24] G. Erlebacher, M.Y. Hussaini, C.G. Speziale, and T.A. Zang. Towards a large-eddy simulation of compressible turbulent flows. *J. Fluid Mech.*, 238:155–185, 1992.

[25] H.H. Fernholz and P.J. Finley. A critical complication of compressible turbulent boundary layer data. *AGARD-AG*, 223, 1977.

[26] H.H. Fernholz and P.J. Finley. A critical commentary on mean flow data for two-dimensional compressible turbulent boundary layers. *AGARD-AG*, 253, 1980.

[27] H. Foysi, S. Sarkar, and R. Friedrich. Compressibility effects and turbulence scalings in supersonic channel flow. *J. Fluid Mech.*, 509:207–216, 2004.

[28] J. Gaviglio. Reynolds analogies and experimental study of heat transfer in the supersonic boundary layer. *J Heat. Mass Transfer*, 30(5):911–926, 1987.

[29] D. Gottlieb and E. Turkel. Dissipative two-four methods for time-dependent problems. *Math. Comp.*, 30:703–723, 1976.

[30] S. E. Guarini, R. D. Moser, K. Shariff, and Wray A. Direct numerical simulation of a supersonic turbulent boundary layer at mach 2.5. *J. Fluid Mech.*, 414:1–33, 2000.

[31] M. Haberkorn. Simulation des grandes echelles en canal plan turbulent : effets de compressibilité et propagation acoustique. In *PhD Thesis*, 2004. Institut de Mécanique des Fluides et des Solides, Strasbourg.

[32] R. Howard. Direct numerical simulation and modelling of turbulent channel flows subjected to complex distortions. In *PhD Thesis*, 1999. University of London, London.

[33] P.G. Huang and G.N. Coleman. Van driest transformation and compressible wall-bounded flows. *AIAA J.*, 305:185–218, 1994.

[34] P.G. Huang, G.N. Coleman, and P. Bradshaw. Compressible turbulent channel flows: Dns results and modelling. *J. Fluid Mech.*, 305:185–218, 1995.

[35] J.C.R. Hunt, A.A. Wray, and P. Moin. Eddies, stream and convergence zones in turbulent flows. In *Report CTR-S88, Center for Turbulence Research*, 1988. NASA Ames/Stanford University.

[36] J. Jeong and F. Hussain. On the identification of a vortex. *J. Fluid Mech.*, 285:69–94, 1995.

[37] J. Jeong, F. Hussain, W. Schoppa, and J. Kim. Coherent structures near the wall in a turbulent channel flow. *J. Fluid Mech.*, 332:185–214, 1997.

[38] J. Jimenez and P. Moin. The minimal flow unit in near-wall turbulence. *J. Fluid Mech.*, 225:213–240, 1991.

[39] Robinson S. K. Coherent motions in the turbulent boundary layer. *Annu. Rev. Fluid Mech.*, 23:601–639, 1991.

[40] C. Kennedy and M. Carpenter. Comparison of several numerical methods for simulation of compressible shear layers. *NASA technical paper*, 3484, 1997.

[41] H.T. Kim, S.J. Kline, and W.C. Reynolds. The production of turbulence near a smooth wall in a turbulent boundary layer. *J. Fluid Mech.*, 50:133–160, 1971.

[42] J. Kim. Physics and control of wall turbulence. *Direct and Large-Eddy Simulation VI. Poitiers*, 2005.

[43] J. Kim, P. Moin, and R.D. Moser. Turbulence statistics in fully-developed channel flow at low reynolds number. *J. Fluid Mech.*, 177:133–166, 1987.

[44] A. L. Kistler. Fluctuation measurements in a supersonic turbulent boundary layer. *Phys. Fluids*, 2:290–296, 2004.

[45] S.J. Kline, W.C. Reynolds, F.A. Schraub, and Runstadler P.W. The structure of turbulent boundary layers. *J. Fluid Mech.*, 30:741–773, 1967.

[46] L. Kovasznay. Turbulence in supersonic flow. *J. Aeronautical Sciences*, 20(10):657–682, 1953.

[47] P-A. Krogstad and L.E. Torbergsen. Invariant analysis of turbulent pipe flow. *Flow, Turbulence and Combustion*, 64:161–181, 2000.

[48] R. Lechner, J. Sesterhenn, and R. Friedrich. Turbulent supersonic channel flow. *Journal of Turbulence*, 2:01–25, 2001.

[49] M.J. Lee and W.C. Reynolds. Numerical experiments on the structure of homogeneous turbulence. In *Thermoscience Division*, 1985. Stanford University.

[50] E. Lenormand and P. Sagaut. Subgrid-scale models for large-eddy simultions of compressible wall bounded flows. *AIAA J.*, 38:1340–1350, 2000.

[51] E. Lenormand, P. Sagaut, and L. Ta Phuoc. Large-eddy simulation of subsonic and supersonic channel flow at moderate reynolds number. *Int. J. Num. Meth. Fluids*, 32:369–406, 2000.

[52] M. Lesieur. *Turbulence in Fluids*. Kluwer Academic Publishers, 1997. $3^{rd}$ revised and enlarged edition.

[53] M. Lesieur and O. Métais. New trends in large-eddy simulations of turbulence. *Annu. Rev. Fluid. Mech.*, 28:45–82, 1996.

[54] M. Lesieur, O. Métais, and P. Comte. *Large-Eddy Simulations of Turbulence*. Cambridge University Press, 2005.

[55] J.L. Lumley. Computational modeling of turbulent flows. *Adv. Appl. Mech.*, 18:123–176, 1978.

[56] J.L. Lumley and G.R. Newman. Return to isotropy of homogeneous turbulence. *J. Fluid Mech.*, 82:161–178, 1977.

[57] M. Manhart, N. Peller, and C. Brun. Near-wall scaling for turbulent boundary layers with adverse pressure gradient. a priori tests on dns of channel flow with periodic hill constrictions and dns of separating boundary layer. *Theor. Comput. Fluid Dyn.*, 2007. DOI 10.1007/s00162-007-0055-0.

[58] O. Métais and M. Lesieur. Spectral large-eddy simulation of isotropic and stably stratified turbulence. *J. Fluid Mech.*, 239:157–194, 1992.

[59] R. Michel. Aerodynamique experimentale. *Rebuffet*, 1, 1962.

[60] R. Michel, C. Quemard, and R. Durand. *ONERA N.T.*, 1969.

[61] Y. Morinishi, S. Tamano, and K. Nakabayashi. Direct numerical simulation of compressible turbulent channel flow between adiabatic and isothermal walls. *J. Fluid Mech.*, 502:273–308, 2004.

[62] M.V. Morkovin. Effects of compressibility on turbulent flows. In A.J. (ed) Favre, editor, *Mécanique de la turbulence*, pages 367–380. CNRS, 1961.

[63] M.V. Morkovin and R. E. Phinney. Extended applications of hot wire anemometry to high-speed yurbulent boundary layers. In *AFOSR TN-58-469*. Baltimore: Johns Hopkins Univ., 1958.

[64] R.D. Moser, J. Kim, and M. Mansour. Direct numerical simulation of turbulent channel flow up to $re_\tau = 590$. *Phys. Fluids*, 11(4):943–945, 1999.

[65] Y. Na and P. Moin. Direct numerical simulation of a separated turbulent boundary layer. *J. Fluid Mech.*, 374:379–405, 1998.

[66] N. Peller, C. Brun, and M. Manhart. Wall layer investigations of channel flow with periodic hill constrictions. *DLES 6, Poitiers, September 12-14*, 2005.

[67] U. Piomelli and E. Balaras. Wall-layer models for large-eddy simulations. *Annu. Rev. Fluid Mech.*, 34:349–374, 2002.

[68] T.J. Poinsot and S. K. Lele. Boundary conditions for direct simulations of compressible viscous flows. *J. Comp. Phys.*, 103:16–42, 1992.

[69] W.C. Reynolds. Fundamentals of turbulence for turbulence modelling and simulation. In *Lecture Notes for Von Karman Institute*, 1987. version 3.1, April 12.

[70] R. S. Rogallo and P. Moin. Numerical simulation of turbulent flows. *Annu. Rev. Fluid Mech.*, 16:99–137, 1984.

[71] M. Rubesin. Extra compressibility terms for favre-averaged two-equation models of inhomogeneous turbulent flows. In *NASA CR-177556*, NASA Ames, 1990.

[72] D.H. Rudy and J.C. Strikwerda. A nonreflecting outflow boundary condition for subsonic navier-stokes calculations. *J. Comp. Phys.*, 55(70):36, 1980.

[73] D.H. Rudy and J.C. Strikwerda. Boundary conditions for subsonic compressible navier-stokes calculations. *Computers and Fluids*, 9:327–338, 1981.

[74] M. Salinas Vásquez and O. Métais. Large-eddy simulation of the turbulent flow through a heated square duct. *J. Fluid Mech.*, 453:201–238, 2002.

[75] H. Schlichting. *Bondary-Layer theory.* McGraw-Hill, 1968. $3^{rd}$ english edition.

[76] R.-L. Simpson. A model for the backflow mean velocity profile. *AIAA J.*, 21:142, 1983.

[77] R.-L. Simpson. Turbulent boundary layer separation. *Ann. Rev. Fluid Mech.*, 21:205–234, 1989.

[78] R.-L. Simpson. Aspects of turbulent boundary layer separation. *Prog. Aerospace. Sci., Elsevier Science Ltd*, 32:457–521, 1996.

[79] D. R. Smith and A. J. Smits. The simultaneous measurement of velocity and temperature fluctuations in the boundary layer of a supersonic flow. *Exp. Thermal Fluid Sci.*, 1993.

[80] A. Smits and J. Dussauge. *Turbulent shear layers in supersonic flows.* American Institute of Physics, 1996.

[81] P. Spalart and G.N. Coleman. Numerical study of a separation bubble with heat transfer. *Eur. J. Mechanics, B Fluids*, 16(2):169–189, 1997.

[82] P. R. Spalart. Direct simulation of a turbulent boundary layer up to $re_\theta = 1410$. *J. Fluid Mech.*, 187:61–98, 1988.

[83] E. F. Spina, Smits A. J., and Robinson S. K. The physics of supersonic turbulent boundary layers. *Annu. Rev. Fluid Mech.*, 26:287–319, 1994.

[84] B.S. Stratford. An experimental flow with zero skin friction throughout its region of pression rise. *J. Fluid Mech.*, 5:17–35, 1959.

[85] B.S. Stratford. The prediction of separation of the turbulent boundary layer. *J. Fluid Mech.*, 5:1–16, 1959.

[86] K. W. Thompson. Time dependent boundary conditions for hyperbolic systems. *J. Comp. Phys.*, 68:1–24, 1987.

[87] K. W. Thompson. Time-dependent boundary conditions for hyperbolic systems, ii. *J. Comp. Phys.*, 89:439–461, 1990.

[88] E. Van Driest. Turbulent boundary layer in compressible fluid. *J. Aeronaut. Sci.*, 18(3):145–160, 1951.

[89] D.R. Webster, DeGraaff D.B., and Eaton J.K. Turbulent characteristics of a boundary layer over a two-dimensional bump. *J. Fluid Mech.*, 320:53–70, 1996.

[90] F.M. White. *Viscous fluid flow*. Mc Graw-Hill, 1974.

[91] X. Wu and P. Moin. A direct numerical simulation study on the mean velocity characteristics in turbulent pipe flow. *J. Fluid Mech.*, 608:81–112, 2008.

[92] P.K. Yeung and G. Brasseur. The reponse of isotropic turbulence to isotropic and anisotropic forcing at the large scales. *Phys. Fluids*, 3:884–897, 1991.

[93] A. D. Young. The equations of motion and energy and the velocity profile of a turbulent boundary layer in a compressible fluid. *College of Aeronaut., Cranfield*, (Rep. No. 42), 1951.